Trinity College Dublin
Coláiste na Tríonóide, Baile Átha Cliath
The University of Dublin

Properties of massive stars before death

Author:
Andrew Allan

Supervisor:
Prof. José Groh

A report submitted for the degree of Masters in Astrophysics

Massive Stars and Supernovae Group
School of Physics

September 3, 2021

Plagiarism Declaration

I have read and I understand the plagiarism provisions in the General Regulations of the University Calendar for the current year, found at: http://www.tcd.ie/calendar.
I have also completed the Online Tutorial on avoiding plagiarism 'Ready, Steady, Write', located at http://tcd-ie.libguides.com/plagiarism/ready-steady-write.
Andrew Allan

Abstract

Despite their importance, there is a lot yet to be learned regarding massive stars, particularly those at late evolutionary stages. In the first of two studies presented here, we investigate a suspected very massive star in one of the most metal-poor dwarf galaxies, PHL 293B. Excitingly, we report the disappearance of signatures previously associated with a massive Luminous Blue Variable (LBV) from our two 2019 spectra, in particular, broad Balmer emission with prominent P-Cygni profiles. Using CMFGEN, we compute radiative transfer models to predict properties of the LBV. Our models show that during 2001–2011 the LBV had: a luminosity of $2.5 - 3.5 \times 10^6$ $L_\odot$, a mass-loss rate of $0.005 - 0.020$ $M_\odot$ yr^{-1}, a wind velocity of 1000 km s^{-1}, effective and stellar temperatures of $6 - 6.8$ kK and $9.5 - 15$ kK, respectively. These properties indicate an eruptive state. We consider two main hypotheses for the absence of the broad emission components from the spectra obtained since 2011. One possibility is that we are seeing the end of an LBV eruption of a surviving star, with a mild drop in luminosity, a shift to hotter effective temperatures, and dust obscuration. Alternatively, the LBV could have collapsed to a massive black hole without the production of a bright supernova.

The second study considers Type-Ibn supernovae (SNe). Their early-time spectra feature narrow emission lines of mostly He, signatures of interaction between SN ejecta and a dense, H-poor, He-rich circumstellar medium (CSM). Assuming this CSM was expelled by the progenitor prior to explosion, these signatures allow for predictions of progenitor properties such as mass-loss rate and surface composition. Hence, we fit CMFGEN models to early-time spectra of Type-Ibn SNe. It is our understanding that this will be the first detailed radiative transfer study for such spectra. Our best-fit models to a spectrum of SN 2010al obtained 5.7 days post explosion predict: a SN luminosity between 5.3-10 $\times 10^{10}$ $L_\odot$, a progenitor mass-loss rate between 0.34-0.52 $M_\odot$yr^{-1}, a wind velocity of 1000 km s^{-1}, an inner boundary radius to the CSM $R_{\rm in}$ of 1.2 $\times 10^{15}$ cm. These properties, combined with the H-free and N-rich nature of our models are consistent with the progenitor being H-stripped (probably of WN type), exploding as a Type-I SN surrounded by a dense H-free, He-rich CSM as suggested by Pastorello et al. (2015). We can also not rule out the explosion of a small-mass, stripped-envelope star surrounded by a He-rich CSM which could have been ejected by a binary interaction.

Keywords: massive stars, CSM-interacting SNe, radiative transfer modelling

Acknowledgements

To my supervisor, Prof. José Groh, thank you for your patience and willingness to help me throughout. Your support has allowed me to develop in many ways. Thanks for all that you have taught me, as well as the many opportunities you have provided and entrusted me with.

My family, in particular my parents Malcolm and Jeanette, and sister Clodagh, thank you for the love and support. Your constant willingness to help and listen is much appreciated, as are the countless phone calls and early lifts.

Thanks to the many friends I made throughout my time at Trinity for making it so enjoyable. To those also in José's research group, Ioana, Laura and Eoin, thank you for guiding and assisting me, both in-person and online. It was a pleasure working amongst you. Many thanks also to Dualta, Stephen, Amanda, Rob, Kelly, Maxime, Pearse and Brendan for everything in and out of the office. I wish we could have returned before I finish. Thanks also to the broader astrophysics community in Trinity for being so welcoming. To my friends outside of Trinity, thanks for your interest in, and ability to make me forget, whatever I had been working on.

Many thanks to the co-authors of Allan et al. (2020) for your hard work both on the paper and the many press opportunities which followed. I also wish to acknowledge John Hillier for developing and maintaining the CMFGEN radiative-transfer code.

Last but certainly not least, I would like to thank the examiners for their willingness to evaluate this work. Thank you for all of the time you spend doing this. I hope you enjoy the read!

Contents

List of Figures

List of Tables

Contributions

Contributed Papers

1. Allan, Andrew P. and Groh, José H. *Type Ibn Supernovae - A detailed spectroscopic study using radiative transfer modelling with CMFGEN* (Manuscript in preparation)

2. Allan, Andrew P. and Groh, José H. and Mehner, Andrea and Smith, Nathan and Boian, Ioana and Farrell, Eoin J. and Andrews, Jennifer E., *The possible disappearance of a massive star in the low-metallicity galaxy PHL 293B* (Published in MNRAS496.2, pp. 1902–1908 in June 2020)

3. Groh, José H. and Farrell, Eoin J. and Meynet, Georges and Smith, Nathan and Murphy, Laura and Allan, Andrew P. and Georgy, Cyril and Ekstroem, Sylvia *Massive Black Holes Regulated by Luminous Blue Variable Mass Loss and Magnetic Fields* (Published in ApJ900 98 in September 2020)

Contributed Talks

1. Allan, Andrew P. Radiative Transfer Models of Eruptive Stars and Interacting Supernovae, UKRI STFC Introductory Course in Astronomy for New Research Students, January 2021

2. Allan, Andrew P. The Possible Disappearance of a Massive Star, Irish National Astronomy Meeting, September 2020

3. Allan, Andrew P. The Possible Disappearance of a Massive Star in a Low Metallicity Galaxy, Astrophysics Seminar at Trinity College Dublin, April 2020

Contributed Posters

1. Allan, Andrew P. Predicting progenitor properties of type-Ibn Supernovae using early-time spectral modelling, European Astronomical Society Annual meeting 2021 at Leiden (virtual)

2. Allan, Andrew P. End stages of massive star evolution at low metallicity: the possible collapse of an LBV in PHL 293b to a black hole, European Astronomical Society Annual meeting 2021 at Leiden (virtual)

3. Allan, Andrew P. PHL 293B: The possible disappearance of a massive star, Royal Astronomical Society Early Career Poster Exhibition, September 2020

Public Outreach Contributions

1. Press-release about the possible disappearance of a massive star in PHL 293B | July 2020, ESO, CNN, BBC, Forbes, 120+ outlets; estimated audience 1 million+
2. * Trinity Walton club, Transition Year Physics Experience (TYPE), March 2021
3. * I-LOFAR Teen camp, July 2020
4. * Radio Interview with Jonathan McCrea, Newstalk, Futureproof Science, August 2020
5. * Radio Interview with the Canadian Broadcasting Corporation, July 2020
6. * Podcast Interview with FunKids Science Weekly, July 2020

* General talks or interviews aimed at public outreach and the promotion of astrophysics, mainly through discussing the end-fates of massive stars.

Other Contributions

1. Volunteer technical-host for 6 sessions at the European Astronomical Society Annual meeting 2021 at Leiden (virtual), 28 June to 2 July

1. Organiser and host of the weekly Astronomy-Seminar at Trinity College Dublin, January to May 2021

1. Teaching assistant for the 'Practical in Astrophysics' undergraduate module at Trinity College Dublin, 2020 (IDL) and again in 2021 (Python)

1. Report grading and assistance for the 'Foundation Physics Practical Lab' undergraduate module at Trinity College Dublin, 2020

Chapter 1

Introduction
Massive stars and their end-fates

This thesis explores the spectroscopy of massive stars both during their end stages and terminal supernovae explosions. The research within is split into two main studies: the possible disappearance of the spectral signature of the luminous blue variable in PHL 293B (Chapter 3) and predicting the progenitor properties of Type-Ibn supernovae through modelling their early-time spectral observations (Chapter 4). In this chapter, the relevant background theory is discussed.

1.1 A brief overview of massive stars

Massive stars are highly important components of our Universe, being among the most prevalent sources of chemical elements. Compared to lower mass stars, their formation is rare (Salpeter, 1955) and their lifetimes considerably short (Ekström et al., 2012). Throughout their evolution, the cores of massive stars progressively produce elements up to Fe through the process of nuclear fusion. Furthermore, at the end of their evolution, their energetic terminal supernova (hereby SN) explosion disperse both energy and many elements heavier than Fe throughout the Universe leading to higher metallicity environments. Despite their importance to a number of topics in astrophysics, there is still a lot to be learned about massive stars. One such topic which would greatly benefit from further study is the link between SN and the nature of the progenitor star. We refer to massive stars as those with an initial mass $>8M_{\odot}$. Above this mass, electron degeneracy pressure in their core is negligible, unlike lower mass stars. Massive stars are believed to end their lives in a multitude of ways, such as a SN or direct collapse to a black hole (hereby BH) (Heger et al., 2003). The initial mass and composition greatly

dictate the type of massive star produced with minor variations often resulting in vastly different stars. This is particularly the case at late evolutionary stages, when the star has completed the main sequence phase of core H-burning, progressing on to heavier element burning.

1.2 Winds and mass loss in massive stars

Relative to lower mass stars, massive stars undergo much stronger mass loss owing to their much higher luminosities. This mass loss occurs for most of their evolution, including while they are on the main sequence (hereby MS), during which nuclear fusion of H occurs in the stellar core (Smith, 2014). mass loss affects many stellar properties including luminosity, temperature, radius, element abundances, lifetime and ultimately the end-fate of the star.

Massive stars are hot for the majority of their evolution, being mostly of OB-type during the MS. All hot stars host line-driven winds which are driven by absorption in spectral lines (Castor, Abbott, and Klein, 1975). They emit most of their photons in the UV where their atmospheres have a wealth of absorption lines. Ions of C, N, O and Fe absorb and re-emit UV photons (Lamers and Cassinelli, 1999). The ability of these species, in particular Fe, to absorb UV photons and drive the wind results in a metallicity dependence in the resulting mass loss. The momentum $\frac{h\nu}{c}$ of the photon is transferred to its absorbing ion. The photon is re-emitted in approximately an isotropic direction, whereas the initially absorbed photon travelled from deeper in the star. Therefore there is a net transfer of momentum from the photons to the absorbing ions (Puls, Vink, and Najarro, 2008). The absorbing ions then share some of their gained momentum with their non wind-driving companions via Coulomb coupling. Additionally, the larger velocity of potential absorbers further out in the atmosphere results in photons in these regions being increasingly red-shifted. Potential absorbers can hence absorb photons that are not absorbed lower down in the atmosphere making the line-driven wind highly efficient (Sobolev, 1960; Lamers and Cassinelli, 1999).

Due to the large influence mass loss has on the evolution of a star, many studies attempt to provide accurate prescriptions of wind mass loss, which are then adopted in stellar evolution codes. However, calculating the mass loss is a highly complex task which directly impacts the modelled evolution. Nevertheless, various prescriptions for steady line-driven mass loss exist in the literature. Vink, de Koter, and Lamers (2001) and de Jager, Nieuwenhuijzen, and van der Hucht (1988) (both shown in Fig. 1.1) remain the most popular prescriptions for modelling the winds of OB-type stars. Recent

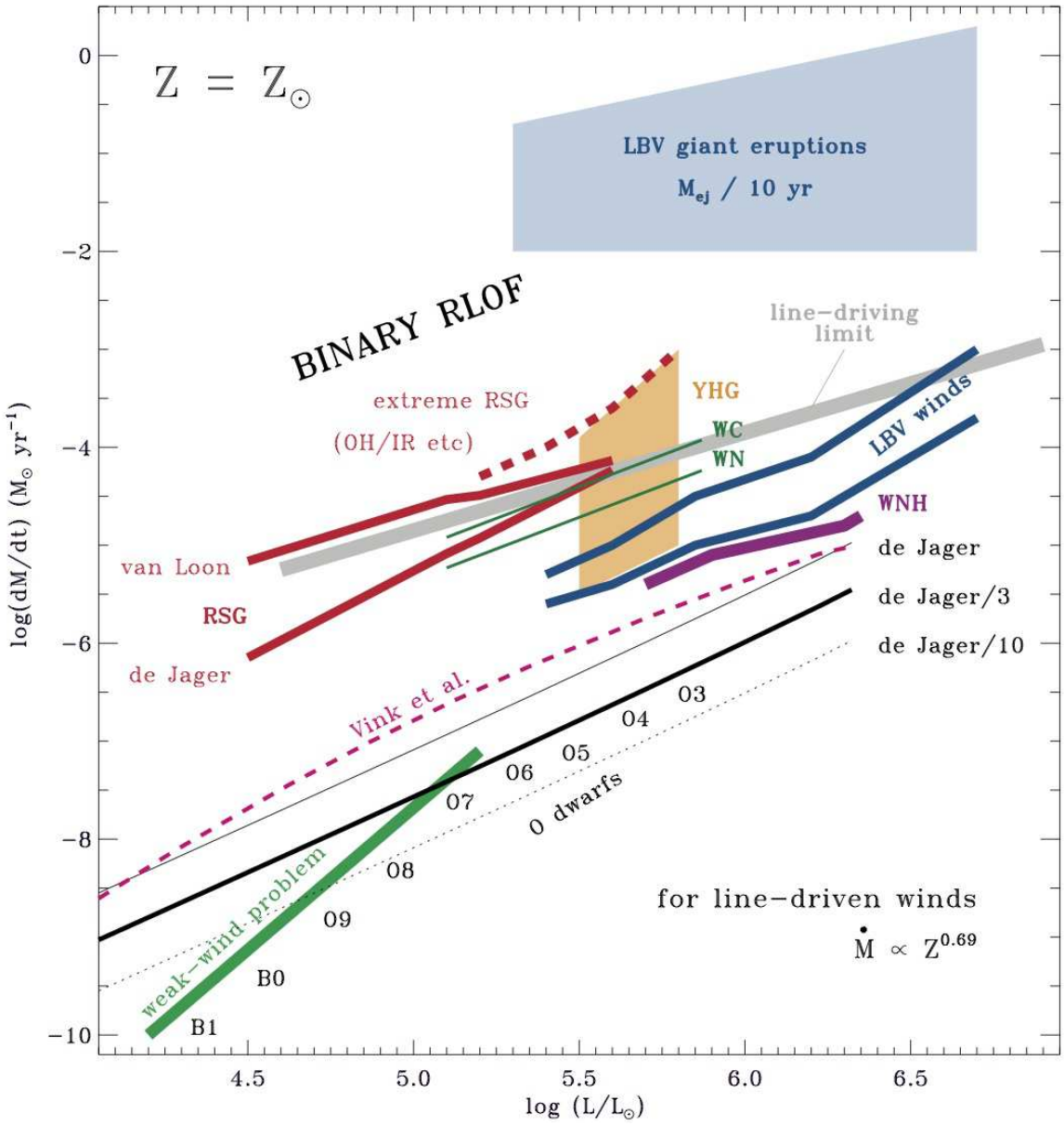

Figure 1.1: Various predictions of mass-loss rates as a function of luminosity for a number of different types of massive stars. See the review paper by Smith (2014, from which this figure was obtained) as well as the references within for detailed descriptions of the various prescriptions used in producing this figure.

alternative prescriptions include Björklund et al. (2021), Sundqvist et al. (2019), and Gormaz-Matamala et al. (2019). Current prescriptions for the line-driven winds of H-poor stars (see Sec. 1.4) include Nugis and Lamers (2000), Yoon, Langer, and Norman (2006) and the more recent Sander and Vink (2020). The latter prescription is unique in that it is physically motivated, based on dynamically consistent atmosphere models. Higgins et al. (2021) provides an in-depth comparison of the three mentioned H-poor mass loss prescriptions, finding that only the Nugis and Lamers (2000) prescription produces a convergence to a maximum BH mass. Hence, the Yoon, Langer, and Norman (2006) and Sander and Vink (2020) prescriptions suggest that the initial mass of the He star is the determining factor for the mass of the resulting BH, with pulsational pair instabilities instead causing the convergence of a maximum BH mass for He stars. The Vink, de Koter, and Lamers (2001) mass loss prescription for OB-stars is theoretically-based, employing a Monte-Carlo method to calculate the radiative acceleration of wind material by tracking the energy loss of photons through the wind. The de Jager, Nieuwenhuijzen, and van der Hucht (1988) prescription on the other hand is empirical, based on the predicted mass-loss rates of 271 stars. These popular prescriptions typically yield mass losses between $10^{-10} - 10^{-5}\ M_{\odot}\text{yr}^{-1}$ for OB-type stars. This is considerably lower than that predicted for luminous blue variables (Sec. 1.3) and Wolf-Rayet stars (Sec. 1.4). This is emphasised in Figure 1.1 in which the line-driving limit is roughly two orders of magnitude below the observationally based mass loss of LBV giant eruptions.

The physical origin of these giant eruptions remains an open question. Two popular hypotheses are hydrodynamic explosions (Smith, 2008) and continuum-driven super-Eddington winds (Owocki, Gayley, and Shaviv, 2004). Above the Eddington limit, stars are no longer gravitationally stable against radiation pressure. In the case of hydrodynamic explosions, Smith (2013) points out that CSM interaction could also prolong the eruption, as would be necessary to explain the $\sim$10 year long eruption of the LBV η-Carinae (discussed in Sec. 1.3). Interestingly, these hypotheses do not explain the 'root trigger' of the eruption. The cause of both the explosion and the ejected CSM in the hydrodynamic explosion hypothesis or the strong increase in luminosity necessary for the super-Eddington wind are not yet known. Smith (2014) and Smith et al. (2011b) discuss many potential 'triggers', none of which has been distinguished as a favourite as of yet. Smith (2014), Weis and Bomans (2020) and Davidson (2020) all offer in-depth reviews of the various proposed mechanisms for giant eruptions.

The incomplete understanding of the physical mechanism of eruptive mass loss combined with a lack of observationally-based mass-loss predictions at various

luminosities and metallicities means that mass lost through sporadic giant eruptions is not accounted for in current stellar evolutionary modelling. Vink and de Koter (2002) offers a prescription for the strong line-driven winds of luminous blue variables (Sec. 1.3). Omitting giant eruptions in stellar evolutionary models however is an important problem considering their ability to vastly alter the evolutionary path of the star. In extreme cases, an eruption can expel more mass than is shed in the time that the star is on the main sequence. Furthermore, giant eruptions are believed to occur in the very late stages of a star's life (Ofek et al., 2014), largely impacting the resulting SN and remnant.

1.3 Luminous Blue Variables (LBVs)

As the name[1] suggests, luminous blue variables (hereby LBVs) are typically bright, hot stars with variable properties (Smith, 2017b; Vink, 2012; Humphreys and Davidson, 1994). Weis and Bomans (2020) however point out that this is a weak constraint for LBVs. The detection of either S-Doradus variability or a giant eruption are the only true signatures distinguishing LBVs from other massive stars. 'LBV candidates' however, are spectroscopically similar to quiescent LBVs but have yet to be observed to undergo either a giant eruption or S-Doradus cycle (Smith, 2014). Separate from the giant eruptions discussed in Section 1.2, S-Doradus variability refers to both photometric and spectroscopic variations over the period of an 'S-Doradus' cycle which can last years or decades (van Genderen, de Groot, and Sterken, 1997; van Genderen, 2001). During the S-Doradus cycle, the star can brighten by 1 to 2 magnitudes at visual wavelengths (Humphreys, Davidson, and Smith, 1999). S-Doradus episodes are not major sources of mass loss in comparison to giant eruptions which can cause LBVs to lose between 10^{-2} to 1 $M_{\odot}\text{yr}^{-1}$, more than that predicted for any other spectral type (see Fig. 1.1). LBVs exhibit a line-driven wind (Vink and de Koter, 2002), however, as shown in Figure 1.1 this line-driven mass loss is of the order of 10^{-5} to 10^{-4} $M_{\odot}\text{yr}^{-1}$. Terminal wind velocities of LBVs are typically between 100-250 km s^{-1} (Vink, 2012), below that of the $\sim$1000-3000 km s^{-1} of normal OB supergiants. The slower wind velocity, combined with the stronger mass-loss rates of LBVs results in considerably denser winds (see Eq. 2.9), giving LBVs their characteristic P-Cygni line profiles (Vink, 2012).

Giant eruptions can cause LBVs to brighten by up to 5 magnitudes (Humphreys and Davidson, 1994). The primary star of the well-known η-Carinae system is an example of such an LBV, which underwent a giant eruption in the 1840s, during which it became

[1]first coined by Peter Conti in a talk (Conti, 1984) at the IAU Symposium.

the second brightest star in the sky (Humphreys, Davidson, and Smith, 1999). In this extreme case, $\eta-$Carinae apparently maintained an Eddington factor (ratio of Newtonian acceleration to the radiative acceleration due to electron scattering) of $\sim$5 for over a decade. This supports the hypothesis previously mentioned in Section 1.2 of Super-Eddington winds being responsible for eruptive mass loss. Even in their quiescent state, LBVs approach the Eddington limit owing to their high luminosity to mass ratio. Other well-known LBVs include AG Carinae (Groh et al., 2009) and P-Cygni (de Groot, 1988).

Similar to their giant eruptions, the true physical mechanism for the S-Doradus variability of LBVs is uncertain. Recent work by Grassitelli et al. (2021) identified a wind-envelope interaction as the cause of S-Doradus variability. Another potential explanation is the crossing of the bi-stability limit at a critical temperature $\sim$21000 K when the LBV evolves from hotter to cooler temperature resulting in recombinations of dominant line-driving ions (Lamers, Snow, and Lindholm, 1995; Vink, de Koter, and Lamers, 1999; Smith, Vink, and Koter, 2004). These recombinations increase the mass-loss rate and lower the wind velocity with Vink, de Koter, and Lamers (1999) predicting a rise in mass-loss rate of a factor of 5 and a velocity drop of a factor of 2 when Fe recombines from Fe IV to Fe III at the critical temperature. Petrov, Vink, and Gräfener (2016) use CMFGEN to investigate the bi-stability limit for LBV stars, finding a second bi-stability (previously predicted by both Lamers, Snow, and Lindholm (1995) and Vink, de Koter, and Lamers (1999)) jump at $\sim$8800K at which Fe III starts to recombine to Fe II.

The LBV phase appears to occur late in the evolution of particularly massive stars with Smith, Vink, and Koter (2004) predicting a mass $>$25 $M_{\odot}$ assuming a single star evolution. In stellar timescales the LBV phase is relatively short with prediction timescales of a few 10^4 years (Humphreys and Davidson, 1994; Weis and Bomans, 2020). This short timescale is consistent with the noted rareness of LBVs. The traditional belief is that the LBV phase occurs within the transition between O-type core H-burning to WR core He-burning (Humphreys and Davidson, 1994). Observational and theoretical evidence suggesting that LBVs are in SNe progenitors however seems to contradict this view. For example, the stellar evolution models such as those of Groh, Meynet, and Ekström (2013) and Groh et al. (2019) suggest that some of the most massive stars end their evolution as LBVs (e.g., Humphreys and Davidson, 1994; Maeder and Meynet, 2000; Groh et al., 2014). Consistent with this picture, progenitors of a number of SNe are predicted to have been LBVs such as SN 2013cu (Groh, 2014), SN 2005gl (Gal-Yam and Leonard, 2009), SN 2010jl (Smith et al., 2011a), SN 2008ax (Groh, Meynet, and Ekström, 2013), SN 2015bh (Boian and Groh, 2018), SNe 1979C, 1998bw, 2001ig and 2003bg (Kotak and

Vink, 2006). Another problem with the traditionally believed timing of the LBV phase includes LBVs being more isolated than WR stars as found by Smith and Tombleson (2015) who suggest that the LBV phase may instead be reached through binary evolution. These disagreements with the traditional belief and more are discussed thoroughly in the recent review by Smith (2017b). For more detailed discussions on LBVs see also the following review papers: Weis and Bomans (2020), Vink (2012) and Humphreys and Davidson (1994).

1.4 Wolf-Rayet stars

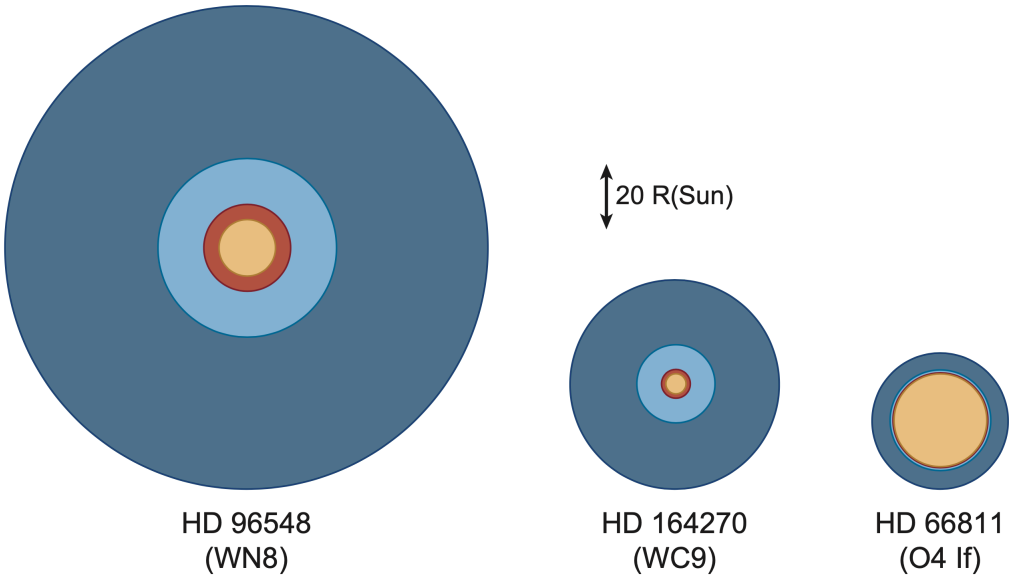

Figure 1.2: Illustration (from Crowther, 2007) depicting the extended nature of the dense line-driven winds of WRs (left and middle) compared to Of-type supergiants (right). The winds of LBVs follow a similar physical structure to that shown here for WRs. The greatly extended line forming regions of WRs (and LBVs) are coloured in dark blue. The electron density in these regions range from $10^{11} - 10^{12}$ cm^{-3}. Light blue indicates even higher density material. Red and orange regions have Rosseland optical depths of 20 and 2/3 respectively. The separation of these two regions highlights why we calculate $T_\star$ in addition to $T_{\rm eff}$, as will be further discussed in Section 3.3.

Wolf-Rayet[2] (hereby WR) stars have been entirely stripped of their H envelopes exposing a bare He core. This is evidence of either strong mass loss via winds or through interaction with a binary companion. Candidates for the prior stage of evolution vary with

[2]named after their discoverers (Wolf and Rayet, 1867).

stellar mass, with red supergiants (RSGs) predicted for masses between 25–30 $M_{\odot}$ and LBVs above 30 $M_{\odot}$ assuming a single star evolution (Crowther, 2007). The spectra of WR stars feature strong, broad emission lines which form far out in their strong, fast, high-density line-driven winds. These winds can reach terminal velocities between 700-4100 km s^{-1} and can produce mass losses of $\sim 10^{-5}$ $M_{\odot}yr^{-1}$ (Crowther, 2007). The extended nature of the line formation region of WR (and LBV) stars is illustrated in Figure 1.2. WR stars are sub-classified based on the prominent element other than He seen in their spectra with WC, WN or WO implying strong C, N or O emission, respectively. WRs are quite rare with estimated lifetimes of a few 10^5 years (Meynet and Maeder, 2005). Their rarity seemingly increases in very metal-poor regions (Crowther and Hadfield, 2006). However surveys have detected evolved WR stars in the Small Magellanic Cloud (SMC) (Massey, Olsen, and Parker, 2003; Massey et al., 2014; Neugent, Massey, and Morrell, 2018; Shenar et al., 2020) and I Zw 18 galaxy (Izotov et al., 1997; Legrand et al., 1997; Brown et al., 2002).

1.5 The end-fate of massive stars

Massive stars can end their lives in a variety of fashions. The star's final fate is highly dependant on both its initial mass and the mass loss throughout its lifetime. Evolutionary models can predict the end-fate of massive star as a function of initial mass and metallicity as shown in Figure 1.3. In creating this figure, Heger et al. (2003) assume single star evolution, neglecting mass loss arising through interaction with a binary companion. Above an initial mass of $\sim$10 $M_{\odot}$, formation and collapse of an Fe core is expected.

The initial mass and metallicity dictate whether a neutron star or BH remnant remains and whether a BH is formed through direct collapse or fallback. They also affect the nature of the accompanying SN explosion. At low metallicities, the end fate depends mostly on the initial mass as this sets the mass of the He core at the time of collapse. At larger metallicities, mass loss becomes increasingly important leading to a smaller He core for a given initial mass. This results in the increasingly skewed nature of the predicted boundaries at higher metallicities in Figure 1.3. The mass and composition of the envelope and the time of explosion dictate the classification of the SN which would be produced, with a H-free envelope resulting in a type Ib, while more (less) than 2 $M_{\odot}$ of H in the envelope is predicted to produce a Type-IIp (Type-IIL) (Heger et al., 2003). Figure 1.3 does not include interacting SNe, which will now be discussed.

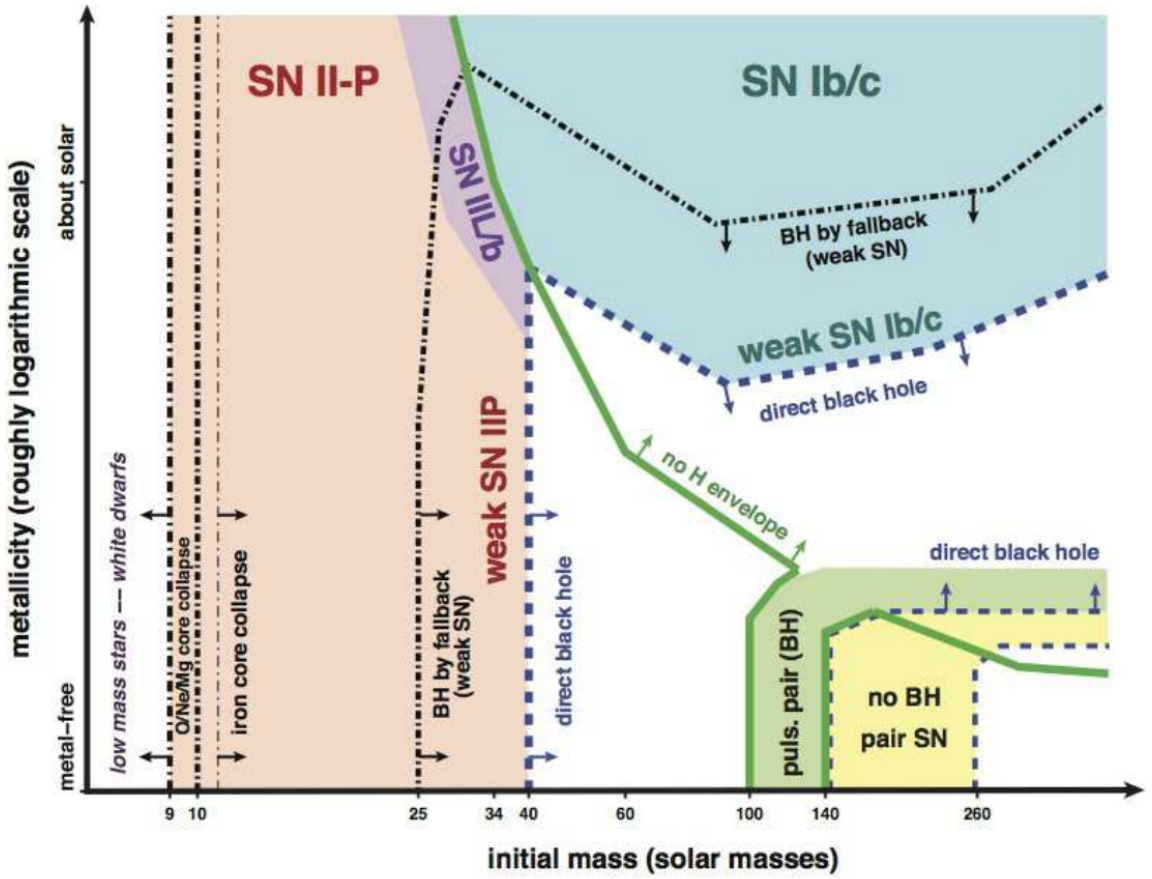

Figure 1.3: Predicted end-fates of massive stars as a function of initial mass and metallicity assuming a single star evolution. From Smith (2014) who adapted the figure from (Heger et al., 2003).

1.5.1 CSM-Interacting Supernovae

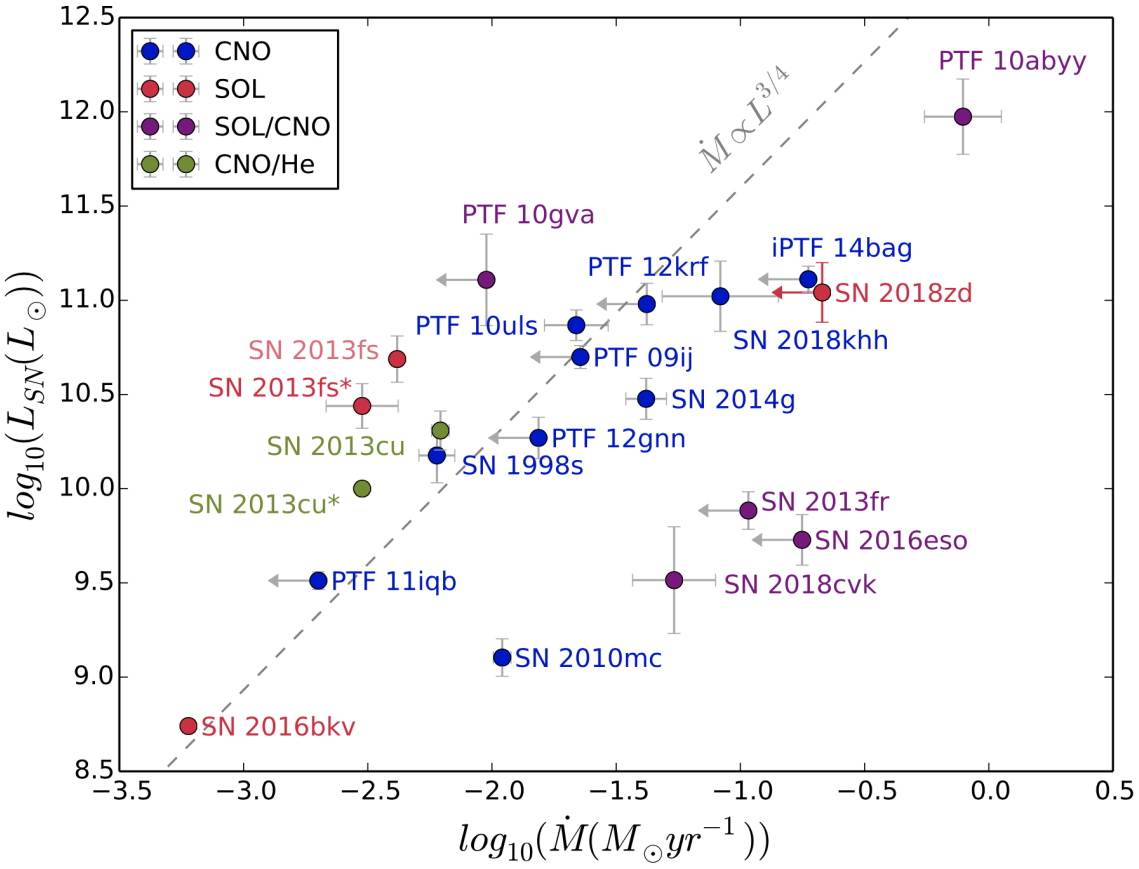

Figure 1.4: Various moss loss rates and luminosities predicted with CMFGEN modelling for the interacting SNe sample of Boian and Groh (2020, from which the figure was obtained). The scaling of $\dot{M} \propto L^{0.75}$ from Gräfener and Vink (2016) is also shown.

The previous section mentioned that the properties of a massive star determine the nature of its end-fate. This statement holds true for the class of circumstellar medium (hereby CSM)-interacting SNe, with the CSM and explosion energy being intricately dependent on both the mass-loss rate and metallicity. All SNe interact with whatever material surrounds them. Those which are classified as CSM-interacting however, are simply surrounded by material in the form of a CSM which is sufficiently dense to produce clear spectral signatures of interaction with the SN ejecta when the star explodes. Dependent on whether this CSM is H-rich or H-poor, the SN is classified as type-IIn (Schlegel, 1990) or type-Ibn (Sec. 1.5.2), respectively. Transitional events between these two classifications in which H and He I lines have similar emission strengths have also been

detected such as SN 2005la (Pastorello et al., 2008) and SN 2011hw (Smith et al., 2012; Pastorello et al., 2015)

In both classifications, the CSM matter is likely expelled directly from the progenitor star creating a link between its observable properties and the progenitor star. The composition of the CSM is then representative of that of the outer regions of the progenitor star when it exploded. The stellar wind velocity may also be approximated by the CSM velocity in the case that the CSM was formed steadily by a line-driven wind. Figure 1.4 displays predictions of the SN luminosity and the progenitor mass-loss rate for a number of Type-IIn SNe events. These were obtained through spectral fitting with CMFGEN which allows for predictions of CSM and consequently progenitor properties (see Sec. 2.2). The mass-loss rates required to produce the necessarily dense CSMs for producing the observed spectral signatures are considerably greater than that expected for line-driven winds. The higher rates may be more consistent with the CSM forming very soon before explosion through unstable giant eruptions such as those exhibited by LBV stars. A direct observation of such a pre-SN outburst was made in the case of the prototypical Type-Ibn SN 2006jc (Foley et al., 2007; Pastorello et al., 2007). A binary interaction could also produce the CSM, likely giving it an asymmetric nature. A number of observations of interacting-SNe have been explained with an asymmetric CSM including SN 1998S (Leonard et al., 2000), PTF11iqb (Smith et al., 2015) and SN 2012ab (Bilinski et al., 2018). For simplicity however, our models (Sec. 2.2) assume a spherically symmetric CSM. Depending on both the density and extent of the CSM, an interacting SN can remain bright for years as opposed to months, as is usually the case for non-interacting SNe.

Figure 1.5 illustrates the explosion process of an interacting SN assuming a spherically symmetric CSM consistent with our models. The explosion of the progenitor propels fast moving ejecta (10^4 km s^{-1}) into the surrounding slower moving CSM (50-1000 km s^{-1}). This ejecta-CSM interaction forms both a forward- and reverse-shock. In this interaction, kinetic energy from the SN explosion is converted into radiative energy (Chevalier and Fransson, 2017) with as high as 50% efficiency, meaning a lower explosion energy is required compared to a non-interacting SN in order to achieve the same luminosity (Smith, 2017a). Hence, it is perhaps not surprising that this highly efficient interaction is one of the proposed powering mechanisms for producing super-luminous supernovae SLSN (Dessart, Audit, and Hillier, 2015) (as suggested for SN 2006gy Ofek et al., 2007), with spinning down magnetars and radioactive decay providing alternative mechanisms (Moriya, Sorokina, and Chevalier, 2018). The forward-shock propagates through the CSM material

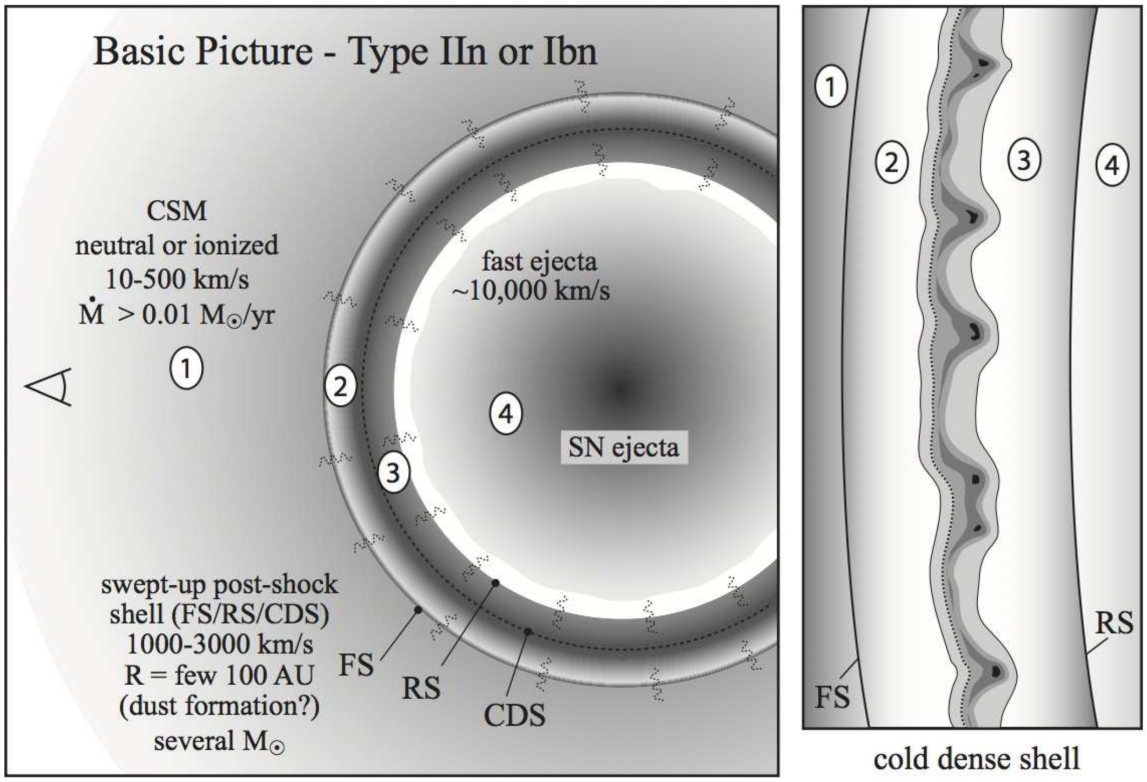

Figure 1.5: Illustration from Smith (2017a) of the various zones produced in the interaction between fast moving SN ejecta with the slow moving CSM. The zones are indicated by number, with zone (1) being pre-shock CSM, (2) shocked CSM, (3) shocked SN ejecta, (4) freely expanding SN ejecta. As indicated, these zones are separated by the forward shock (FS), reverse shock (RS) and the contact discontinuity between the shocked CSM and shocked ejecta, also known as the cold dense shell (CDS). The panel on the right displays a close-up illustration of the CDS.

resulting in the formation of shocked and unshocked CSM zones as shown in Figure 1.5. The reverse-shock, on the other hand, travels inwards towards the expanding ejecta leading to zones of decelerated ejecta which have encountered the reverse-shock and freely expanding ejecta which have yet to. Signatures from material in the mentioned zones appear during different stages in spectral observations of the SNe. At the onset of the CSM-ejecta interaction, the CSM is ionised by radiation from the shock. The photosphere resides in the unshocked region of the CSM at this stage, temporarily obscuring the interaction (Smith, 2017a). The early-time spectra consists of a smooth blue continuum overlaying with narrow emission lines exhibiting broad Lorentzian wings; the wings arising from electron scattering. It is the presence of these narrow (n) lines that distinguishes Type-IIn/Ibn SNe from non-interacting SNe. In non-interacting SN, the picture is much

simpler, with only spectral signatures of the freely expanding SN ejecta. For such SNe, the spectra exhibit decreasingly broad emission and absorption lines as the velocity of the ejecta declines.

1.5.2 Type-Ibn supernovae

We focus primarily on SN Ibn. These events are considerably rare compared to other SN classifications, with less than 40 events presently reported in the literature (Hosseinzadeh et al., 2019). These explosions are believed to originate from the collapse of their progenitor's core. At the time of explosion, an Ibn progenitor star is surrounded by a H-poor, He-rich CSM composed of material expelled from the progenitor at an earlier stage. The physics of how this CSM is formed remains an open area of study, with stellar winds and late-time explosions offering potential answers. As explained in Section 1.5.1, the spectra of SN-Ibns exhibit signatures arising from the interaction between the ejecta of the SN explosion and the surrounding CSM. These signatures are strong, narrow (a few 10^3 km s^{-1}) He emission lines at early-times (Matheson et al., 2001; Foley et al., 2007; Pastorello et al., 2007). These narrow He lines are likely generated by photo-ionised material in the pre-shocked region of the He-rich CSM. Hosseinzadeh et al. (2017) compare the observed spectra of a sample of Type-Ibn SNe finding some diversity in the spectra at early times with some exhibiting P-Cygni lines superimposed on a blue continuum while others exhibit broader features similar to SN-2006jc. In comparison to type-IIn SNe however, the spectra of Type-Ibn SNe are considerably less diverse. Hosseinzadeh et al. (2017) also find a surprising homogeneity in the fast-evolving light curves of Type-Ibn SNe compared to their H-rich Type-IIn counterparts. This is possibly the result of the higher density He-rich CSM requiring a much stronger pre-explosion eruption or wind, in order to be expelled from the progenitor. Considering that only a sufficiently high energy would thus be capable of producing the Ibn CSM, it makes sense that Ibn CSMs would vary less from event to event compared to IIn CSMs which can form over a much wider range of wind or eruption energies.

All but one of the SN Ibn events detected thus far have been found in actively star forming spiral galaxies, indicative of a massive star origin for Type-Ibn SNe. Hence, massive WR stars which for an unknown reason undergo a giant eruption prior to explosion are popular progenitor candidates as a result of their H-poor nature (Smith, 2017a). In the case of SN2006jc, a giant outburst occurred at the progenitor location just two years before this SN explosion (Pastorello et al., 2007). Sanders et al. (2013) however revealed

that a massive star origin is not necessarily the case with their finding of PS1-12sk, an SN Ibn which appeared to explode on the outskirts of the brightest elliptical galaxy in a galaxy cluster. The very low star formation rate of such an environment makes a massive star origin for PS1-12sk highly unlikely. This was further emphasised by Hosseinzadeh et al., 2019 who use deep UV imaging taken with the Hubble Space Telescope to strengthen the initial star formation limit by an order of magnitude, revealing it to be less than that of all previous core collapse SNe. They offer three potential explanations for the progenitor of PS1-12sk: a massive star ejected or tidally stripped from a nearby ultra-compact dwarf galaxy, a rare massive star in a region with a very low star formation rate or a low mass star such as a white dwarf in a He envelope or a non-degenerate He star.

1.5.3 SN2010al: A Type-Ibn SNe with early-time spectroscopy

In this thesis, we focus on SN2010al, a type-Ibn SN which exploded in the edge-on spiral galaxy UGC 4286 located 71.6 Mpc away (Rich, 2010). It remains one of the earliest spectroscopically observed SN Ibn events, with the archival spectrum fitted in Section 4.3 obtained just 5.7 days post-explosion using the FAST spectrograph of the Tillinghast Telescope (Fabricant et al., 1998). For consistency, we adopt the predicted explosion date of JD=2455268.0 $\pm$ 1.5 based on pre-discovery non-detections by routine observations performed with the 0.4-m MASTER telescope at Kislovodsk, Russia. In their study of SN2010al, Pastorello et al. (2015) noted that this early specrum is dominated by a blue continuum, with narrow P-Cygni He I lines indicating the presence of a slow- moving, He-rich circumstellar medium. They also highlight spectral similarities at later times with the prototypical SN Ibn 2006jc, with broader lines indicating that a significant amount of He was still present in the stellar envelope at the time of the explosion. They predict from their detailed analysis of the photometric and spectroscopic observations that SN2010al is a Type Ib SN that exploded in a H-poor, He-rich CSM, suggesting that the progenitor was H-stripped and in the process of losing its He at the time of explosion. A suitable progenitor for such evolution would be a WR star possibly of WN Type.

1.5.4 Direct core collapse to a black hole

While massive stars are typically seen to end their lives in extremely bright SNe explosions, both observational and theoretical evidence exist which suggests that this may not always be the case. In the case of a failed SNe, the core may collapse to a black hole (hereby BH) without a luminous SN. For a successful core-collapse SN, either a neutron star or

light BH is left as a remnant, whereas in a failed SN most of the stars mass collapses into the BH producing a more massive (>20$M_{\odot}$) BH (Mapelli, 2021). Models such as that of O'Connor and Ott (2011), Lovegrove and Woosley (2013), and Sukhbold et al. (2016) have predicted a non-monotonic behaviour of SN explodability with stellar mass, suggesting the presence of "islands of explodability".

The famous N6946-BH1 event provides the most clear-cut observational evidence for the collapse to a BH without a bright transient (Adams et al., 2017a; Adams et al., 2017b). This is an exciting result considering the observational difficulties associated with detecting events which by definition do not produce an easily observed bright transient. In this interesting case, a Red Super Giant (RSG) seemingly disappeared in optical wavelengths after undergoing an outburst in 2009. Continued follow-up observations as described in Basinger et al. (2020) find no evidence for a re-brightening of the star, with the candidate failed SN remaining 1% as luminous as its progenitor RSG. They also rule out obscuration by either dust or an ongoing wind due to the absence of a counterpart in the IR and the fact that the star has yet to reappear. In addition to this event, thus far there have been only two other photometric detections suggestive of the direct collapse to a BH without a bright transient, namely a ∼25-30 $M_{\odot}$YSG in NGC 3021-candidate (Reynolds, Fraser, and Gilmore, 2015) and a ∼12 $M_{\odot}$BSG in M101-0C1 (Neustadt et al., 2021). In Allan et al. (2020), we propose the possible *spectral* disappearance of a massive LBV star. The collapse of the star's core to a BH without the production of a bright transient is one of the three scenarios we propose to explain this disappearance, as will be discussed. This hypothesis separates PHL 293B from the previous possible detections of direct BH collapse mentioned above as they were photometrically- rather than spectroscopically-based.

1.6 An LBV in the low metallicity dwarf galaxy PHL 293B

As discussed in Section 1.3, the LBV phase is currently a poorly understood late stage in the evolution of massive stars. Owing mainly to a scarcity of observations, our understanding of LBVs is even less complete in low metallicity (Z) environments. In an effort to improve upon this, in Allan et al. (2020) we monitored the blue compact dwarf (hereby BCD) galaxy PHL 293B which previous studies indicated hosted an LBV star. Allan et al. (2020) accordingly forms the basis for much of this thesis.

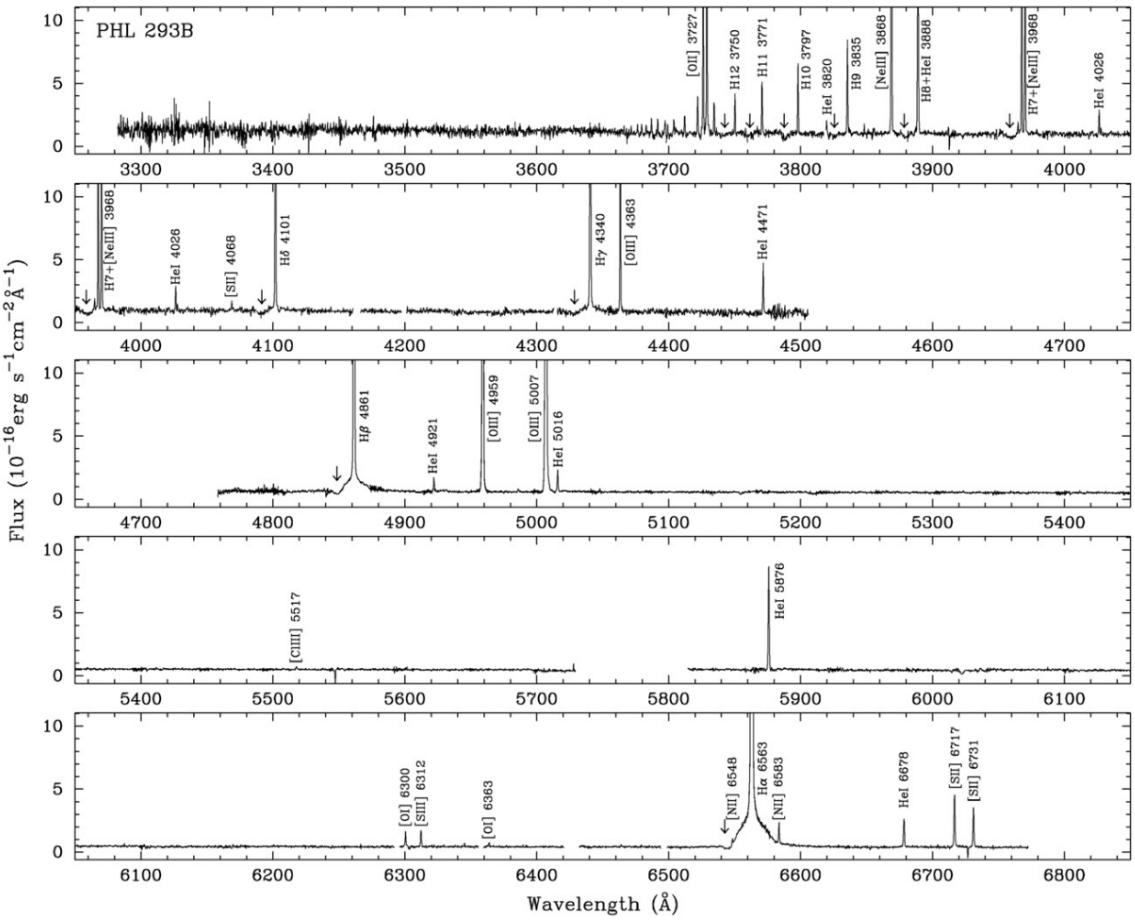

Figure 1.6: Archival redshift-corrected spectrum of PHL 293B taken with the UVES instrument of the Very Large Telescope in 2002 (Izotov and Thuan, 2009). The locations of blue-shifted absorption in lines with P-Cygni profiles are shown by arrows.

PHL 293B resides at a large distance of 23.1 Mpc (Mould et al., 2000), and has a metallicity of $Z \simeq 0.1Z_{\odot}$ (Izotov, Thuan, and Stasińska, 2007). Spectroscopic observations of the compact galaxy obtained between 2001–2011 consistently featured broad, strong emission components in the H Balmer lines. These spectral features are seen in Figure 1.6 and have been interpreted to originate in the outflow of an LBV star (Izotov and Thuan, 2009; Izotov et al., 2011), since together with the presence of Fe II and weak He I lines, only LBVs show these types of signatures (see discussion in Sects. 2.4 and 3 of Groh et al., 2014). The broad wings on the Balmer recombination lines arise due to electron scattering and consequently scale with the electron density. The earlier spectra of PHL 293B were remarkably similar, with the Balmer lines differing mainly in the strength of their narrow components, likely due to the different aperture size used in each observation. This narrow component is not believed to originate from the LBV, but

rather from a region of H II ionised by many O-type stars (Izotov et al., 2011).

Photometric analysis of PHL 293B revealed no optical photometric variability at the level of 0.1 magnitudes between 1988 and 2013 (Terlevich et al., 2014). Based on this, (Terlevich et al., 2014) suggested that the blue-shifted absorptions of H I and Fe II were not caused by an LBV, but instead by an expanding super-shell generated by the cluster wind of PHL 293B. The substantial spectral variation we report disfavours such a hypothesis. Burke et al. (2020) also report the weakening of the broad H Balmer components based on 2019 Gemini data. In addition, they report photometric variability of 0.12 magnitudes in the g band between 1998 and 2018, using images from the Sloan Digital Sky Survey (SDSS) and the Dark Energy Survey (DES). They suggest a SN IIn or an unusual outburst as the source of the broad components in the 2001–2011 spectra. While we do not rule out this hypothesis, in Section 3.5, two alternative scenarios for the apparent disappearance of the LBV are discussed.

Chapter 2

Spectral modelling with CMFGEN

This chapter presents the general techniques of our modelling. Section 2.1 first covers relevant theory prerequisites. We utilise the publicly available radiative transfer code CMFGEN (Co-Moving Frame GENeral, Hillier and Miller, 1998), as discussed in Section 2.2. More specific modelling descriptions for PHL 293B and Type-Ibn SNe are saved for the subsequent chapters in Sections 3.3 and 4.1, respectively.

2.1 Prerequisites from radiative transfer theory

Radiative transfer (hereby RT) refers to the study of the propagation of radiative energy through a medium. The study of RT is essential to our understanding of various astrophysical environments. This section briefly covers some of the theories of RT relevant to our modelling. For more detailed descriptions of RT theory, Rutten (2003), Crivellari, Simón-Díaz, and Arévalo (2019) and Rybicki and Lightman (1986) are all excellent resources and were instrumental in forming this chapter.

2.1.1 Mathematically describing the radiation field

The study of RT allows astronomers to gain an understanding of the microscopic properties of astronomical objects through spectral-based predictions of macroscopic properties such as the stellar temperature and luminosity. To achieve this, a mathematical description for the transfer of radiative energy is required. The specific intensity $I_\nu(\mathbf{r}, t; \mathbf{n})$ is a macroscopic property used in describing energy transport in the radiation field. Consider an area dA at location $\mathbf{r}$ with normal direction $\mathbf{n}$. Photons with frequencies between ν and $\nu+d\nu$ travelling within a solid angle $d\Omega$ from the normal $\mathbf{n}$, transport the energy dE_ν through the area dA in the time dt. That is to say:

$$dE_\nu = I_\nu(\mathbf{r}, t; \mathbf{n})\ dA\ dt\ d\nu\ d\Omega. \tag{2.1}$$

As radiation propagates through a material, some of the radiation will interact with the matter altering the properties of the radiation field. This process is described mathematically by the RT equation. Assuming azimuthal symmetry and adopting a spherical geometry with radial coordinate r, angular coordinate $\mu = cos\theta$ where θ is the polar angle, the RT equation is expressed as:

$$\frac{\partial}{\partial t}\frac{I_\nu(r,t;\mu)}{c} + \mu\frac{\partial I_\nu(r,t;\mu)}{\partial r} + \frac{1-\mu^2}{r}\frac{\partial I_\nu(r,t;\mu)}{\partial \mu} = \eta_\nu(r) \ - \ \chi_\nu(r) I_\nu(r,t;\mu) \tag{2.2}$$

where $\chi_\nu(\mathbf{r})$ is the extinction (absorption and scattering) coefficient while $\eta_\nu(\mathbf{r})$ is the emission coefficient. $\eta_\nu(\mathbf{r})$ gives the fraction of energy emitted by a volume dV into a solid angle $d\Omega$ in time dt per frequency band $d\nu$ while $\chi_\nu(\mathbf{r})$ gives the fraction of I_ν absorbed per unit length. Their ratio forms the source function $S_\nu = \frac{\eta_\nu}{\chi_\nu}$, a function commonly used in RT theory. These coefficients allow for the effects of radiation-matter interactions, such as spontaneous or stimulated emission and absorption, to be accounted for in our models[1]. These extinction and emission processes can be accurately calculated granted that the atomic level populations are known. The RT equation (Eq. 2.2) simply states that the radiation field varies only if photons are lost (extinction) or gained (emission).

2.1.2 Thermodynamic Equilibrium

The properties of an object in a state of thermodynamic equilibrium (hereby TE) are both isotropic and homogeneous. In TE, the source function describing the radiation field is given directly by the Plank function while the atomic level populations are given by the Saha-Boltzmann equations. Accordingly, both the radiation field and atomic levels can be defined using a single global temperature. The deep interior of a star is a close approximation to a state of TE. If in TE, a body behaves as an ideal blackbody. This allows it to be described by the Stefan Boltzmann Law which states that the flux emergent from a blackbody is proportional to the fourth power of its temperature:

$$F_{BB} = \frac{L_{BB}}{4\pi R^2} = \sigma T_{\text{eff}}^4 \tag{2.3}$$

[1] Sec. 2.9 of Crivellari, Simón-Díaz, and Arévalo (2019) gives detailed descriptions of such transitions.

where F_{BB}, L_{BB}, R_{BB} and $T_{\rm eff}$ are the flux, luminosity, radius and temperature of the blackbody while $\sigma = 5.67 \times 10^{-5}$ erg cm^{-2} s^{-1} K^{-4} is the Stefan Boltzmann constant.

2.1.3 Non-Local Thermodynamic Equilibrium

Local thermodynamic equilibrium (LTE) holds in environments less extreme than the deep stellar interior such as the photosphere of some stars. In LTE, a local region with temperature $T_{\rm local}$ is essentially in TE, with its radiative and atomic properties now functions of $T_{\rm local}$. However, in environments such as the outer region of the CSMs modelled in Chapter 4, even LTE is not satisfied. The radiation and matter are then in a state of Non-Local Thermodynamic Equilibrium (hereby NLTE). Fortunately, CMFGEN (described in Sec. 2.2) is capable of modelling NLTE environments. It achieves this through the non trivial task of simultaneously solving the RT (Eq. 2.2) and statistical equilibrium (Eq. 2.4) equations as will be explained in Section 2.2.1. The assumption of statistical equilibrium (SE) states that atomic level populations do not vary with time. That is:

$$n_j \sum_{i \neq j} P_{ji} = n_i \sum_{i \neq j} P_{ij} \tag{2.4}$$

where n_i is the occupation number of state i while P_{ij} is the probability of transitioning from state i to state j, and vice versa. CMFGEN also assumes radiative equilibrium in which the radiative energy absorbed by a medium equals that leaving the medium. This is expressed mathematically with the radiative equilibrium equation:

$$\int_0^\infty \kappa_\nu (J_\nu - S_\nu)\, d\nu = 0 \tag{2.5}$$

where κ_ν is the frequency dependent opacity and J_ν is the mean intensity obtained by averaging the specific intensity over all directions $J_\nu = \frac{1}{4\pi} \int I_\nu d\Omega$. CMFGEN uses radiative equilibrium to obtain a temperature structure as follows. An initial temperature structure estimation $T(\tau_{\rm Ross}(R))$ is first made with:

$$T^4(\tau_{\rm Ross}(R)) = \frac{3}{4} T^4_{\rm eff}(\tau_{\rm Ross} + q(\tau_{\rm Ross})) \tag{2.6}$$

where $T_{\rm eff}$ is the effective temperature, calculated using the Stefan Boltzmann law, (Eq. 2.3), $\tau_{\rm Ross}(R)$ is the mean Rosseland optical depth obtained by $\tau_{\rm Ross} = \int_0^s \kappa_{\rm Ross}(s)\rho(s)\, ds$ where $\rho(s)$ is the density profile and the integral is over the optical path ds. $q(\tau_{\rm Ross}(R))$

is the Hopf function which varies from 0.57 to 0.71 going from $\tau_{\text{Ross}}(R) = 0$ to ∞. The Rosseland mean opacity κ_{Ross} is a weighted average in which frequencies where the opacity is small or the temperature gradient is large tend to dominate:

$$\kappa_{\text{Ross}} = \frac{\int_0^\infty \frac{\partial B_\nu(T)}{\partial T} d\nu}{\int_0^\infty \frac{1}{\kappa_\nu} \frac{\partial B_\nu(T)}{\partial T} d\nu} \tag{2.7}$$

where $B_\nu(T)$ is the Planck function. To obtain the temperature structure the RT equation is first solved in LTE for J_ν using the Planck function with the initial temperature estimate as the Source function: $S_\nu = B_\nu(T(\tau_{\text{Ross}}(R)))$. If radiative equilibrium does not hold when substituting the resulting J_ν into Equation 2.5 then $T(\tau_{\text{Ross}}(R))$ is adjusted and the process is repeated.

2.2 CMFGEN - A radiative transfer model

Our modelling makes use of the publicly available one-dimensional RT code CMFGEN (Co-Moving Frame GENeral, Hillier and Miller, 1998) developed by Professor D. John Hillier. We use this code to compute both continuum and line formation in both the spectra of CSM-interacting SNe and dense outflows of massive stars. In our modelling the spectra of Type-Ibn SNe, we adopt H-free variations of the CSM-interacting CMFGEN models of Groh (2014) and Boian and Groh (2020). In our spectral modelling of the outflow of the LBV in PHL 293B, we adopt a similar approach to that taken by Boian and Groh (2019) for the LBV progenitor of SN 2015bh.

CMFGEN requires the following inputs to model the spectrum arising from a dense stellar outflow: the steady stellar mass-loss rate $\dot{M}$, the bolometric luminosity $L_\star$, the stellar radius $R_\star$, the surface abundances and the wind velocity profile $v(r)$ (Eq. 2.8). When modelling CSM-interacting SNe, the mass-loss rate is that of the progenitor star which we assume expelled the CSM. Additionally, the inner boundary radius of the CSM (hereby R_{in}) is used in lieu of $R_\star$. CMFGEN does not specify the inner radiative energy source. However, we can predict that this energy originates from the efficient conversion of kinetic to radiative energy when fast-moving, recently-ejected material interacts with previously-ejected, slow-moving material. An LBV-like giant eruption occurring after a period of considerable mass loss could produce this. It could also be provided by fast-moving SN ejecta being propelled into a slow dense CSM, as described previously in Section 1.5.1. In Section 2.1, it was mentioned that our CMFGEN models assume NLTE,

radiative equilibrium and statistical equilibrium. Additionally, a β-type velocity profile is assumed for the stellar outflow or CSM. This is given by:

$$v(r) = \frac{v_0 + (v_\infty - v_0)(1 - R_*/r)^\beta}{1 + v_0/v_{\text{core}} e^{([R_* - r]/h_{\text{eff}})}}. \tag{2.8}$$

We use the following properties suitable for the velocity of the outflow of the LBV in PHL 293B: $v_0 = 10$ km s^{-1} for the velocity at a reference radius close to R_*, $v_\infty = 1000$ km s^{-1} for the terminal velocity of the wind, $v_{\text{core}} = 0.85$km s^{-1} for the velocity at R_* and $h_{\text{eff}} = 0.002\ R_*$ for the scale height and a β-parameter determining the steepness of the wind of 2.5. For the CSM velocity profile of Ibn SNe, we use $v_0 = 900$ km s^{-1}, $v_\infty = 1000$ km s^{-1}, $v_{\text{core}} = 0.02$km s^{-1} and $h_{\text{eff}} = 0.008\ R_{in}$ and $\beta = 0.2$. CMFGEN joins smoothly the density profile of the non-shocked outflow or CSM (Eq. 2.9) to a steeper profile with a scale height of h_{eff} at the very innermost region, simulating the shock layer. The density profile of sub-samples of our Type-Ibn models are shown later in Chapter 4. The assumed velocity profile $v(r)$ and mass-loss rate $\dot{M}$ combined with the mass continuity equation allows the density profile of the modelled outflow or CSM to be given as:

$$\rho_{\text{CSM}}(r) = \frac{\dot{M}}{4\pi r^2 v(r)}. \tag{2.9}$$

We also assume a spherically symmetric geometry. We further assume that the dense outflow or CSM is in a steady-state, simplifying the RT equation (Eq. 2.2) by removing the time dependent derivative $\delta I_\nu / \delta t = 0$. Gräfener and Vink (2016) warn however that light-travel-time effects may substantially effect the modelling, predicting a larger luminosity and mass loss and a lower wind velocity for SN 2013cu, compared to time-independent CMFGEN modelling by Groh (2014).

CMFGEN adopts atomic data from publicly available databases such as Opal (Iglesias and Rogers, 1996). These data includes lab-based measurements on various atomic properties such as collisional cross-sections and ionisation energies for each included species. CMFGEN groups together energetically close transitions into a single representative "super level" (Anderson, 1989), ultimately allowing for the inclusion of a large number of transitions at a reduced computational cost (Hillier and Miller, 1998). The high number of levels and transitions possible allows for accurate modelling of the line-blanketing effect in which a high number of absorption lines (usually belonging to metals) are too close together in wavelength space to be individually resolved resulting in an apparent reduction in intensity. Accurate modelling of the line-blanketing effect is

important as it can lead to back-warming as will be shown in Section 4.2. Tables 3.2 and 4.1 display the number of super- and atomic-levels used for each species included in our PHL 293B and Type-Ibn progenitor models, respectively.

2.2.1 A brief overview of the inner workings of CMFGEN

This section aims to briefly explain the complex inner workings of the CMFGEN code. It is heavily reliant on Hillier and Miller (1998), which provides considerably more in-depth explanations of CMFGEN's many procedures.

Provided with the inputs mentioned in Section 2.2, CMFGEN attempts to simultaneously solve the RT (Eq. 2.2) and SE (Eq. 2.4) equations. This is complicated by the coupling of these equations in NLTE. Therefore, CMFGEN utilises a partial linearisation technique in which the coupling only needs to be considered locally and at adjacent grid points (Hillier and Miller, 1998). The constraint equations (statistical equilibrium, charge conservation, number conservation, radiative equilibrium) can be written as:

$$S(N_e, T_e, n_{1d}, n_{2d}, ..., J_{1d}, J_{2d}...., Z_{1d}, Z_{2d}, ...) = 0, \tag{2.10}$$

in which all of the quantities are at depth d, N_e and T_e are the electron density and temperature, n_{id} is the population of level i, J_{md} is the mean intensity of the radiation field at frequency ν_m and $Z_{ld} = (1 - J_l/S_l)$ is the net radiative bracket for line l given in terms of the mean intensity in the line J_l and the line source function S_l. Linearisation of the constraint equations produces a system of equations for each depth:

$$\partial\overline{S}_d \cdot \delta\overline{N}_d = -\Delta\overline{S}_d \tag{2.11}$$

where $\partial\overline{S}$ represents the linearised constraint equations and is in the form of a $N_c \times N_T$ matrix, N_c and N_T being the numbers of constraint equations and variables, respectively. The error in the constraint equations evaluated with the current populations and radiation field is contained in the vector $\Delta\overline{S}$ while the unknown correction to the populations is contained in $\delta\overline{N}$ which is a vector of the form $(\delta N_e, \delta T_e, \delta n_{1d}, \delta n_{2d}, ..., \delta J_{1d}, \delta J_{2d}...., \delta Z_{1d}, \delta Z_{2d}, ...)$. The δJ_{md} and δZ_{ld} terms can be eliminated by replacement with δN_e, δT_e, δn_{id} using the linearised transfer equation. In performing this elimination, it is assumed that only local and adjacent coupling terms are important. This leads to a block-tridiagonal system of simultaneous equations for the corrections to the populations δn. Each block of equations is coupled over N_D depths

and has dimension $N_C \times N_C$. CMFGEN employs Fortran's LAPACK routines in order to solve these simultaneous equations. Once the corrections to δn are sufficiently small, the model is considered to have converged. CMF_FLUX (Busche and Hillier, 2005) then converts the output spectrum from the co-moving frame adopted by the modelling to the observer's frame.

2.2.2 Fitting continuum-normalised spectra

One of the benefits of CMFGEN is that it outputs separate continuum and line flux arrays. This allows for an easy comparison of line formation with an observed spectrum granted that the continuum present in the observation can be easily distinguished. If this is the case, we can manually normalise the observed spectrum with respect to its continuum. We achieve this by fitting a polynomial function to the continuum and dividing the spectrum by this function, as done previously by Boian and Groh (2020). We predict that this is accurate to within 5%, with difficulties such as galactic contamination, line-blanketing disguising continuum flux and human error in distinguishing between highly broadened emission lines and the continuum, all potentially leading to inaccuracies. Simultaneous good fits to the absolute and normalised spectra, as will be shown for SN 2010al in Figure ??, imply that both line and continuum fluxes are being reproduced accurately.

2.2.3 Accounting for the observing resolution

When comparing a modelled spectrum to an observed spectrum, it is important to account for the resolution of the observation. We do this by convolving our model spectra with a Gaussian kernel with a full width at half maximum (FWHM) corresponding to the resolution in velocity space of the observation, allowing for a more realistic comparison. The observing resolution affects the spectral line widths and strengths, and if sufficiently low, it can can hide key spectral features such as P-Cygni profiles as shown by Figure 2.1.

2.2.4 Fitting absolute flux spectra and accounting for reddening

Often a model provides a good fit to a continuum-normalised spectrum but could require a scaling of the absolute flux in order to reproduce the continuum. This could indicate an error in the assumed distance or luminosity, while the predictions for the temperature and optical depth profiles are accurate. In such a scenario, we manually scale the luminosity

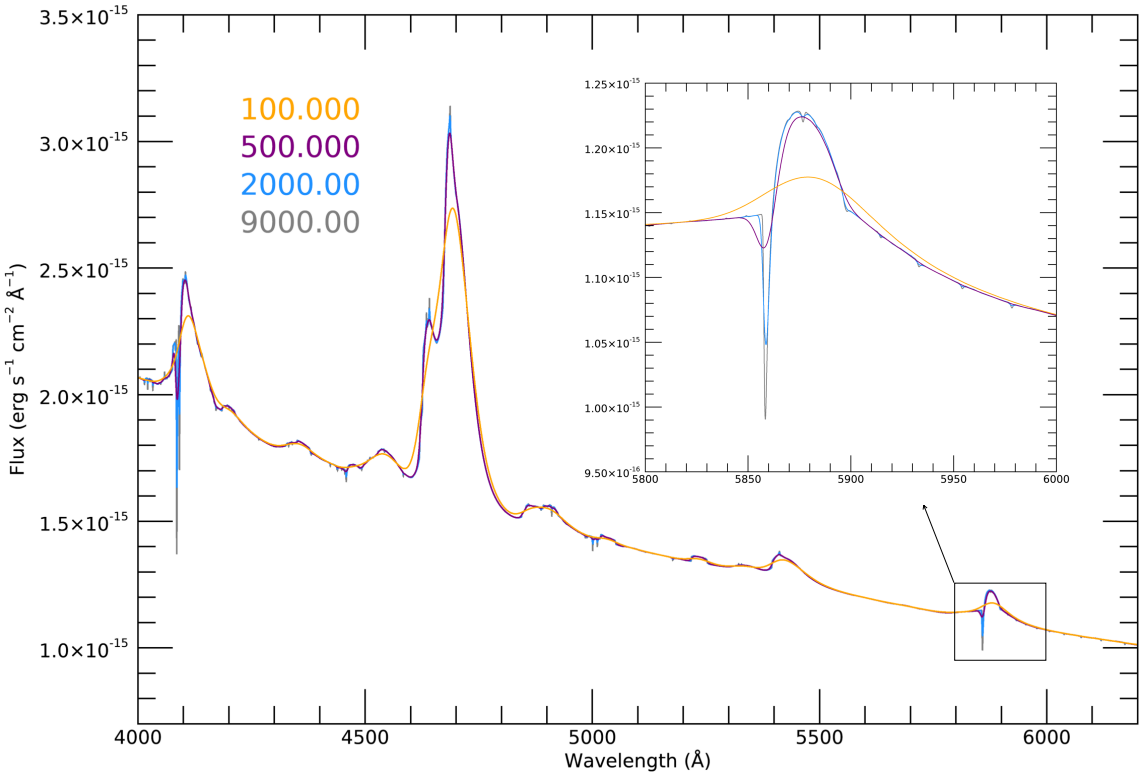

Figure 2.1: Modelled spectra of SN2010al convolved with Gaussian kernels of various resolving powers (hereby P_{res}) as indicated by colour. P_{res} is connected to the resolution $\Delta\lambda$ through the relation $P_{\text{res}} = \frac{\lambda}{\Delta\lambda}$.

as required, applying scaling relations in order to retain the temperature and optical depth profiles, consistent with Boian and Groh, 2020. In order to retain the temperature structure, the radius ($R_\star$ or R_{in}) is scaled in proportion to the square root of the luminosity in accordance with the Stefan Boltzmann Law (Eq. 2.3). A mass loss - luminosity scaling in which $\dot{M} \propto L^{0.75}$ is also used based on the scaling by Gräfener and Vink (2016). We then run a new CMFGEN model using the scaled luminosity, radius and mass-loss rate as inputs. This scaled model offers a much improved fit to the absolute spectrum, while mostly retaining the original good fit to the normalised spectrum.

We also attempt to account for the intrinsic effect of reddening in the observed spectrum, caused by the intervening interstellar medium preferentially preventing higher energy photons from reaching the observing spectrograph. For this, we use the R-dependent Galactic extinction curve of Fitzpatrick (1999) to apply artificial reddening to our models. R in this context refers to the relative visibility and is set by the ratio of total to selective extinction at V:

$$R = A(V) \ / \ E(B-V) \tag{2.12}$$

where $E(B-V)$ is the colour excess due to extinction. We assume a relative visibility of $R = 3.1$ which is its mean value for the diffuse interstellar medium (Fitzpatrick, 1999). As demonstrated in Figure 2.2, we test various colour excesses until the modelled slope of the continuum matches that of the observation.

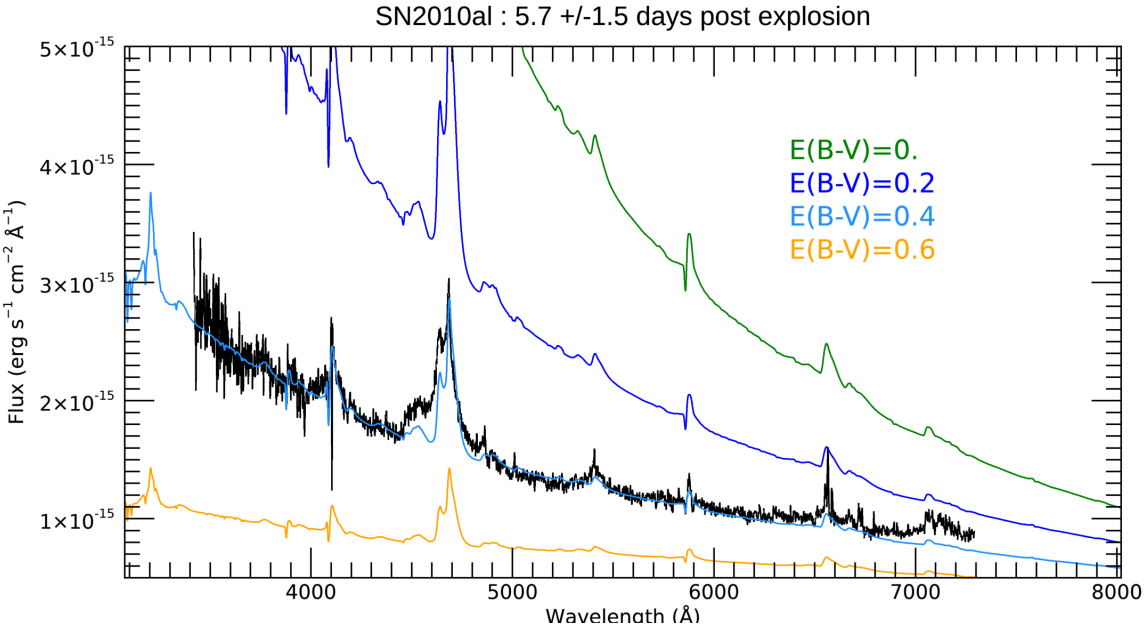

Figure 2.2: Applying different values of $E(B-V)$ (coloured spectra) to the same model spectrum in an attempt to determine the degree of reddening present in an observation of the SN-Ibn event SN2010al (black spectrum).

2.2.5 Computing synthetic photometry

Hitherto, the focus has been entirely on reproducing spectral observations of considered events to gain insight into their properties. However, these events often have a wealth of photometric observations probing wavelengths far beyond those covered spectroscopically. Photometry hence contains valuable information on the system. To avail of this, we generate synthetic photometry from our spectroscopically best-fitting models to a particular spectral observation. We can then compare this synthetic photometry to actual photometric observations of the same event. Depending on the instrument and the specific filter or band in which the photometric observation was made, there is a unique pass-band function (see top panel of Fig. 2.3) through which only a specific band

of radiation passes. Knowledge of this function combined with a relative comparison to Vega allows us to predict photometric properties such as apparent magnitudes in various filters which can be directly compared to observed light curves.

An obvious benefit of computing synthetic photometry is it can be used to study events with poor spectral coverage. This is particularly useful in our modelling of type-Ibn SNe due to the limited number of confirmed events in comparison to other SNe classifications. A good fit to photometric observations alone cannot directly tell us about the progenitor composition and mass-loss rate. However, it implies a satisfactory fit to the spectral continuum over the considered wavelength range and allows us to make predictions for the luminosity and temperature. Alternatively, if we can obtain a good spectral fit to an event in a particular wavelength region, we can then generate artificial photometry in a wavelength region in which there was only photometric coverage. Comparing the synthetic photometry with the observation in this additional wavelength region allows for a deeper analysis, ultimately strengthening or discrediting the predicted properties obtained with the spectral fit alone.

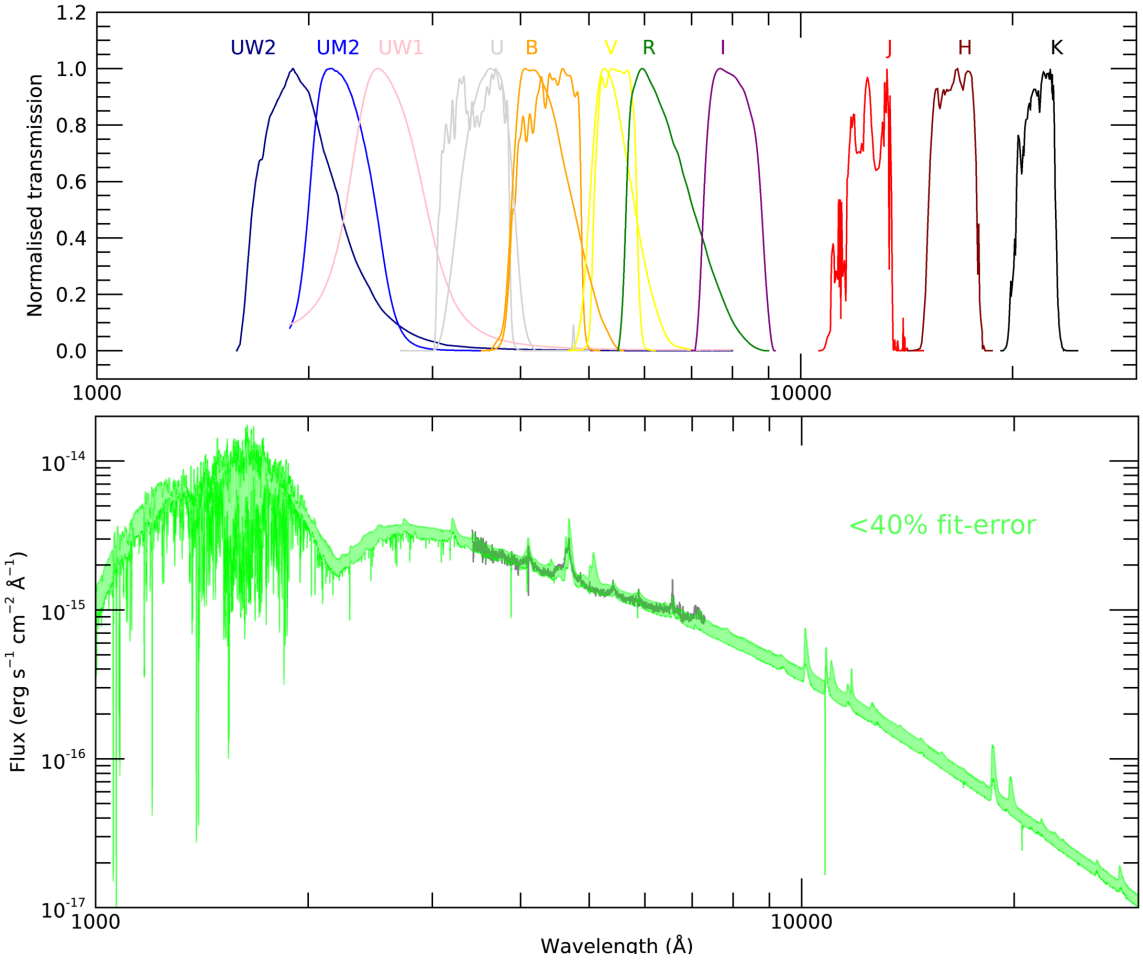

Figure 2.3: Upper panel: pass-band functions corresponding to the photometric observations of SN 2010al shown later in Figure ??. The UW2, UM2, UW1 as well as the more jagged of the U, B and V profiles belong to the Swift UltraViolet and Optical Telescope (hereby UVOT). Lower panel: Optical spectrum of SN2010al taken 5.7 days post-explosion (grey) compared to our models which achieve a fit error <40% (green) which are described in Section 4.3.

Chapter 3

The possible disappearance of a massive star in the low-metallicity galaxy PHL 293B

This chapter is based on 'The possible disappearance of a massive star in the low-metallicity galaxy PHL 293B' (Allan et al., 2020), which was accepted in The Monthly Notices of the Royal Astronomical Society in June 2020. The co-Authors of this work are José H. Groh, Andrea Mehner, Nathan Smith, Ioana Boian, Eoin J. Farrell and Jennifer E. Andrews. Previous spectral studies of PHL 293B, first introduced in Section 1.6, have inferred the presence of an LBV star in outburst. This chapter begins with Section 3.1 discussing our two spectral observations of PHL 293B, in addition to previously unpublished Hubble Space Telescope imaging. Section 3.2 exhibits the surprising absence of the LBV signatures in these two latest spectra. Section 3.3 describes the specifics of our spectral models for PHL 293B and the properties which they predict. Our photometric analysis of PHL 293B is discussed in Section 3.4. Finally, in Section 3.5, three potential hypotheses for the disappearance of the LBV spectral signatures are explored.

3.1 New spectral observations and unpublished HST imaging

We obtained two new spectra of PHL 293B in 2019, the first of which was obtained on August 28 using the Echelle SPectrograph for Rocky Exoplanets and Stable Spectroscopic Observations (hereby ESPRESSO, Pepe et al., 2021) of the European Southern Observatory's Very Large Telescope (hereby VLT) in Chile's Atacama Desert. ESPRESSO was used in the four-unit telescope mode, combining the light from four 8 m

telescopes. The data was reduced with the ESO pipeline version espdr/1.3.0. As will be explained more in Section 3.2, this observation excitingly suggested the disappearance of a spectral signature previously believed to originate from the outflow of a massive LBV star. As a result of this, we were fortunate to secure a follow-up spectrum with the X-shooter spectrograph (Vernet et al., 2011) on December 17, 2019, obtained through a director's discretionary time (DDT) proposal (2104.D-5015A; PI Allan). The X-shooter data was reduced with the ESO pipeline version xshoo/3.3.5.

We also obtained an archival image of PHL 293B taken with the Hubble Space Telescope (hereby *HST*) on October 31, 2010 (GO-12018; PI Prestwich). This observation was made using HST's wide-field camera 3, in the filters F336W, F438W, F606W, and F814W. With this observation, we performed photometry of the brightest region of the galaxy, where the LBV was believed to reside, being where the previous spectroscopic observations centred their slit. In doing this, we used Dolphot (Dolphin, 2000; Dolphin, 2016) on the standard STScI pipeline pre-processed, charge-transfer efficiency corrected images. These photometric observations were obtained before the LBV signature disappeared, and give the following apparent magnitudes: $m_{\mathrm{F336W,pre}} = 19.70 \pm 0.01$, $m_{\mathrm{F438W,pre}} = 20.82 \pm 0.01$, $m_{\mathrm{F606W,pre}} = 20.31 \pm 0.01$, and $m_{\mathrm{F814W,pre}} = 20.03 \pm 0.01$ mag in the F336W, F438W, F606W, and F814W filters, respectively.

3.2 The disappearance of the stellar signature

Section 1.6 mentioned that the presence of a massive LBV star in the galaxy PHL 293B was inferred from spectral observations of the galaxy taken between 2001 and 2011 (Izotov and Thuan, 2009; Izotov et al., 2011). Consistently strong, broad emission components in the H Balmer lines were inferred to originate from the outflow of the LBV. This is strengthened by the presence of Fe II and weak He I lines unique to LBVs (Groh et al., 2014).

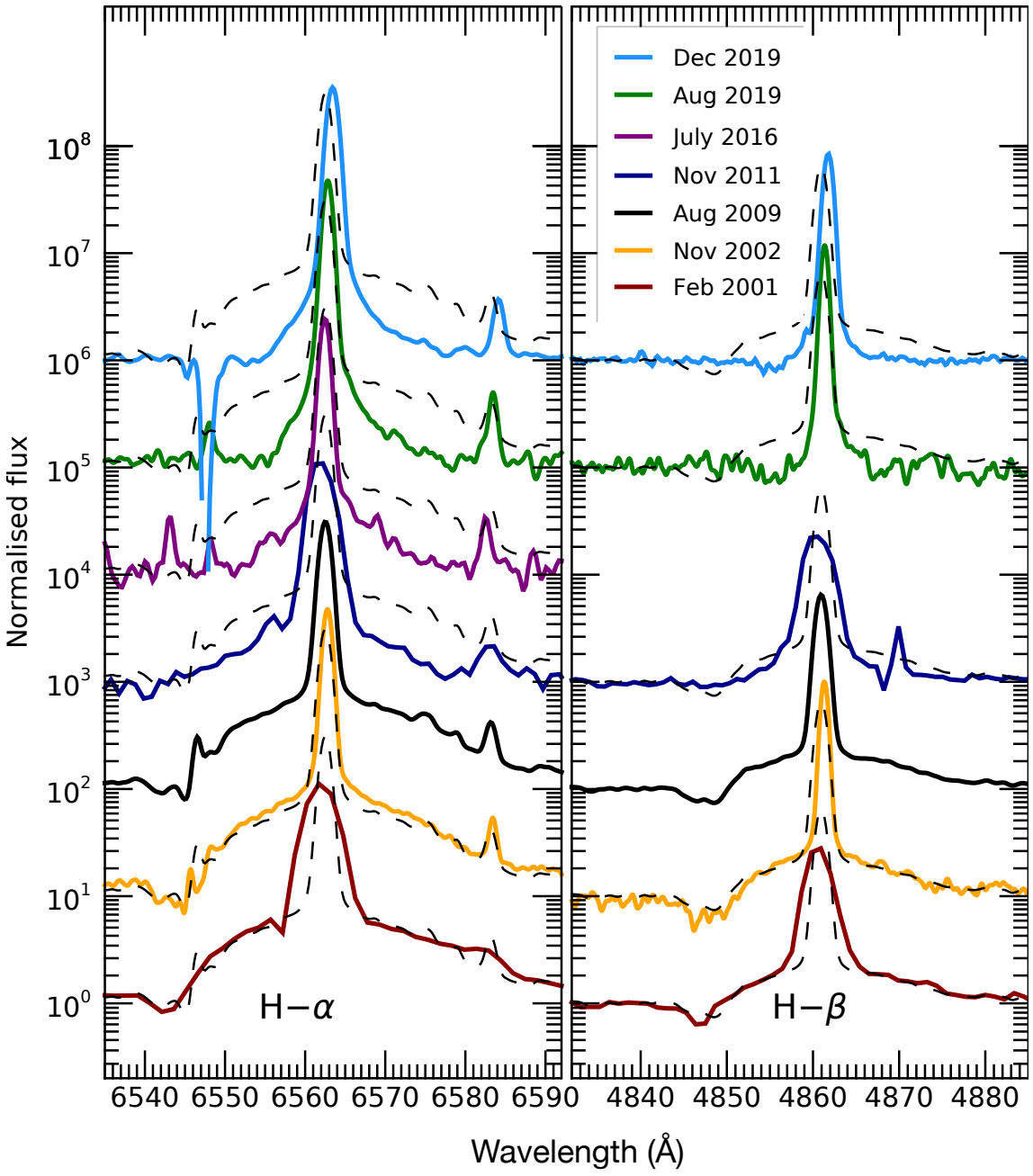

Figure 3.1: Spectroscopic evolution of PHL 293B between 2001 (lowest spectrum) and 2019 (highest). The 2009 X-shooter spectrum (dashed grey) is over-plotted to all spectra, which are also shifted for clarity. Table 3.1 summarises the observing setup used in obtaining each of the included observations.

Table 3.1: Observing set-up for spectral observations of PHL 293B from 2001 to 2019.

Instrument	Date	Wavelength (Å)	Setup	Resolving power
VLT/X-shooter	2019-12-17	3000–23000	UVB, VIS, NIR (1.0'', 0.9'', 0.9'')	5400, 8900, 5600
VLT/ESPRESSO	2019-08-28	3800–7800	MR42 (4x1'')	72 000
HST/COS	2018-04-30	1027–2337	G140L (2.5'')	2000
INT/IDS	2016-07-02	5890–7230	H1800V (1'')	7000
WHT/ISIS	2011-11-30	3805–8095	R300B/7500 (1'')	1000
WHT/ISIS	2011-09-24	2630–6230	R300B/5700 (1'')	1000
VLT/X-shooter	2009-09-28	3000–23000	UVB, VIS, NIR (1.0'', 0.9'', 0.9'')	5100, 8800, 5600
VLT/X-shooter	2009-08-16	3000–23000	UVB, VIS, NIR (1.0'', 0.9'', 0.9'')	5100, 8800, 5600
VLT/UVES	2002-11-08	3100–6800	DICHR#1 (1'')	40 000
SDSS	2001-02-22	3810–9200	3'' fiber	2000

The original aim of our ESPRESSO observation was simply to obtain a high resolution spectrum which we could apply our models to in order to constrain the properties of the LBV. Figure 3.1 however reveals that this spectrum, as well as our follow-up X-shooter spectrum, exhibit important variations from all prior spectra of PHL 293B, namely the absence of the LBV signatures. The broad wings of the H-α and H-β emission lines are significantly reduced in these later spectra. It is also apparent that the signatures were in fact absent from an earlier archival observation obtained using the Intermediate Dispersion Spectrograph on the Isaac Newton Telescope (Smith and Dudley, 1982) in 2016. In addition, Fe II and weak He I lines believed to originate from the LBV are also absent in these more recent observations. Table 3.1 gives the observing set-up for each of the spectral observations. We interpret the initial lack of spectral variability shown in Figure 3.1 as evidence for the LBVs presence between 2001 and 2011, in agreement with Izotov and Thuan (2009) and Izotov et al. (2011). The LBV signature then disappeared sometime between 2011 and 2016. A number of scenarios could result in this disappearance, as Section 3.5 will explore.

3.3 Spectral modelling with CMFGEN

In order to constrain the properties of the LBV in PHL 293B, we compute new radiative transfer models using CMFGEN, described previously in Section 2.2. We fit these models to the high-resolution 2002 spectrum (presented in Izotov and Thuan, 2009) obtained with the Ultraviolet and Visual Echelle Spectrograph (hereby UVES, Dekker et al., 2000) instrument of the VLT. The models make similar physical assumptions to those of the LBV progenitor of the SN candidate SN 2015bh (Boian and Groh, 2018). Each of the CMFGEN models in our library has a differing combination of $\dot{M}$ and L. We also test variations in the stellar radius, finding however that this only has a minor effect on the key spectral features, as will be discussed. Table 3.2 displays the atomic model used in our modelling of the LBV. We assume an Fe mass fraction of 1.7 $\times 10^{-4}$, ~ 0.1 of the solar value, as expected for PHL 293B. We also assume a He mass fraction of 0.5 (~ 1.8 of the solar value), which is typical of LBVs (Groh et al., 2009). Since only a handful of diagnostic lines are present, both the He and Fe abundances are assumed rather than derived values. In this temperature regime, the He and Fe lines are affected by a small change in stellar or wind parameters (Boian and Groh, 2018). This is especially relevant for Fe, since we assume a solar-scaled Fe/O ratio, and this may not hold depending on the chemical evolution history of the galaxy. Since the derived metallicity of PHL 293B is

based on nebular O lines (Izotov and Thuan, 2009), a change in Fe abundance by a factor of 2, for instance, would still be consistent with our models. For simplicity our models are unclumped, and indeed they match the strength of the observed electron-scattering wings of the H lines, which is a key clumping diagnostic (Hillier, 1991). We degraded the CMFGEN high-resolution synthetic spectra by convolving with a Gaussian kernel of 33.3 km s^{-1} (resolving power $P_{\rm res}$ ~9000) as to match the UVES spectral resolution (see Sec. 2.2.3). Because of the high wind density, we compute both a flux temperature $T_\star$ at a large optical depth ($\tau_{\rm Ross}$=10), as well $T_{\rm eff}$ at the photosphere (where $\tau_{\rm Ross}$=2/3).

Due to its distance of 23.1 Mpc, the LBV is spatially unresolved from the underlying stellar population of PHL 293B in seeing-limited ground-based data. Therefore, we add an additional parameter to the outputted total flux of the models, a flat background galaxy component. We vary this parameter for each LBV model in our library, noting the stellar and galactic contribution parameters necessary to simultaneously achieve a good fit to both the continuum and key spectral lines. To do so, we match simultaneously the continuum and H-α, H-β, and Fe II 5169 Å lines. A simultaneous match is needed because all the diagnostics above depend on multiple model parameters, such as the luminosity, mass-loss rate, and effective temperature. For fitting the absolute level of the continuum, we use a conservative criterion and compare the mean absolute flux of our models in the region 6470 – 6520 Å to the observations, and only retain models that are within ±5% of the observed value. We then compare the equivalent width of the H-α, H-β, and Fe II 5169 Å emission lines to the 2002 observation, giving equal weights to each line when computing the fit error. We chose these lines as they are the only ones where the broad component is visible with a sufficiently high signal-to-noise ratio. The white regions in Figure 3.2 show the wavelength range considered in this calculation for the H-α, H-β (upper panels) and Fe II 5169 Å lines (lower left panel). We neglect the narrow component of the Balmer lines as this is strongly affected by the background galaxy and likely originates from a region of H II ionised by many O-type stars (Izotov et al., 2011). We define our best-fit models as those which produce a fit error of $< 25\%$. The range of input parameters and background galaxy contributions of these best-fit models allow us to estimate the properties of the LBV.

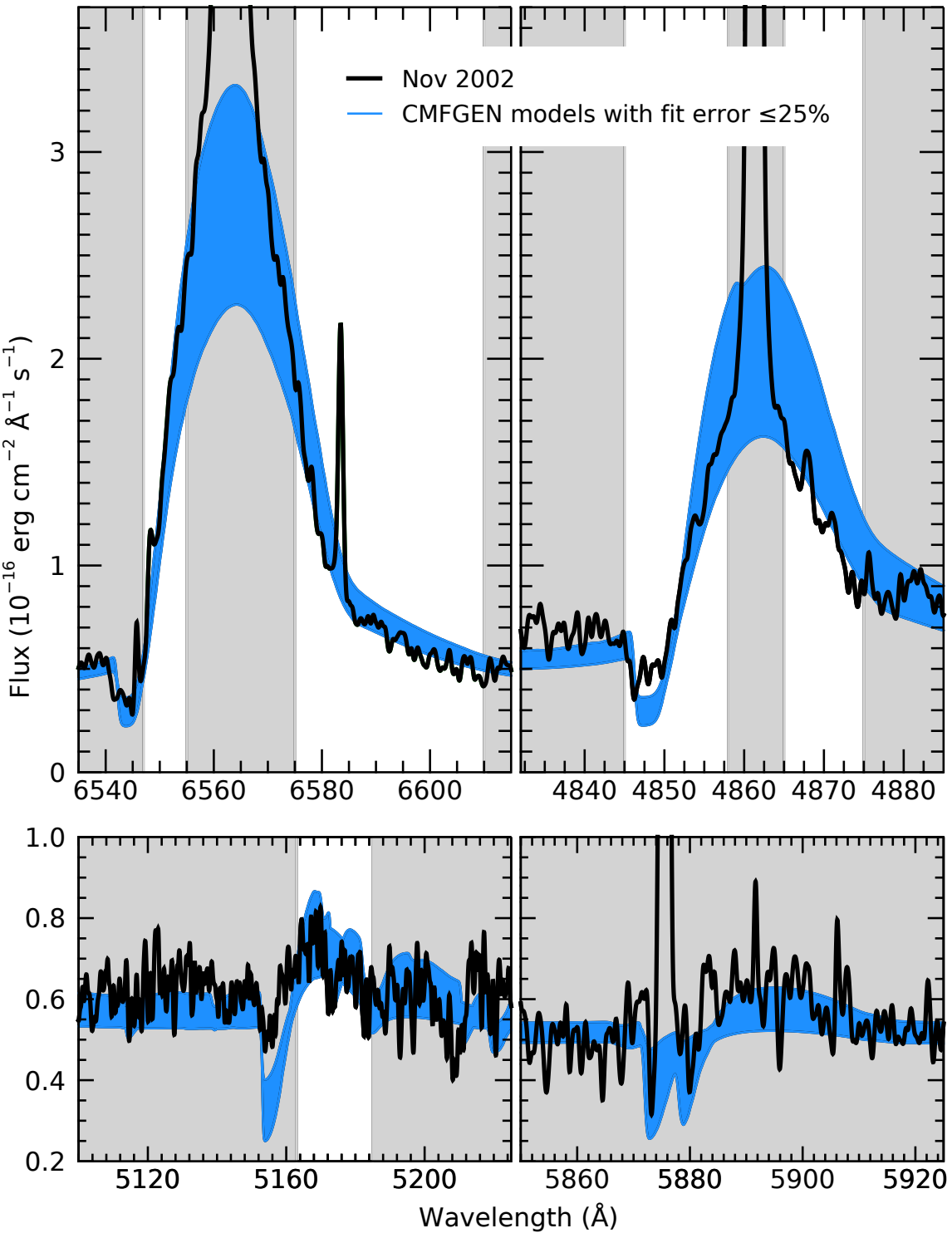

Figure 3.2: Comparison of the 2002 UVES spectrum of PHL 293B (black) to our best-fitting CMFGEN models. Blue region corresponds to models with a fit error $\leq$ 25%. White regions show the wavelength ranges considered in the fit. The upper left and right panels display the H-α and H-β emission lines respectively. The lower left panel includes the tested Fe II 5169 Å emission line in addition to weaker Fe II 5159 Å and N I 5198 Å emission and Fe III 5156 Å absorption. Some best-fit models also feature weak Mg I 5173 Å and 5184 Å and Tk II 5186 Å and 5189 Å. The lower right panel includes the He I 5786 Å line as well as Na I 5890 Å and 5896 Å emission.

Table 3.2: CMFGEN atomic model used in our analysis of PHL 293B.

Species	No. of super-levels	No. of atomic levels
H I	20	30
He I	40	45
He II	22	30
C I	38	80
C II	39	88
C III	32	59
N I	44	104
N II	157	442
N III	42	158
O I	69	161
O II	26	80
O III	33	92
Na I	18	44
Mg I	37	57
Mg II	18	45
Al II	38	58
Al III	17	45
Si II	22	43
Si III	20	34
Si IV	22	33
Ca I	23	39
Ca II	17	46
Ti II	33	314
Ti III	33	380
Fe I	69	214
Fe II	67	403
Fe III	48	346
Ni II	29	204
Ni III	28	220

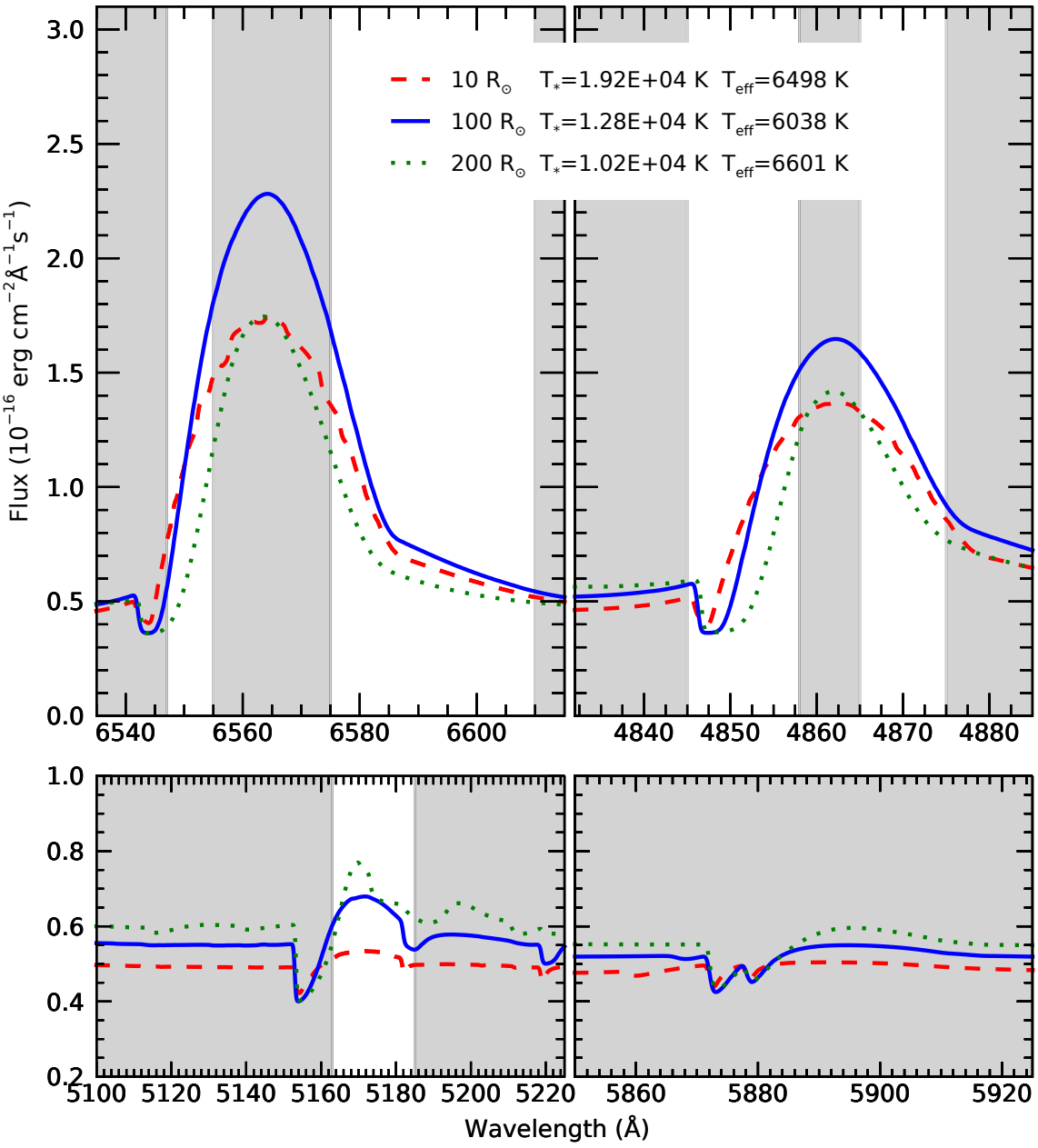

Figure 3.3: CMFGEN radiative transfer models for different stellar radii. The solid-blue spectrum belongs to one of our best-fit models with the following parameters: $R_\star$=100$R_\odot$, $L_* = 2.52\times10^6\ L_\odot$ and $\dot{M} = 0.008\ M_\odot\ \mathrm{yr}^{-1}$. We compare this to two otherwise identical models but with $R_\star = 10\ R_\odot$ (dashed red line) and $R_\star = 200\ R_\odot$ (dotted green line).

3.3.1 Inferred properties of the missing star

Our best-fitting CMFGEN models to 2002 UVES spectrum encompass the blue region of Figure 3.2, providing good fits to the inferred LBV signatures, producing similar P-Cygni emission and absorption components. Their ranging inputs indicate that before its disappearance, the LBV had $L_* = 2.5 - 3.5 \times 10^6\ L_\odot$, $\dot{M} = 0.005 - 0.020\ M_\odot\ \mathrm{yr}^{-1}$, an effective temperature $T_{\mathrm{eff}} = 6000 - 6800$ K, and $T_* = 9500 - 15000$ K. While models with $L_* = 3.5 - 5.0 \times 10^6\ L_\odot$ are consistent with the ground-based data (Fig. 3.4), they are too bright compared to the *HST* observations, as will be discussed in Section 3.4. A stellar wind velocity of 1000 km s^{-1} is required by our models to reproduce the broad emission and P-Cygni absorption component of the H and Fe lines. This velocity is much faster than the 40 km s^{-1} outflow observed for the extreme Red Supergiant (RSG) VY CMa (Smith, Hinkle, and Ryde, 2009) or the typical velocities of $50 - 300$ km s^{-1} observed in S Doradus outbursts of LBVs (van Genderen, 2001). The predicted properties strongly suggest that the LBV was in an eruptive state. Based on our best-fit models, we estimate that the LBV contributes $20 - 47\%$ of the total flux collected in the 1" aperture used in the ground-based spectroscopic observations, with the rest coming from the underlying stellar population. It is important to note that the contribution of the LBV to the total flux would be much smaller for larger apertures, for example those used in the ground-based photometry presented in Burke et al. (2020).

Our best-fit models for the 2002–2011 spectra place the LBV in PHL 293B at the higher luminosity end of the HR diagram (Fig. 3.5), in proximity to very massive LBVs such as η-Carinae, and in a temperature range characteristic of LBVs. It should be noted that the wind properties are stronger than those of η-Carinae, with $\dot{M}_*$ being 5–20 times larger for PHL 293B. It is, however, remarkably similar to the quiescent LBV progenitor of SN 2015bh, in L, T, $\dot{M}_*$, and v_∞, with SN 2015bh being only slightly hotter (Fig. 3.5). SN 2015bh (Boian and Groh, 2018) is a SN candidate with a rare pre-explosion spectrum. SN 2009ip (Smith et al., 2010; Foley et al., 2011) is part of the same category of events, and its progenitor also resides in a similar region of the HR diagram, however, slightly dimmer than PHL 293B, and with relatively poor $T_\star$ constraints. Other LBV progenitors of luminous transients, such as SN 2010jl (Stoll et al., 2011) and Gaia16cfr (Kilpatrick et al., 2018), which have been identified in pre-explosion photometry, show much lower luminosities but consistent temperatures. An obvious difference between all mentioned transients and the PHL 293B case is the detection of a SN explosion rather than simply the fading of the star.

As the outflow of the LBV is very dense, its hydrostatic radius $R_\star$ is difficult to

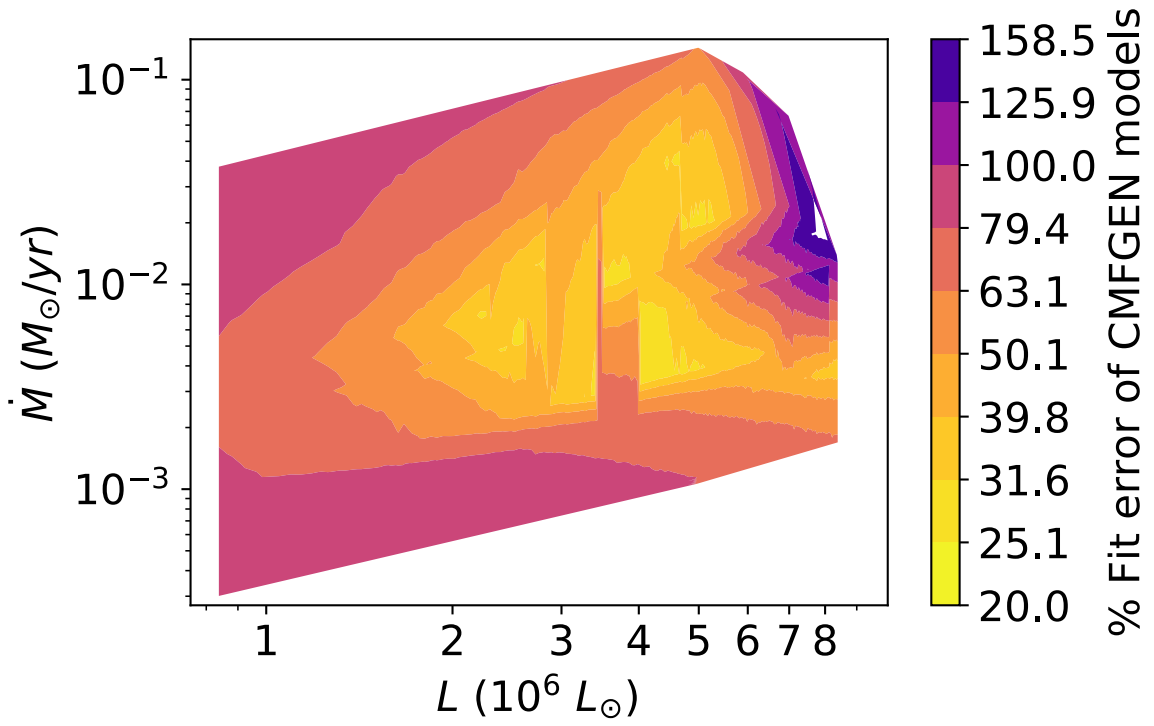

Figure 3.4: Grid of best-fitting CMFGEN models of varying mass-loss rates and luminosities to the 2002 UVES spectrum of PHL 293B. The colour denotes the calculated fit-error of the models.

constrain. Figure 3.3 shows that over a large range of radii, the spectral morphology shows little variation. This is similar to what has been found for η-Carinae, which also possesses a high-density wind (Hillier et al., 2001; Hillier et al., 2006; Groh et al., 2012b). Hillier et al. (2001) find that the dense wind of η-Carinae prevents the temperature of the underlying star from being well determined. Minor variations in line strength due to largely differing choices of hydrostatic radius and consequently temperature could instead be caused by a relatively small change (30-50%) in the mass-loss rate or luminosity. A different He fraction could also alter emission line strengths in this manner. In the case of PHL 293B, large changes from our reference value of 100 $R_\odot$ would require greater mass-loss rates to fit the observations, as shown by Figure 3.3. In this sense, our quoted values of $\dot{M}$ are lower limits. We also omit the narrow region of the Balmer lines in our analysis due to its galactic origin in the observations. This further softens the importance of the chosen radius as the majority of variation resulting from changing the radius is within this component. In summary, our conclusion that the LBV possessed an extremely dense wind is not affected by the choice of $R_\star$.

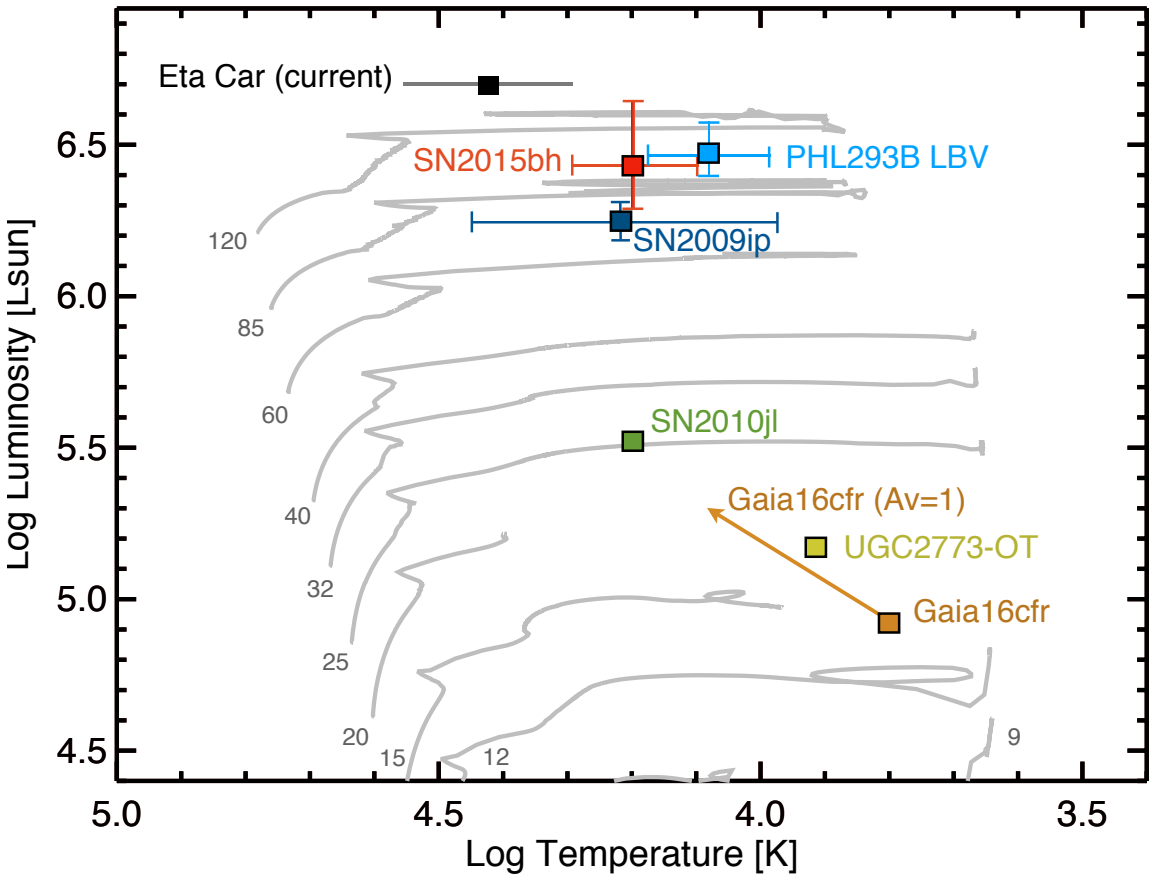

Figure 3.5: HR diagram showing the location of the LBV in PHL 293B during 2002–2011. We also include η-Carinae (Groh et al., 2012a) and the progenitors of SN 2015bh (Boian and Groh, 2018), SN 2009ip (Smith et al., 2010; Foley et al., 2011), UGC2773-OT (Smith et al., 2010), SN 2010jl (Smith et al., 2011a), and Gaia16cfr (Kilpatrick et al., 2018). Evolutionary tracks for rotating stars with initial masses in the range $9 - 120\ M_\odot$ at $Z = 0.0004$ (Groh et al., 2019) are shown in grey.

We also investigate the maximum values of the luminosity ($L_{\rm surv}$) and mass-loss rate ($\dot{M}_{\rm surv}$) that a surviving star concealed within the noise of our 2019 X-shooter spectrum could have. Assuming no dust formation and no change in temperature, we find $L_{\rm surv} = 3.8 \times 10^5\ L_\odot$ and $\dot{M}_{\rm surv} = 2.8 \times 10^{-3}\ M_\odot\ {\rm yr}^{-1}$ (Fig. 3.6). This would require minimum reductions in L_* and $\dot{M}$ of 85–92% and 44–86%, respectively. However, the underlying star could be much more luminous when taking circumstellar dust into account. With the end of the eruption, the star could have become hotter and with a lower mass-loss rate. In this case, the upper limit on $L_{\rm surv}$ would be higher than that quoted here.

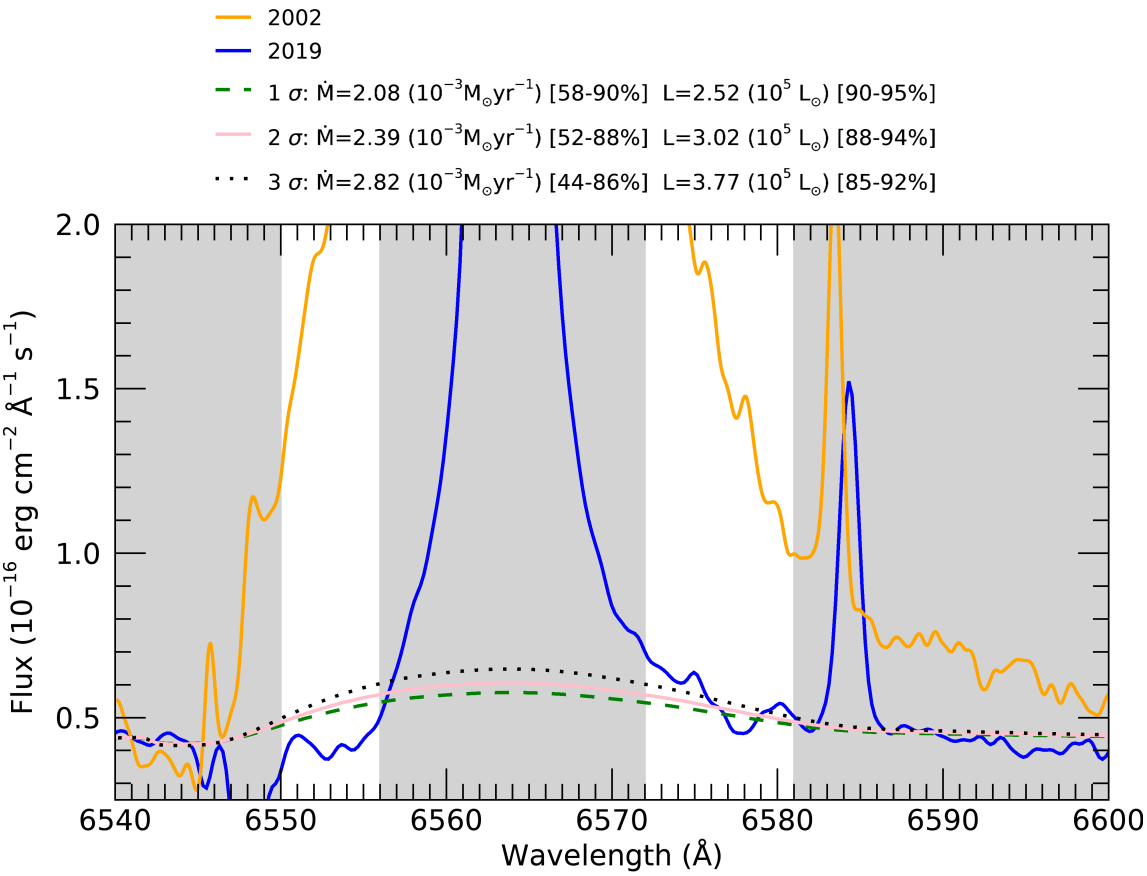

Figure 3.6: CMFGEN models compared to the 2019 X-shooter spectrum (blue). The models correspond to upper limits of L_{surv} and $\dot{M}_{\mathrm{surv}}$ with 1 (dashed green), 2 (solid pink), 3 (dotted black) σ confidence. The 2002 UVES spectrum (yellow) is included to highlight the significant reduction in the broad H-α emission.

3.4 Photometric analysis

Section 3.1 explained that we obtained an archival *HST* observation of PHL 293B taken before the spectral disappearance, on which we performed photometric analysis, obtaining apparent magnitudes in each of the observing filters. In addition to this photometry, we compare our models to observations obtained with SDSS and DES, presented in Burke et al. (2020). Using our procedure for computing synthetic photometry from our best-fit spectral models described in Section 2.2.5, we now investigate the photometric changes that would be expected in the scenario of a disappearing star. We find that our LBV models have apparent magnitudes of $m_{\mathrm{LBV,g}} = 20.20 - 21.05$ mag and $m_{\mathrm{LBV,r}} = 19.79 - 20.56$ mag in the SDSS g and r filters, respectively. In the *HST* F336W, F438W, F606W, and F814W filters, we obtain $m_{\mathrm{LBV,F336W}} = 19.52 - 20.20$ mag, $m_{\mathrm{LBV,F438W}} = 20.27 - 21.13$ mag, $m_{\mathrm{LBV,F606W}} = 19.92 - 20.72$ mag, and $m_{\mathrm{LBV,F814W}} = 19.79 - 20.72$ mag.

We determine the following relation for the expected change in apparent magnitude taken pre- and post-LBV disappearance:

$$\Delta m = m_{\mathrm{post}} - m_{\mathrm{pre}} = -2.5 \log \left(1 - 10^{\frac{m_{\mathrm{pre}} - m_{\mathrm{LBV}}}{2.5}}\right), \tag{3.1}$$

where m_{pre} and m_{post} are the apparent magnitudes of the galaxy captured within a given filter before and after the LBV disappeared, respectively, and m_{LBV} is the apparent magnitude of the LBV alone.

We use the photometry from Burke et al. (2020) to estimate m_{pre} in the SDSS g and r bands. We interpolate the SDSS 2005 and 2013 observations and find $m_{\mathrm{pre,g}} \simeq m_{\mathrm{pre,r}} \simeq 17.83$ mag. Using Equation 3.1, we obtain Δm of about $0.06 - 0.13$ mag and $0.09 - 0.19$ mag in the g and r bands, respectively, if the LBV was to completely disappear. These variations are broadly consistent with the light curve of Burke et al. (2020). This SDSS and DES ground-based photometry uses a large aperture of 5" diameter, hence a large fraction of the underlying galaxy flux is included in the aperture (see Fig. 1 of Burke et al., 2020). The galactic component also captured within the aperture will have the effect of diluting the variation in the measured apparent magnitude if the LBV was to disappear.

Figure 3.7 shows a high spatial resolution image of PHL 293B obtained with *HST* (left panel) compared to an SDSS image of lower spatial resolution (right panel). Because of the high spatial resolution of the *HST* observations, we were able to extract photometry using a much smaller aperture than those of SDSS and DES. For that reason, the LBV contributes to a much higher fraction of the flux in the *HST* observations. Some of our

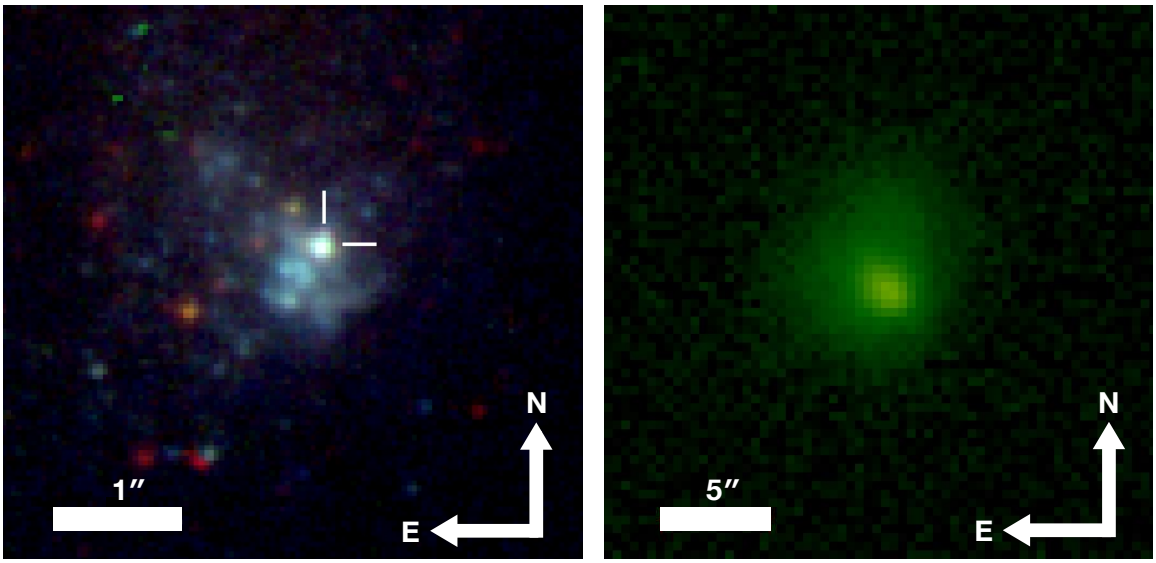

Figure 3.7: Left: High-spatial resolution colour-composite image of PHL obtained with *HST* WFC3 on 2010-10-31 (GO-12018; PI Prestwich). Right: SDSS *g*-band image of PHL 293B taken on 2003-10-24. The spatial scales are indicated by the horizontal bar.

best-fitting CMFGEN models are consistent with the magnitude and colours observed with *HST*, implying that the object for which we extracted 2010 *HST* photometry may actually be the LBV itself. Fainter LBV models are also consistent with the data. Because of the smaller aperture, if the LBV disappeared we predict much higher magnitude changes in future *HST* data, even for the faint models. We find lower limits for the Δm in each filter, obtaining $\Delta m_{\mathrm{F336W}} = 1.07$, $\Delta m_{\mathrm{F438W}} = 1.54$, $\Delta m_{\mathrm{F606W}} = 1.26$, $\Delta m_{\mathrm{F814W}} = 0.81$ mags. High resolution spatial observations are therefore warranted to constrain the photometric variability of the LBV and potentially verify its complete disappearance.

3.5 The fate of the missing star

We infer that PHL 293B hosted an LBV undergoing an eruption that ended sometime between 2011 and 2016. We now explore three potential scenarios which could explain the disappearance of the LBV signature.

3.5.1 A dust obscured surviving star

One possibility is that we are seeing the end of an LBV eruption of a surviving star, with a mild drop in luminosity, a shift to higher effective temperatures, and some dust

obscuration. The lack of variation in the broad emission of H-α and H-β lines in all spectra from 2001 to 2011 would require such an eruption to have persisted for a minimum of 8.5 years. Considering the high mass-loss rate and relatively low temperatures for the outer wind from our model predictions, the dust obscuration scenario does not necessarily require a sudden end of the eruption between the 2011 and 2016 observations. A combination of a slightly reduced luminosity and a thick dusty shell could result in the star being obscured. While the lack of variability between the 2009 and 2019 near-infrared continuum from the two X-shooter spectra eliminates the possibility of formation of hot dust ($\gtrapprox$ 1500 K), mid-infrared observations are necessary to rule out a slowly expanding cooler dust shell.

Smith and Owocki (2006) show that optically thick, continuum-driven outbursts could play a greater role in the mass loss of massive stars than steady, line-driven winds. Importantly, they suggest that such outbursts should be largely metallicity insensitive in comparison to line-driven winds. Our potential finding of such an outburst at a low metallicity could help confirm their hypothesis, implying that mass loss at low metallicities could be dominated by continuum-driven outbursts. This conclusion would carry important implications for stellar mass loss in the early Universe.

3.5.2 Direct collapse to a black hole

Instead of surviving the eruption, the LBV in PHL 293B could have collapsed to a BH, with perhaps the LBV eruption signalling the end of the stellar life. Assuming that a BH has been formed, we utilise low initial metallicity (Z=0.002 and Z=0.0004) stellar evolutionary models (Georgy et al., 2013; Groh et al., 2019) to estimate the BH mass. We find that an initial mass between 85–120 $M_{\odot}$ best suits our determined parameters for the LBV, assuming a single star evolution. Based on this initial mass range, a BH could acquire a mass of between 40 and 90 $M_{\odot}$ through fallback, assuming no mass loss at that stage. The final BH mass depends on the rotation of the progenitor. Fast-rotating models within this initial mass range may produce a pair-instability SN rather than a core collapse to a BH. The non-detection of such a bright event, however, suggests that this was unlikely to be the case for the LBV in PHL 293B. Evolutionary models predict that the lifetime of a star with initial mass of 120 $M_{\odot}$ is between 2.88 − 3.90 Myr, depending on the metallicity and rotation (Georgy et al., 2013; Groh et al., 2019). The initial mass of the star could, however, have been significantly lower if the star was a mass gainer in a binary system. This would result in a drastically longer lifetime and lower BH mass. Determining

the age of the stellar population surrounding the LBV could possibly discriminate between single and binary star evolutionary scenarios, see Smith and Tombleson (2015).

A spectroscopic observation of a star immediately preceding the collapse to a BH without a bright SN would be unprecedented. LBVs span a wide range of luminosities (Smith et al., 2019) and it would not be impossible for a low-luminosity, dust-reddened LBV to show eruptive behaviour and perhaps collapse to a BH. This could have important consequences for N6946-BH1 (Adams et al., 2017a) and the other failed-SNe candidates discussed in Section 1.5.4.

3.5.3 An undetected supernova

An alternative explanation for the disappearance for the LBV in PHL 293B is an undetected SN explosion. Burke et al. (2020) favour this hypothesis, suggesting that an SN IIn event occurred between 1995 and 1998, during which no photometry is available. In this case, the broad components seen in the Balmer lines between 2001–2011 would instead come from interaction between the SN ejecta and a dense circumstellar medium. This scenario requires that a potentially prolonged SN interaction went undetected at early-times, and our data cannot rule this out.

Both pre- and post-explosion spectra have been reported for only one SN (SN 1987a; Walborn et al., 1989) and two SN candidates (SN 2009ip, e.g. Smith et al., 2010; Smith, Mauerhan, and Prieto, 2014); and (SN 2015bh, e.g. Thöne et al., 2017; Boian and Groh, 2018). Analysis of the pre-explosion spectra has revealed that the progenitor of SN 2015bh was an LBV star (Boian and Groh, 2018). Interestingly, the spectra and consequently the predicted parameters of its progenitor do not greatly differ from that of the LBV in PHL 293B.

Chapter 4

Using CMFGEN to investigate the properties of SN Ibn

The following chapter is based on 'Type-Ibn Supernovae - A detailed spectroscopic study using radiative transfer modelling with CMFGEN' (Allan and Groh, 2021, in preparation for submission). Section 4.1 begins by outlining the specific modelling techniques used to study the spectra of Ibn, including our automated routine for quickly fitting their normalised, early-time optical spectra. Section 4.2 explores the spectral dependencies on key parameters. This chapter culminates in Section 4.3, in which we apply our techniques specifically to one of the earliest spectroscopically observed Type-Ibn SNe SN 2010al, in order to predict its properties.

4.1 Predicting the properties of Ibn SNe progenitors

To model the spectrum produced in the interaction of SN ejecta with a dense H-free CSM, we use the publicly available radiative-transfer code CMFGEN (Hillier and Miller, 1998) described previously in Chapter 2. Once accepted, our library of models will be made readily available online. It is our understanding that this will be the first study which utilises detailed radiative transfer calculations for spectroscopic modelling of Type-Ibn events. Boian and Groh (2020) present a similar study of early-time spectra for the CSM-interacting, H-rich Type-IIn classification of SNe, also using CMFGEN.

For consistency with our models, an observed spectrum must have been obtained <15 days after explosion. This is for a number of reasons. At earlier times, the CSM is more representative of the progenitor star. With time, the properties of the CSM can vary greatly as a result of the shock travelling through it. The assumption of a stationary CSM holds well at early-times given that the CSM has a negligible velocity (10-1000 km s^{-1})

compared to the much faster ejecta (10^4 km s^{-1}). The SN luminosity may also accelerate the CSM, making predicting the progenitor wind velocity in the case that the CSM was formed by a steady line-driven wind less accurate. Gräfener and Vink (2016) compute the radiative acceleration due to the SN explosion of SN 2013cu, finding a substantial increase in velocity near R_{in}, declining to a negligible acceleration at greater depths. They also consider ion decoupling, in which a greater number of absorbing spectral lines of more complex ions results in these ions experiencing a stronger radiative acceleration than those of H and He. For this to occur, the radiative acceleration must be sufficient to overcome Coulomb coupling. They point out however, that ion decoupling would not be expected for SN 2013cu, according to the following condition from Lamers and Cassinelli (1999) for the efficiency of Coulomb coupling:

$$\frac{L_{SN}(L_{\odot})v(km/s)}{\dot{M}(M_{\odot}\mathrm{yr}^{-1})} \lesssim 5.9 \times 10^{16} \tag{4.1}$$

The predicted properties of SN 2013cu by Gräfener and Vink (2016) return a value of 1.5 $\times 10^{14}$ for the left-hand side of Equation 4.1, suggesting that ion-decoupling does not occur. Interestingly, our predicted properties for SN 2010al (which will be presented in Section 4.3) return a similar value ranging from 1 $\times 10^{14}$ to 3 $\times 10^{14}$. Another important effect which is not currently accounted for in our models is light-travel time (hereby LTT), as will be discussed in Section 4.3 for SN 2010al.

4.1.1 Library of models

For our automated routine for predicting the properties of Type-Ibn progenitors (described in Section 4.1.2), we have created a library of CMFGEN models. This library, displayed in Figure 4.1.1, spans over a wide range of $\dot{M}$, $0.1 - 8 \times 10^{-1}$ $M_{\odot}\mathrm{yr}^{-1}$and L_{SN}, $1 - 12 \times 10^{9}$ $L_{\odot}$. Each model in our library has $R_{in} = 10^{14}$ cm, consistent with a time of observation post-explosion of 4.6 days assuming an ejecta velocity of 10^4 km s^{-1}. However, once the automated check of the normalised spectrum returns a satisfactory prediction for the temperature and opacity structures, this initial assumption for R_{in} can be modified manually to better match the post-explosion time of the observation. Applying the scaling relations for $\dot{M}$ and L_{SN} with R_{in} mentioned in Section 2.2.4, we can retain the temperature and opacity structures while making improved predictions for the progenitor's properties.

Table 4.1 displays the number of super- and atomic-levels for the transitions included in our library of SN Ibn models while Table 4.2 displays their mass fractions of key

Table 4.1: CMFGEN atomic model used in our analysis of SNe Ibn.

Species	No. of super-levels	No. of atomic levels
He I	69	69
He II	30	30
C II	80	238
C III	51	84
C IV	64	64
N II	120	194
N III	41	82
N IV	44	76
O II	54	123
O III	88	170
O IV	78	154
Mg II	42	80
Al II	41	109
Al III	27	60
Si III	70	118
Si IV	22	33
S IV	51	142
S V	31	98
Cr III	23	112
Mn III	33	333
Fe III	104	1433
Fe IV	74	540
Fe V	50	220
Co III	28	174
Ni III	28	220

elements. A caveat with the predictions of our models is the degeneracy between these assumed mass fractions and the predicted progenitor properties. For example, the $\dot{M}$ may be overestimated if the prediction was based primarily on fitting He emission and the assumed He abundance is higher than the true value.

In order to improve the parameter-space resolution of the library of models, we have linearly interpolated between the spectra of any two CMFGEN models which differ in either L_{SN} or $\dot{M}$ by $< 50\%$. From comparisons of interpolated model spectra with spectra computed with a genuine CMFGEN model with identical input properties, we predict that these interpolated models introduce a maximum error of 5% within the modelled parameter space granted the variation in L_{SN} or $\dot{M}$ is $< 50\%$ as enforced. To predict the $T_\star$ and $T_{\rm eff}$ of an interpolated model, the $L \propto T^4$ relation of the Stefan Boltzmann Law (Eq. 2.3) was used. A comparison of two interpolated and genuine CMFGEN models with

Table 4.2: Mass fractions of key elements adopted by our Type-Ibn models.

Element	Mass fraction	$Z/Z_{\odot}$
H	0	0
He	9.864E-01	3.52E+00
C	5.583E-05	1.83E-02
N	8.172E-03	7.42E+00
O	1.319E-04	1.38E-02

L_{SN}=4.1×10^{10} and 5.5 ×$10^{10} L_{\odot}$ satisfied this luminosity-temperature relation to within 0.14% and 2.3% for $T_{\star}$ and $T_{\rm eff}$, respectively.

4.1.2 An automated routine for fitting SN Ibn spectra

We have created an automated approach to quickly compare each model in our library to a given early-time SN Ibn spectral observation. This is aided by the apparent lack of diversity amongst Ibn events compared to IIns (Hosseinzadeh et al., 2017) with many Ibn events exhibiting strong emission over the same emission lines. We select five commonly observed emission lines for an automatic comparison between a spectral observation and model. Table 4.3 displays the wavelength range over which the equivalent width is calculated, in addition to the chosen allowed threshold for each line. Models whose equivalent widths in any of the selected lines differ from that of the observation by more than their allowed threshold are ruled out. Successful models are then manually compared to the observed spectrum in absolute flux units, accounting also for the reddening effect on the observation (see Sec. 2.2.4). Models which provide good fits in both normalised and absolute flux units are compared to any available photometric observations for that event (see Sec. 2.2.5). Section 4.3 will describe in detail each of these steps necessary for our modelling of the event SN 2010al.

4.2 Spectral dependencies on L_{SN}, R_{in} and $\dot{M}$

In this section, we explore how the emergent spectrum depends on the model input parameters of L_{SN}, R_{in} and $\dot{M}$. We vary each of these input parameters individually to isolate their spectral effects. To better simulate real observations, we convolve each of these spectra with a Gaussian kernel of 500 km s^{-1} (resolving power $P_{\rm res}$ ∼600). This provides an obtainable resolution for observations. For the extended spectra shown in Figures 4.4, 4.9 and 4.16, we instead convolve with a Gaussian kernel of 5000 km s^{-1}

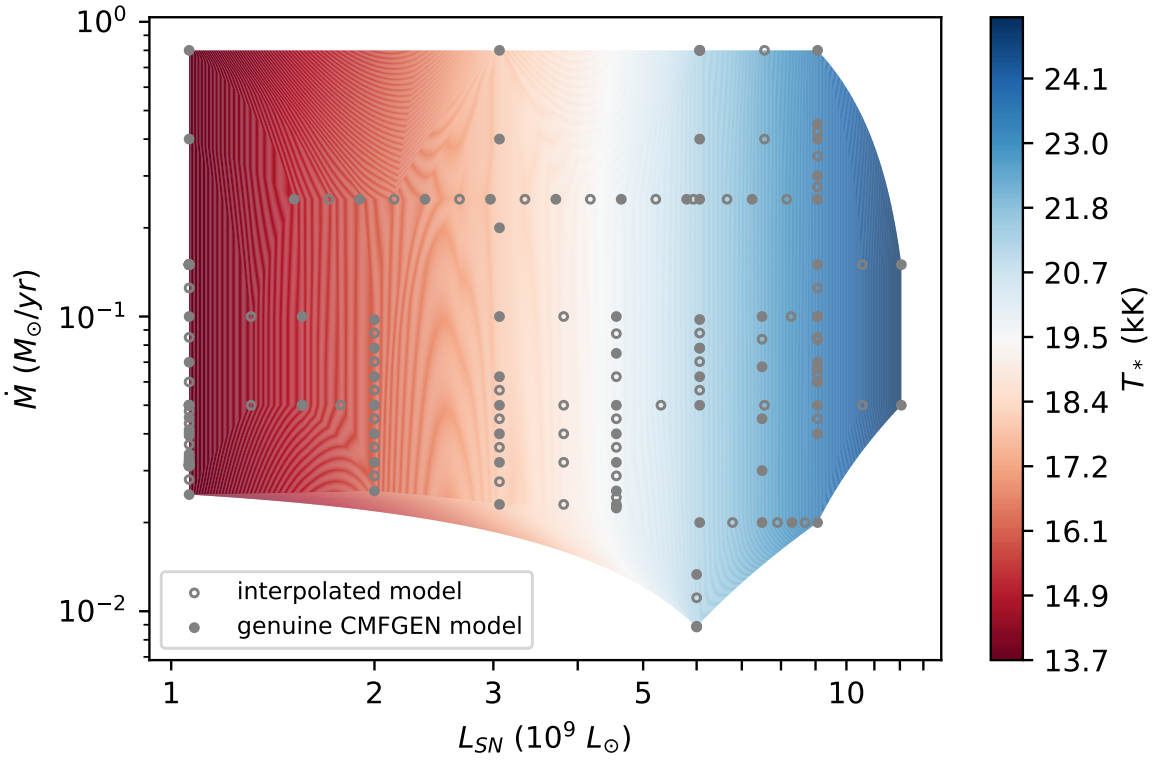

Figure 4.1: Library of our CMFGEN Type-Ibn progenitor models used in our automated routine for predicting properties from a given early-time, continuum-normalised spectral observation. Filled grey points indicate genuine CMFGEN models while unfilled indicate interpolated models. The colour gradient displays the $T_\star$ of the models. $R_{in} = 10^{14}$cm has been initially assumed for each model, as discussed in the text.

Table 4.3: Selected key emission lines which are prominent in early-Type-Ibn spectra. We perform an automatic integration for the equivalent width over the given wavelength range for each continuum normalised observation. Models which achieve an error below the chosen error-threshold in every line are considered good fits to the normalised spectrum.

Identification	λ (Å)	λ range (Å)	Max error threshold (%)
He I	4471	4300 - 4800	80
He II	4685.70	4450 - 5000	60
He I	5876	5750 - 6000	80
He I	6678	6350 - 6800	80
He I	7065	6865 - 7365	80

(resolving power P_{res} ~60), as to better display the continuum. For this investigation we assume a distance of 100 Mpc, which is representative of the currently detected SN Ibn sample. For the L_{SN}-varying models (Sec. 4.2.1), the following inputs were held constant: $\dot{M}$= 0.25 $M_{\odot}$yr^{-1}, R_{in} = 4 × 10^{14} cm while the R_{in}-varying models (Sec. 4.2.2) have $\dot{M}$= 0.25 $M_{\odot}$yr^{-1}and L_{SN} = 9 × 10^{9} $L_{\odot}$. For the $\dot{M}$-varying models (Sec. 4.2.3); L_{SN} = 9 × 10^{9} $L_{\odot}$, R_{in} = 4 × 10^{14} cm. The L_{SN}-varying models offer a great opportunity to isolate the effects of L_{SN} and the consequent variations in the temperature profile alone, hence we begin our discussion here. Both the $\dot{M}$- and R_{in}-varying models are more complex in that both the density profile and temperature profile are dependent on these properties.

4.2.1 Spectral dependency on L_{SN}

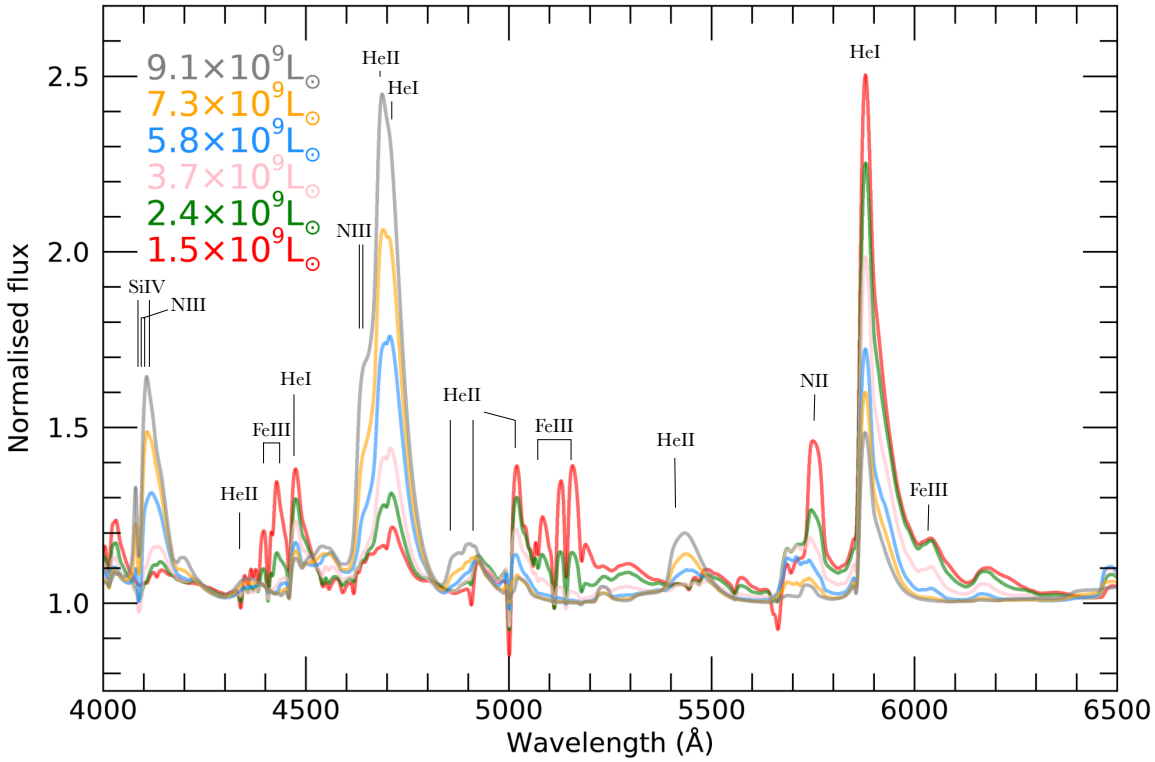

Figure 4.2: Continuum-normalised spectra of CMFGEN models with inputs differing only in L_{SN}. Different colours correspond to different values of L_{SN} as indicated by the legend. Vertical lines identify prominent spectral lines.

Figures 4.2 to 4.4 display the spectra of the L_{SN}-varying models. A larger L_{SN} causes stronger He II 4685 Å emission and weaker He I 5876 Å. This is due to differing ionisation

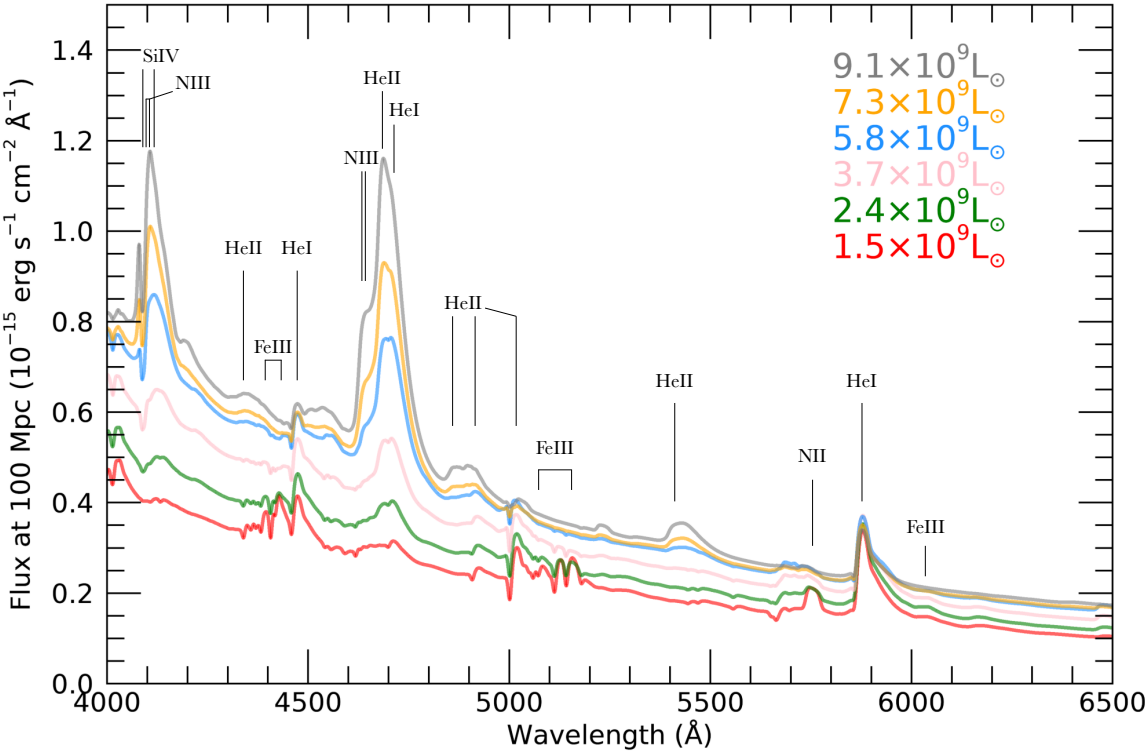

Figure 4.3: Spectra of CMFGEN models in absolute flux units, with inputs differing only in L_{SN}. Different colours correspond to different values of L_{SN} as indicated by the legend. Vertical lines identify prominent spectral lines.

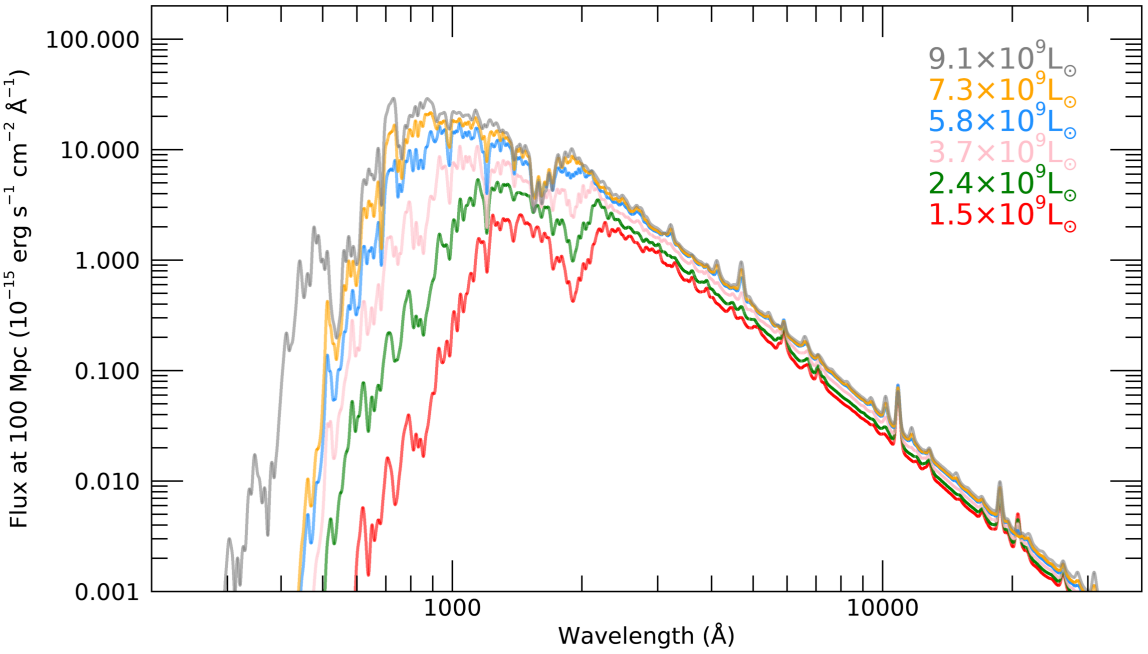

Figure 4.4: Identical to Figure 4.3, now showing the spectra over an extended wavelength range. The spectra have also been convolved with a Gaussian kernel of velocity 5000 rather than 500km s^{-1} to better show the continuum.

fractions of He arising from L_{SN}-dependent temperature profiles as will be shown. Across UV, optical and IR wavelengths, the continuum flux is greater for more luminous models. The peak of the continuum spectrum (which is in the UV for the parameters of our models) shifts to a lower wavelength for a hotter, more luminous model, consistent with Wien's Displacement Law, as shown in Figure 4.4.

Figures 4.5 and 4.6 delve deeper into the L_{SN}-varying models, showing their CSM profiles of density, opacity and optical depth, temperature, ionisation fractions of He and line formation of He I 5876 Å and He II 4685 Å. The central panel of Figure 4.5 shows that the Rosseland mean opacity (Eq. 2.7) profile of the CSM closely follows the profile for the density of ions. It exhibits both a steady decline as well as a bump in the inner-most CSM resulting from the greater ionisation of elements, which increases the number density of free electrons and hence the electron-scattering opacity. The Rosseland mean optical depth τ_{Ross}, accordingly falls off with increasing depth into the CSM. Over the broad range of L_{SN} considered in this parameter study, there is little variation in the resulting optical depth profiles (lower panel of Fig. 4.5). A more luminous model results in a slight extension of the enhanced opacity region due to the ionisation of more atoms. However, the variation in optical depth arising from varying the L_{SN} is negligible compared to that

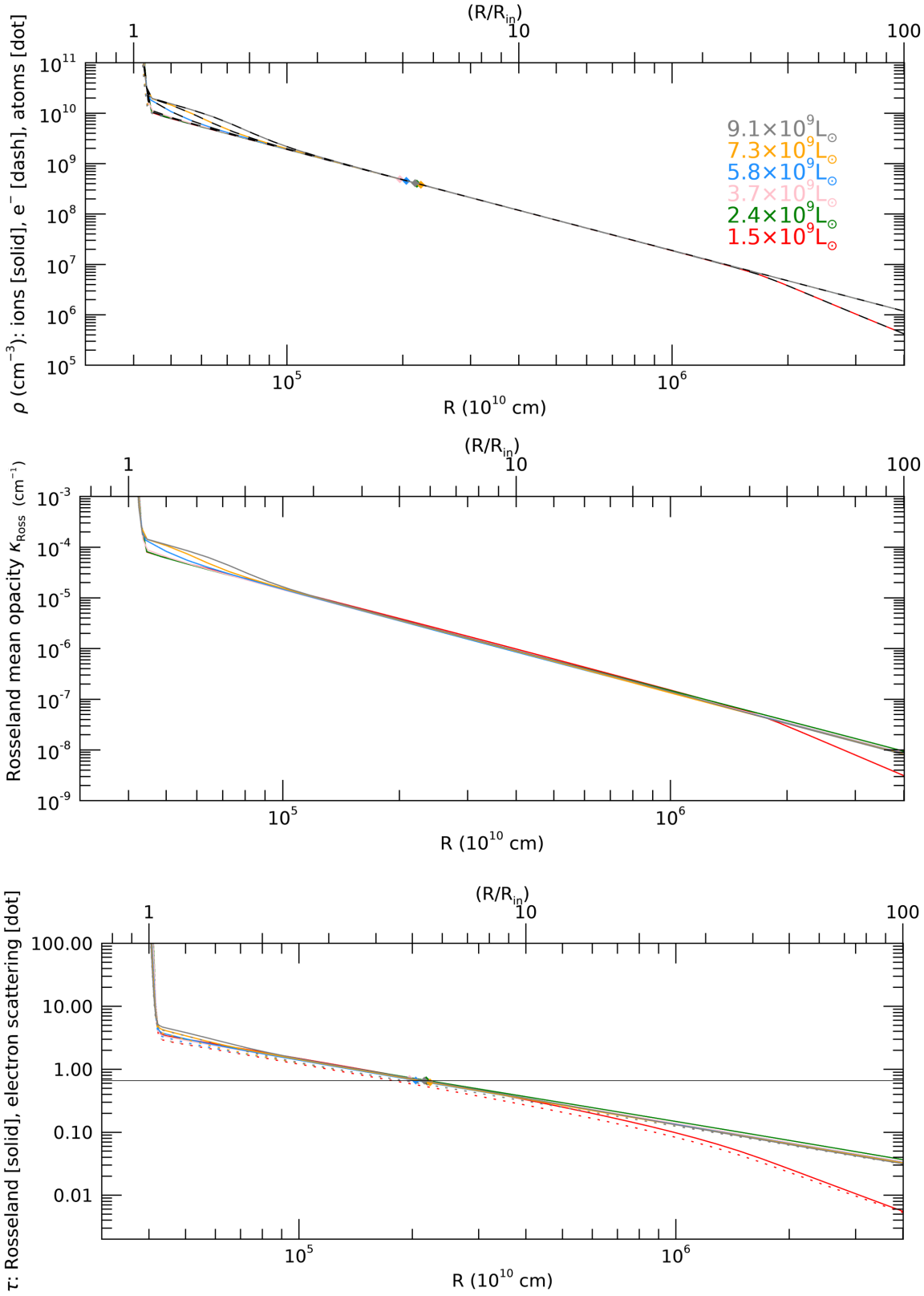

Figure 4.5: CSM profiles of density (upper), opacity (central) and optical depth (lower). The colour corresponds to the L_{SN} of the model which is the only difference in the input of the models. The line-style corresponds to the text on the relevant y-axis. The diamond symbols indicate the depth at which the CSM is no longer optically thick.

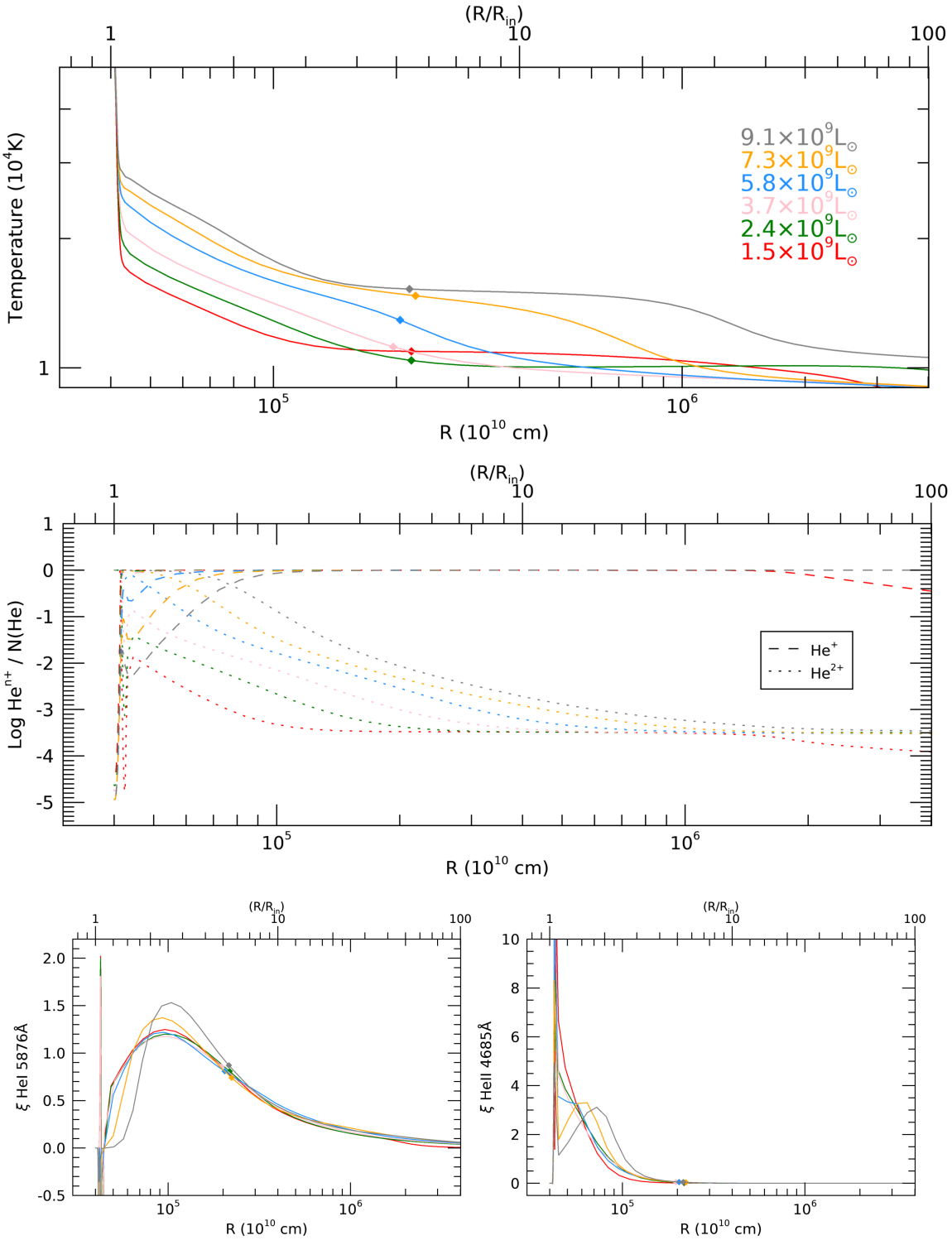

Figure 4.6: CSM profiles of temperature (upper), ionisation fraction of He (central), line formation regions (lower) of He I 5876 Å (left) and He II 4685 Å (right). The colour corresponds to the L_{SN} of the model which is the only difference in the input of the models. $\xi(R)$ relates to the equivalent width of the line as: EW=$\int_{\infty}^{R_{in}} \xi(R)\, d(log(R))$ and highlights the formation region of the line.

from varying R_{in} or $\dot{M}$ which will be studied in the subsequent sections.

As shown in the upper panel of Figure 4.6, temperature decreases with increasing depth into the CSM. The large opacity in the optically-thick inner region leads to strong absorption and hence high temperatures. Consequently, following the opacity profile, the temperature falls off steeply with increasing depths into the CSM until the edge of the optically thick region is reached ($R_{\tau=2/3}$), as marked by the diamonds in all CSM profile figures. The high temperature in this inner region is due mostly to line-blanketing by numerous close-together Fe absorption lines, predominantly Fe III/Fe IV for the $L_{SN} = 1.5 \times 10^9\ L_\odot$ model while the hotter temperature of the $L_{SN} = 9.1 \times 10^9\ L_\odot$ model results in Fe V being the primary source of line-blanketing. These closely spaced UV absorption lines warm the CSM either through absorption or back-scattering of photons in a process known as back-warming. Conservation of energy implies that where the CSM becomes optically thin coincides with a strong drop in temperature as the photons can escape into the emergent spectrum without being absorbed. The dependence of the temperature within the optically thick CSM on L_{SN} (Fig. 4.6) and R_{in} (Fig. 4.12 and 4.13) follows the Stefan Boltzmann Law (Eq. 2.3), as this region is in a state of LTE. This states that a slightly more luminous model will exhibit a significantly hotter temperature profile, if R_{in} is not varied. Similarly, if two models with identical L_{SN} differ only in R_{in}, the larger R_{in} will produce a cooler temperature profile.

The central panel of Figure 4.6 displays the ionisation fraction of He throughout the CSM for various luminosities. Within the temperature regime covered by these models, the hotter temperatures of the inner region of the CSM are better suited to the excitement of He to the He^{2+} rather than the He^{+} state. As the temperature drops going further into the CSM, at some depth it approaches the excitation temperature needed for He^{+}, leading to the respective rise and fall of the He^{+} and He^{2+} states. A hotter temperature profile results in this depth being reached further into the CSM, once the temperature reaches ∼20000 K according to our models.

The lower panel of Figure 4.6 displays the line formation regions of He I 5876 Å (left) and He II 4685 Å (right). The exact region in which the lines are formed depends on a number of factors, such as the density, optical depth and temperature profiles of the CSM. In order for a particular recombination line to be observable in the emergent spectrum, it must be produced readily in a region where there is a high number of free electrons and the ion required for the particular transition, He^{2+} for He II 4685 Å and He^{+} for He I 5876 Å. Hence, the line strength of such recombination lines are typically proportional to the density squared. However, while a higher density raises the number of available emitters

and hence the probability of a line photon being emitted, it also raises the optical thickness at that radius. This greater optical thickness raises the probability that an emitted line photon is absorbed rather than allowed to escape out to the emergent spectrum. Instead, the line photon likely thermalises, eventually contributing to the continuum spectrum. This competing emission and absorption of line photons results in a radius at which the line formation peaks[1]. It was mentioned that hotter temperatures in the optically-thick, inner region of the CSM, due to a higher input L_{SN} for example, leads to the switch between a He^{2+}- to a He^{+}-dominant ionisation fraction occurring further into the CSM. Ultimately, this causes the formation of He I lines to occur further into the CSM than He II lines. Pushing the formation of He I lines out to a greater CSM depth where the density is lower raises the ratio of He II/He I in the emergent spectrum, as previously noted in Figure 4.2.

4.2.2 Spectral dependency on R_{in}

Figures 4.7 to 4.9 displays the spectral effects of varying R_{in}. A smaller R_{in} strengthens individual emission lines relative to the continuum as shown in Figure 4.7. Considering the spectra in absolute flux units as in Figure 4.8, it becomes clear that this is due to both a weaker continuum flux in the optical, and generally stronger line emission for a smaller R_{in}. The weaker continuum flux at optical wavelengths for a smaller R_{in} results from Wien's Displacement Law. The hotter temperature (explained below) arising from a smaller R_{in} results in the continuum emission peaking at a lower wavelength, as shown in Figure 4.9. This shifts the continuum flux of lower R_{in} models blue-ward, redistributing continuum flux from the optical into the UV region.

Figures 4.10 to 4.13 compare profiles of various properties of the CSM for varying R_{in} models. Figures 4.10 and 4.12 give the depth into the CSM in units of 10^{10} cm, whereas Figures 4.11 and 4.13 normalise the depth with each model's specific R_{in}. Density profiles are shown in the upper panels of Figures 4.10 and 4.11. The assumed density profile of the CSM given by Equation 2.9 dictates that $\rho_{CSM}(R) \propto R^{-2}$. Hence, a smaller R_{in} strengthens the emission lines (noted for Figs. 4.7 and 4.8) through raising the number of their available emitters. While a higher CSM density favours stronger line-emission, the density profile cannot be altered without affecting the temperature profile (upper panels

[1] Due to the steepness of the assumed density profile for the shock layer at the innermost depths near R_{in}, some models exhibit a sharp, narrow spike in line formation (emission) very close to R_{in} with a subsequent drop of equal intensity (absorption) at a slightly larger depth into the CSM. However, as the emitted photons are subsequently absorbed, these photons do not reach the emergent spectrum. The observed emission lines are instead produced further into the CSM, in the broader ξ component.

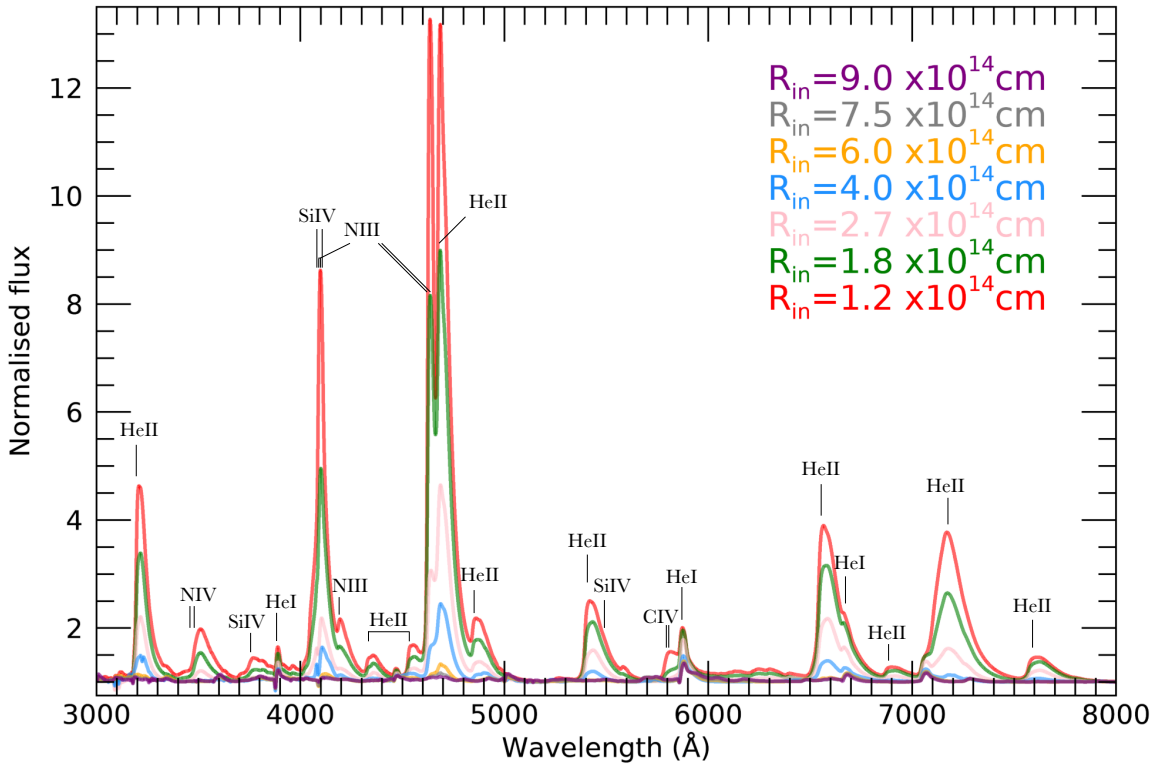

Figure 4.7: Continuum-normalised spectra of CMFGEN models with inputs differing only in R_{in}. Different colours correspond to different values of R_{in} as indicated by the legend. Vertical lines identify prominent spectral lines.

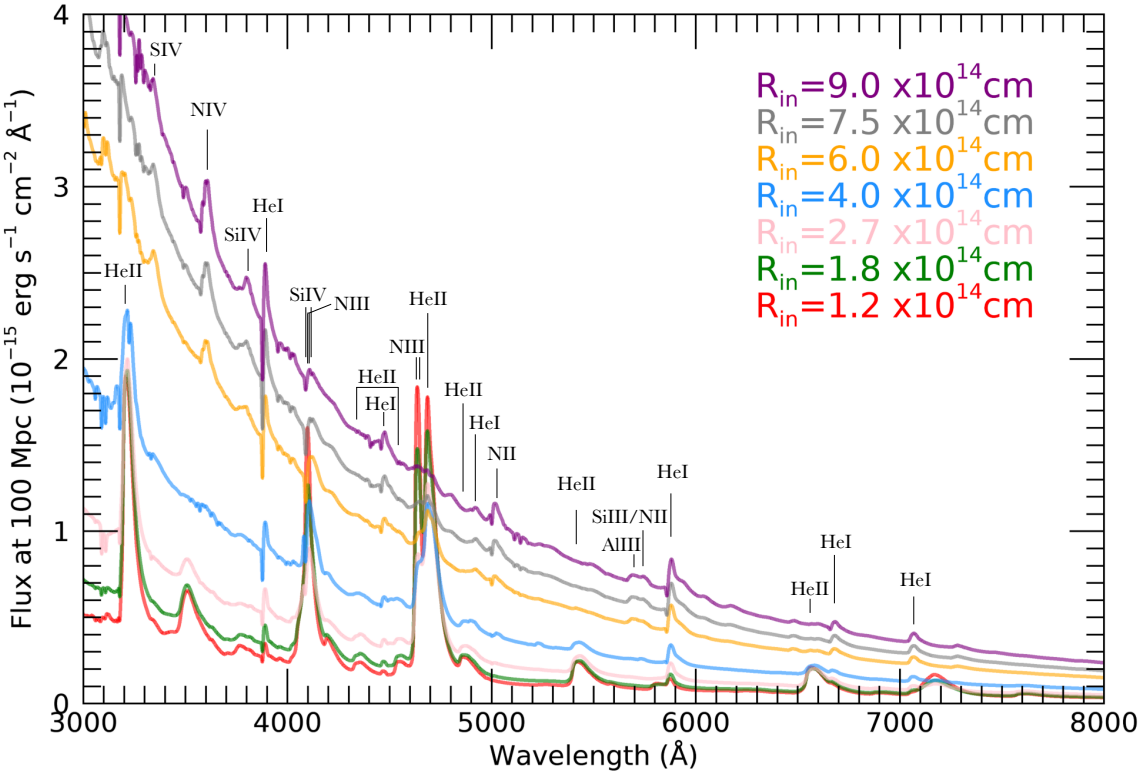

Figure 4.8: Spectra of CMFGEN models in absolute flux units, with inputs differing only in R_{in}. Different colours correspond to different values of R_{in} as indicated by the legend. Vertical lines identify prominent spectral lines.

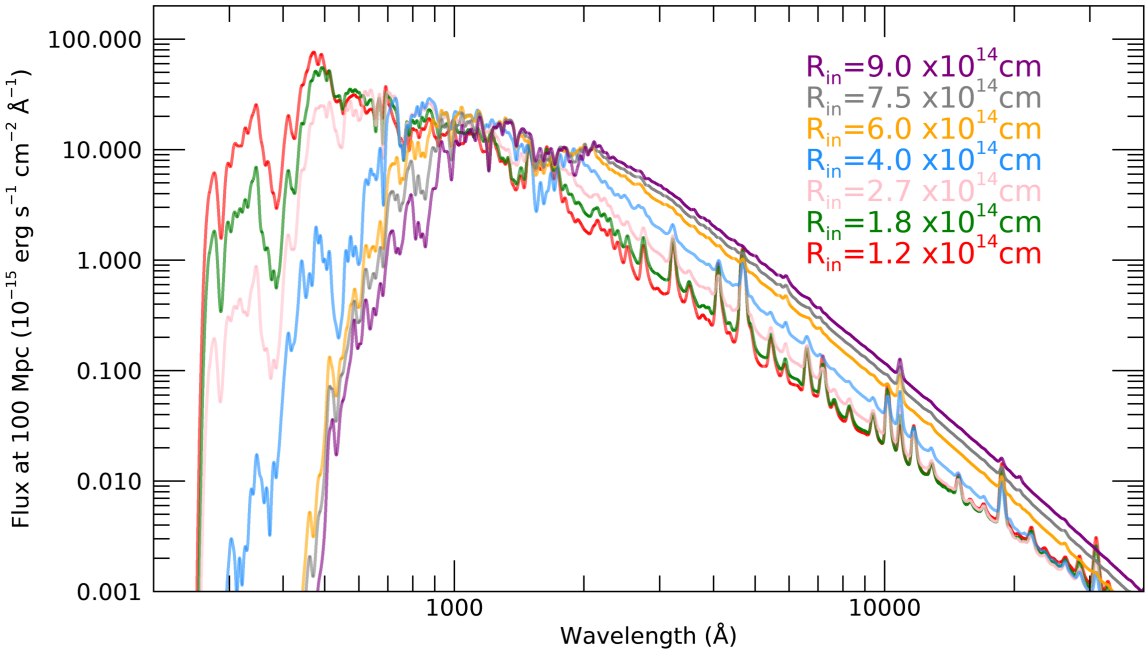

Figure 4.9: Identical to Figure 4.8, now showing the spectra over an extended wavelength range. The spectra have also been convolved with a Gaussian kernel of velocity 5000 rather than 500km s^{-1} to better show the continuum.

of Figs. 4.12 and 4.13), due to the coupling between the RT (Eq. 2.2) and SE equations (Eq. 2.4). A lower R_{in} yields hotter temperatures in the optically thick region of the CSM in accordance with the Stefan Boltzmann Law (Eq. 2.3). This unavoidable temperature variation could potentially lower the fraction of available ions in the required state for the formation of a particular line, resulting in weaker spectral emission despite a greater overall density for the CSM. In summary, raising the density from either decreasing R_{in} (or increasing $\dot{M}$) acts to strengthen all line-emission, however, consequential temperature effects may cause certain lines to weaken or strengthen beyond this.

The central panels of Figures 4.12 and 4.13 display the effect of R_{in} on the ionisation fraction of He. As seen for the L_{SN}-varying models, hotter CSM temperature profiles due to a smaller R_{in} result in the switch from a He^{2+} to He^{+}-dominated ionisation fraction occurring further into the CSM. Again, this pushes the formation of He I 5876 Å and He II 4685 Å to greater CSM depths, shown in the lower panels of Figures 4.12 and 4.13.

While $R_{\tau=2/3}$ shows little variation for different L_{SN}, it is highly dependent on the density profile and hence variations in R_{in}, as seen in the optical depth profiles in Figures 4.10 and 4.11. The upper panels of these figures also reveal that lower R_{in} models exhibit an enhanced density of ions and free electrons in the innermost region of the CSM, above

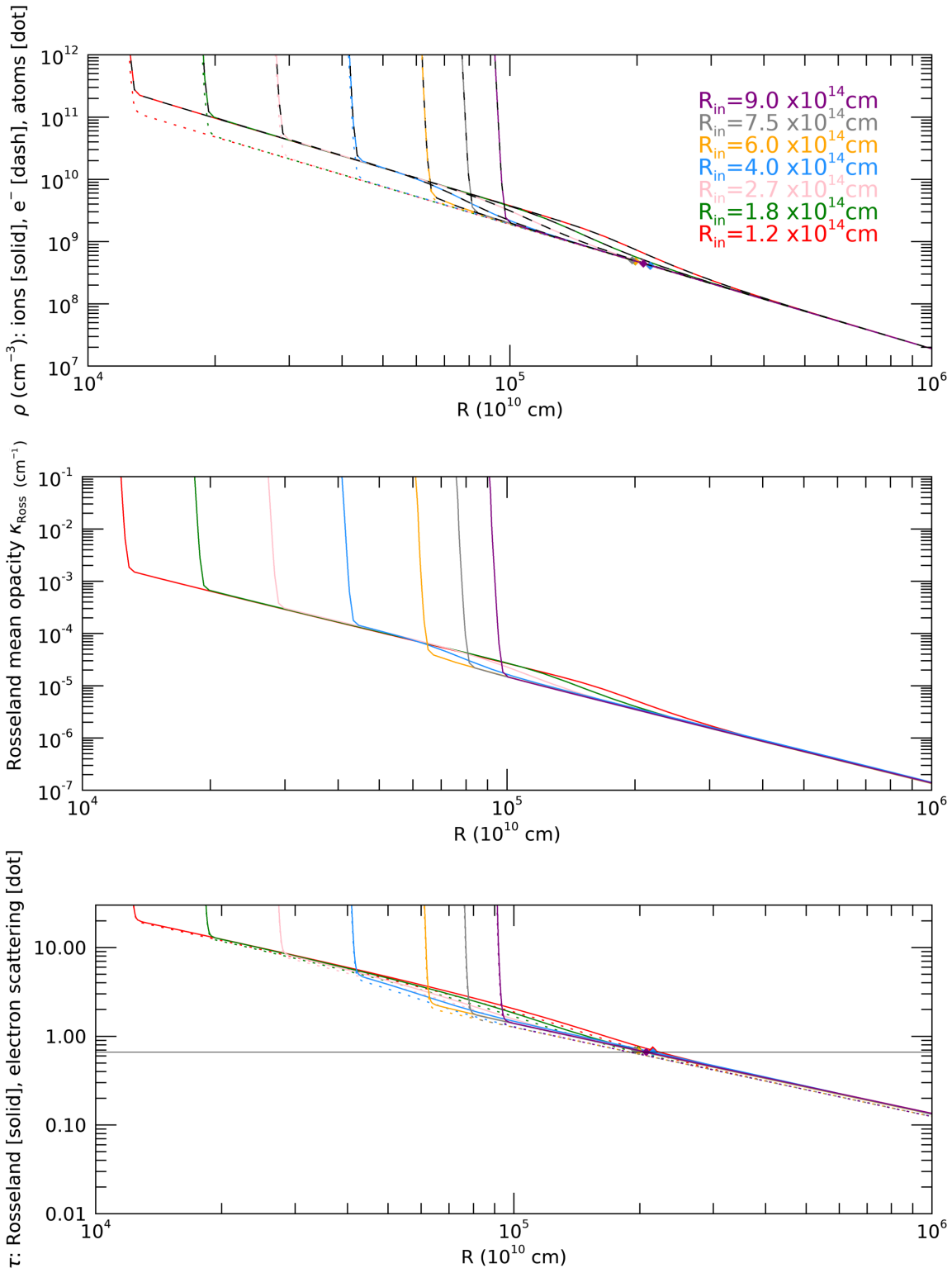

Figure 4.10: CSM profiles of density (upper), opacity (central) and optical depth (lower). The colour corresponds to the R_{in} of the model which is the only difference in the input of the models. The line-style corresponds to the text on the relevant y-axis. The diamond symbols indicate the depth at which the CSM is no longer optically thick.

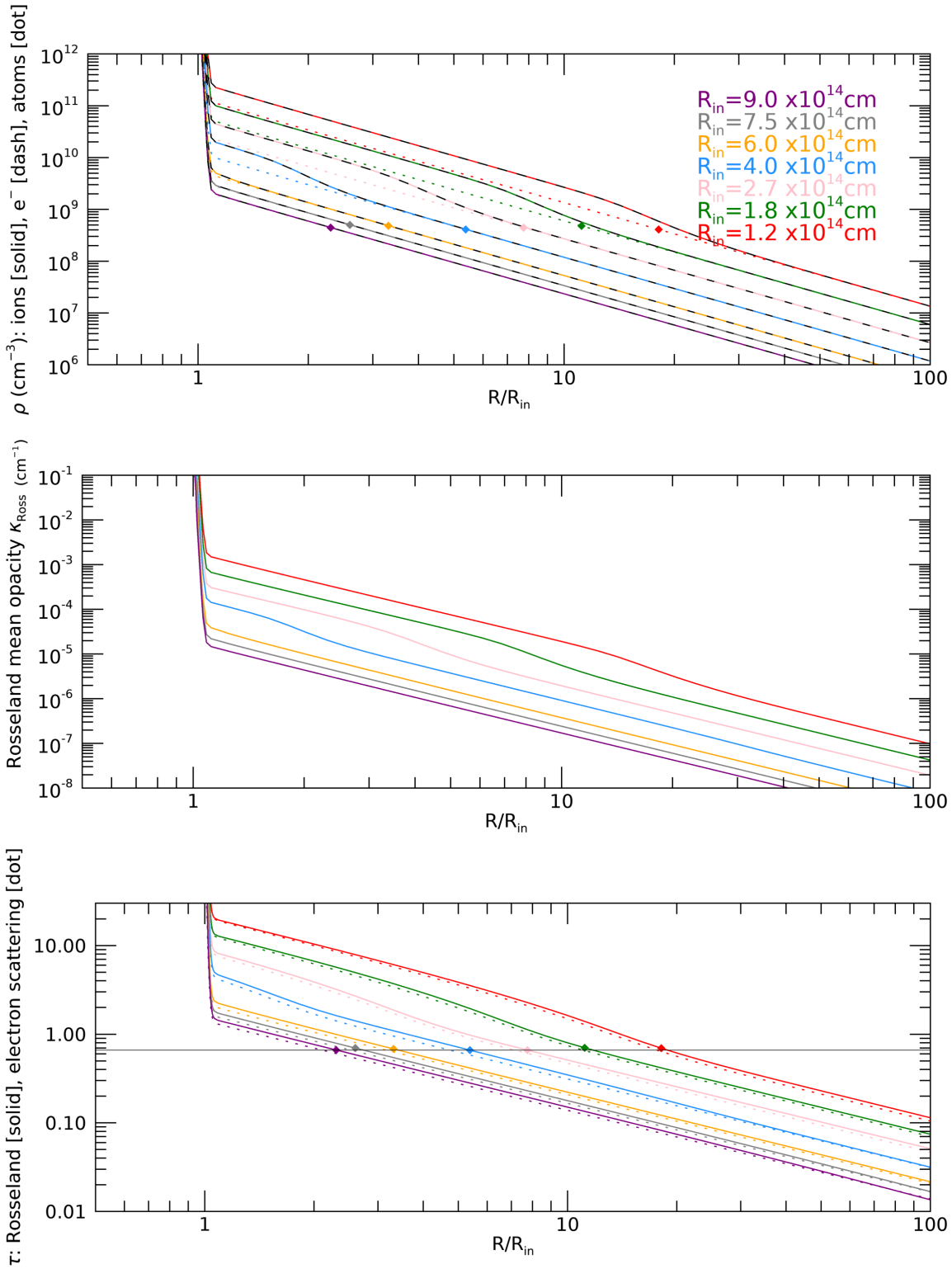

Figure 4.11: Identical to Figure 4.10 but the depth into the CSM, R, is now displayed in units of R_{in}.

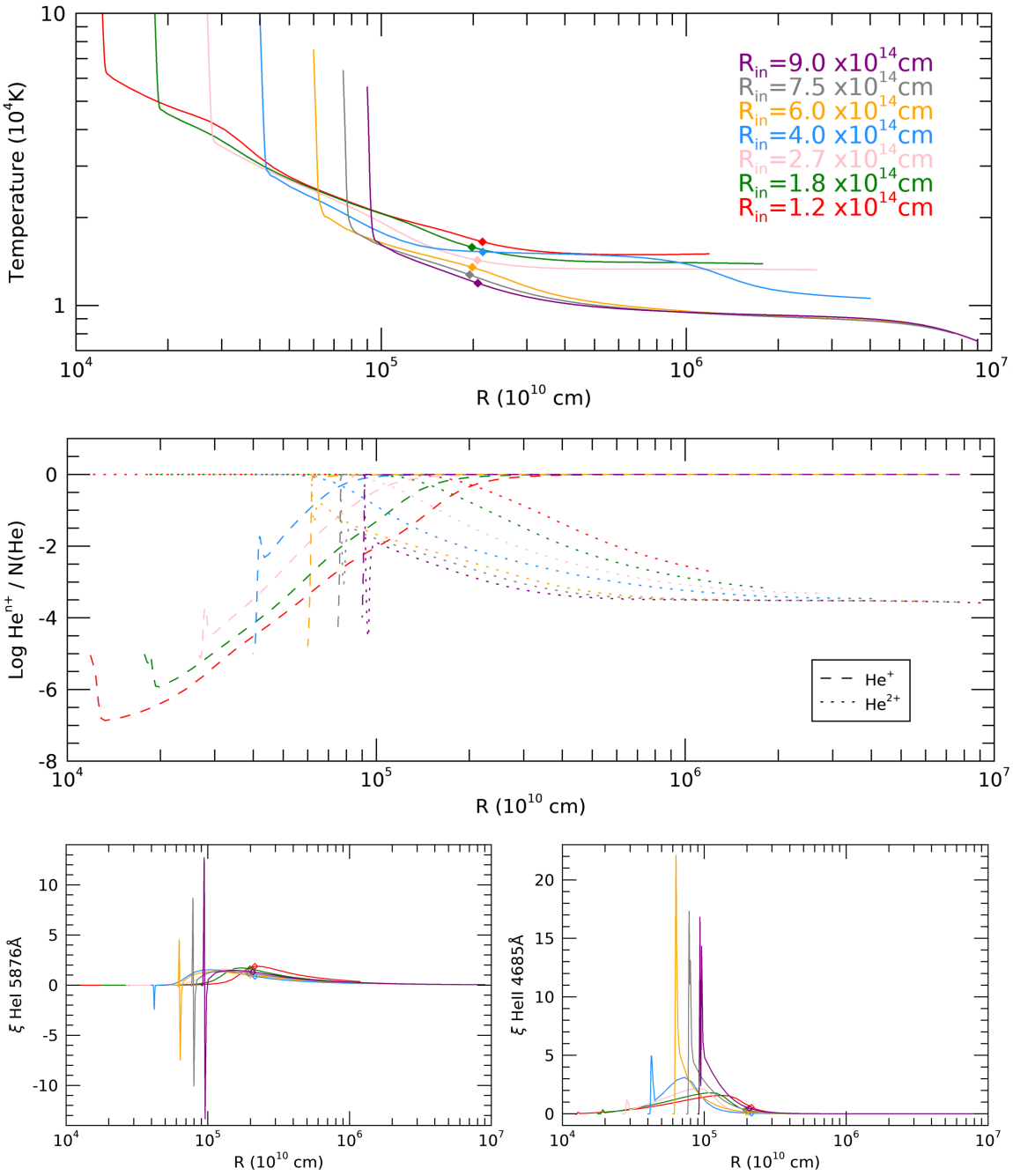

Figure 4.12: CSM profiles of temperature (upper), ionisation fraction of He (central), line formation regions (lower) of He I 5876 Å (left) and He II 4685 Å (right). The colour corresponds to the R_{in} of the model which is the only difference in the input of the models. $\xi(R)$ relates to the equivalent width of the line as: EW=$\int_{\infty}^{R_{in}} \xi(R)\, d(log(R))$ and highlights the formation region of the line.

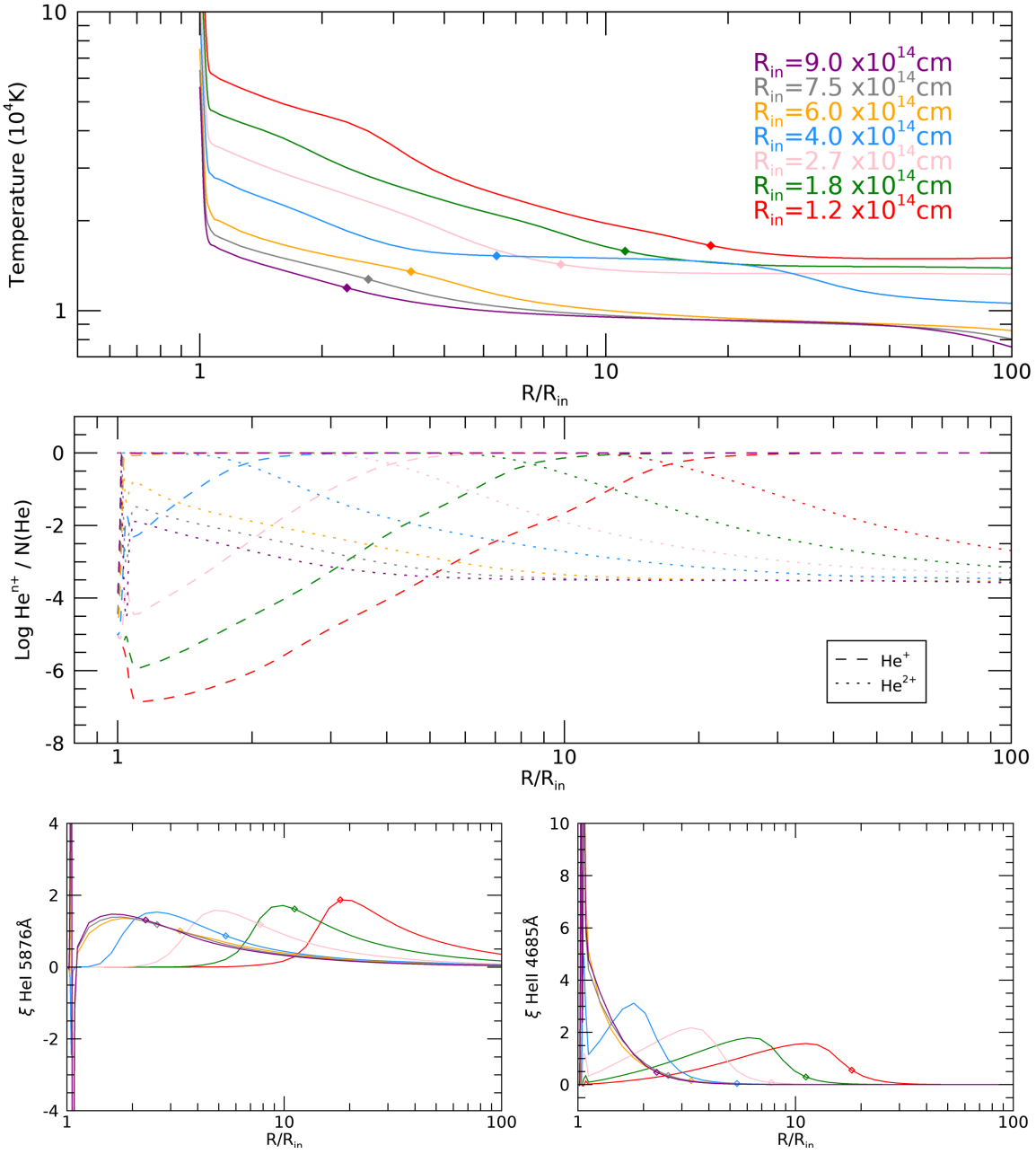

Figure 4.13: Identical to Figure 4.12 but the depth into the CSM, R, is now displayed in units of R_{in}.

the assumed $\rho_{CSM}(R) \propto R^{-2}$ dependence. This is owed to the hotter temperatures of this region. The enhanced density region extends further into the CSM for hotter, lower R_{in} models, similar to that seen for more luminous models. The greater general density as well as the enhanced densities of ions and free electrons in the inner CSM for lower R_{in} models lead to greater opacities, shown in the central panels of Figures 4.10 and 4.11.

4.2.3 Spectral dependency on $\dot{M}$

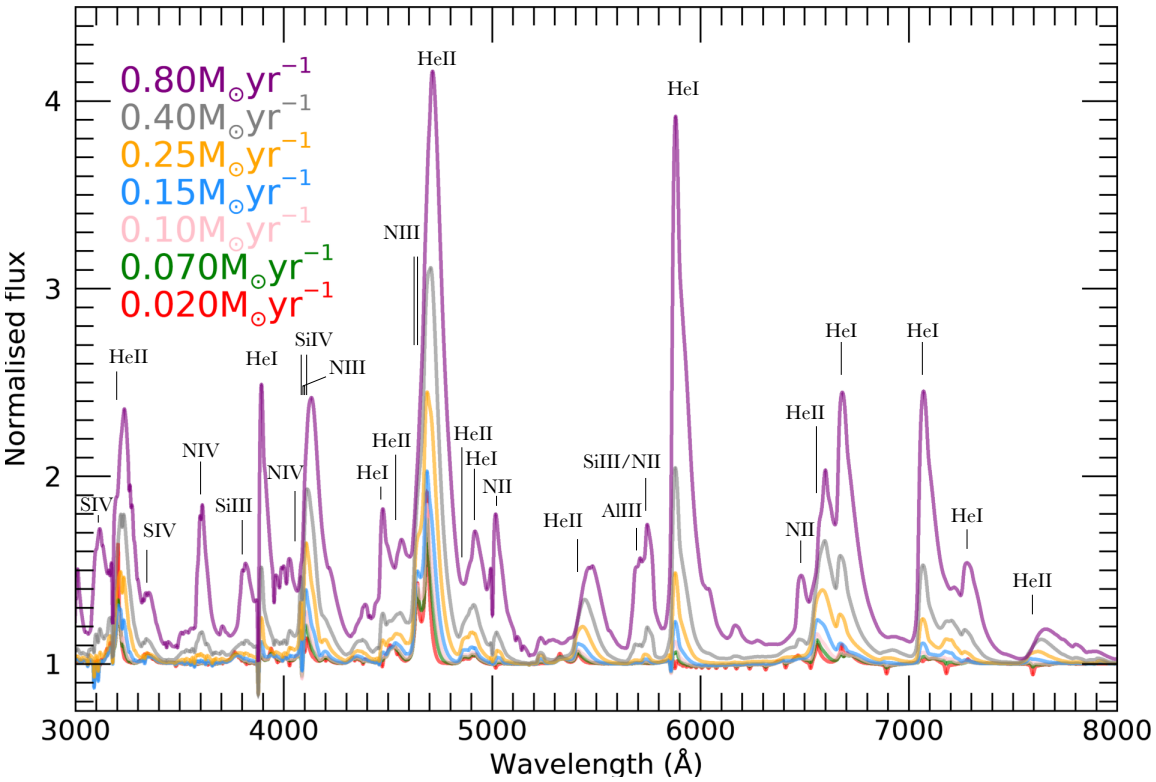

Figure 4.14: Continuum-normalised spectra of CMFGEN models with inputs differing only in $\dot{M}$. Different colours correspond to different values of $\dot{M}$ as indicated by the legend. Vertical lines identify prominent spectral lines.

Many of the effects discussed in the previous two sections also apply in variations of $\dot{M}$. The upper panel of Figure 4.17 clearly shows the $\rho_{CSM}(R) \propto \dot{M}$ dependency, in accordance with Equation 2.9. This causes a larger $\dot{M}$ to produce many effects similar to those seen for a smaller R_{in}. This includes greater opacities and optical depths throughout the CSM, as shown in the central and lower panels of Figure 4.17, respectively. As mentioned, a larger optical depth leads to further back-warming, producing hotter temperatures in the optically thick region of the CSM (see upper panel of Fig. 4.18).

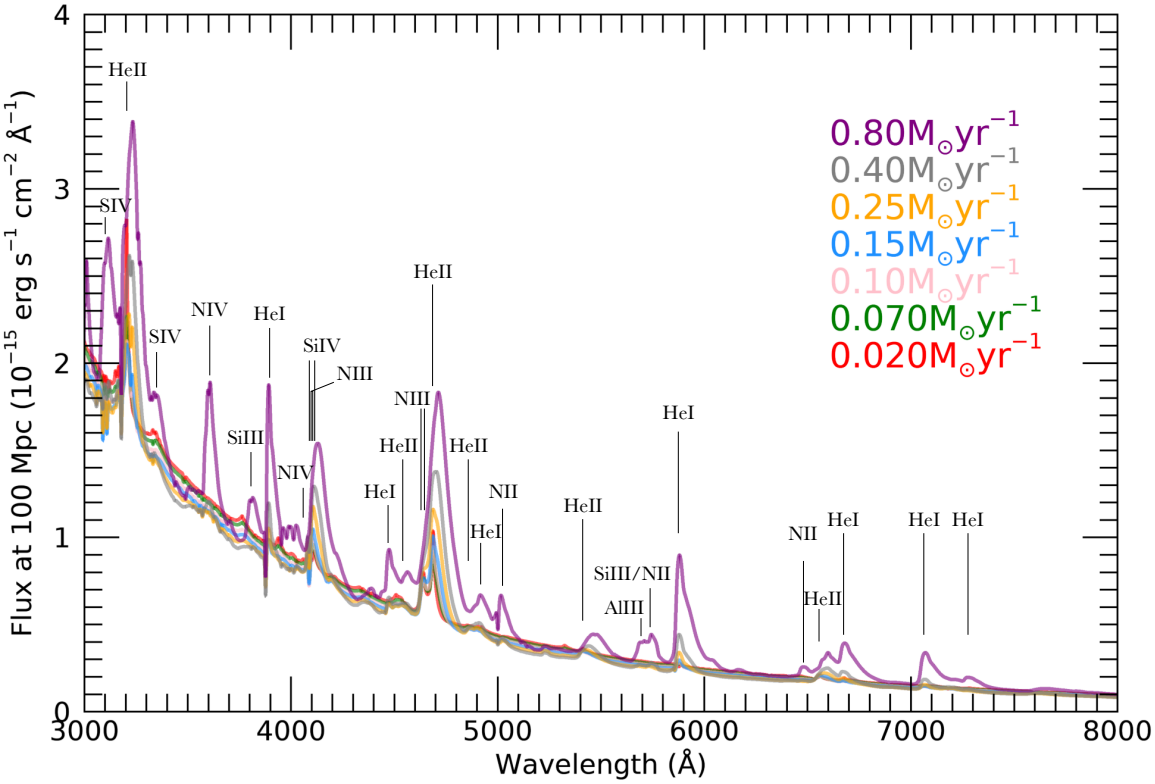

Figure 4.15: Spectra of CMFGEN models in absolute flux units, with inputs differing only in $\dot{M}$. Different colours correspond to different values of $\dot{M}$ as indicated by the legend. Vertical lines identify prominent spectral lines.

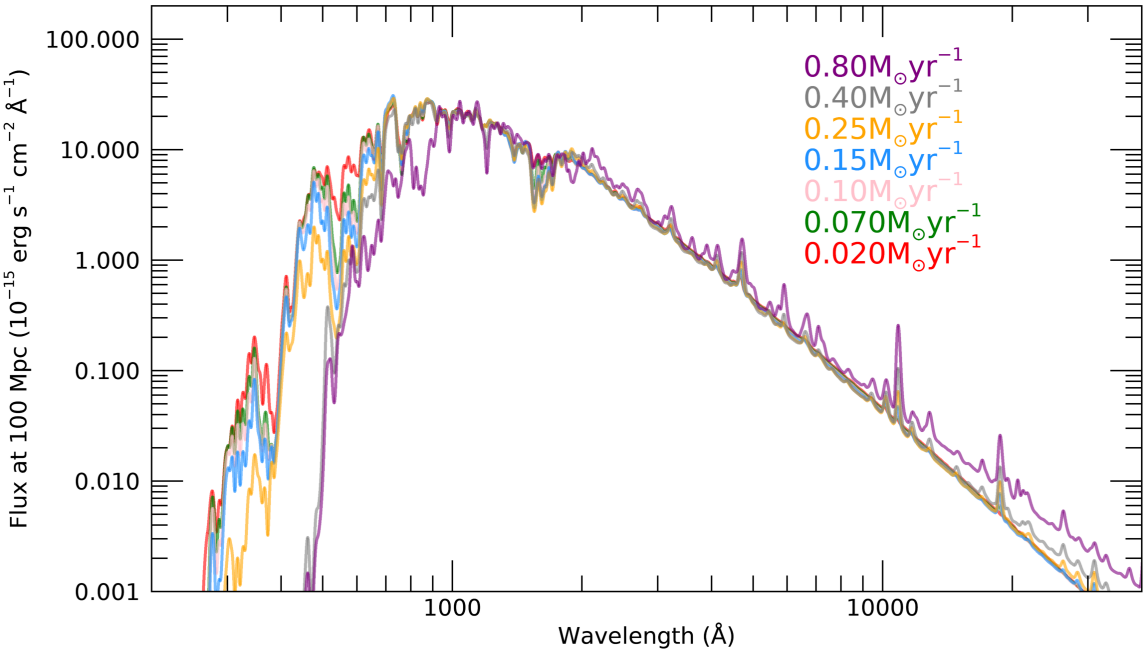

Figure 4.16: Identical to Figure 4.15, now showing the spectra over an extended wavelength range. The spectra have also been convolved with a Gaussian kernel of velocity 5000 rather than 500km s^{-1} to better show the continuum.

Figures 4.14 to 4.16 display the emergent spectra of the $\dot{M}$-varying models. The larger $\dot{M}$ models exhibit stronger line-emission due to the greater density of their CSM. As noted in Section 4.2.2, this increase is not necessarily uniform across all line-emission, due to indirect temperature effects. Compared to variations in L_{SN} and R_{in}, a change in $\dot{M}$ has a negligible effect on the continuum at optical wavelengths (Fig. 4.15). The continuum flux over a more extended wavelength range such as in Figure 4.16 however does reveal dependencies with $\dot{M}$. Firstly, the two highest $\dot{M}$ models feature an excess of continuum emission compared to the lower $\dot{M}$ models, growing steadily with increasing wavelength. This is caused by free-free emission, which scales with the square of the CSM density. This free-free emission leads to a notable IR excess for the highest $\dot{M}$ models. Secondly, the continuum flux of the higher $\dot{M}$ models peak at slightly larger wavelengths. This is the result of Wien's Displacement Law. Unlike the denser, lower-R_{in} models which (for the most part) exhibit hotter temperatures thorough-out the entirety of the CSM, the higher $\dot{M}$ models generally show higher temperatures in the optically thick CSM, and lower temperatures in the optically thin CSM. The slight decrease in temperature in the optically thin region where the continuum radiation originates, shifts the peak of the continuum to slightly larger wavelengths.

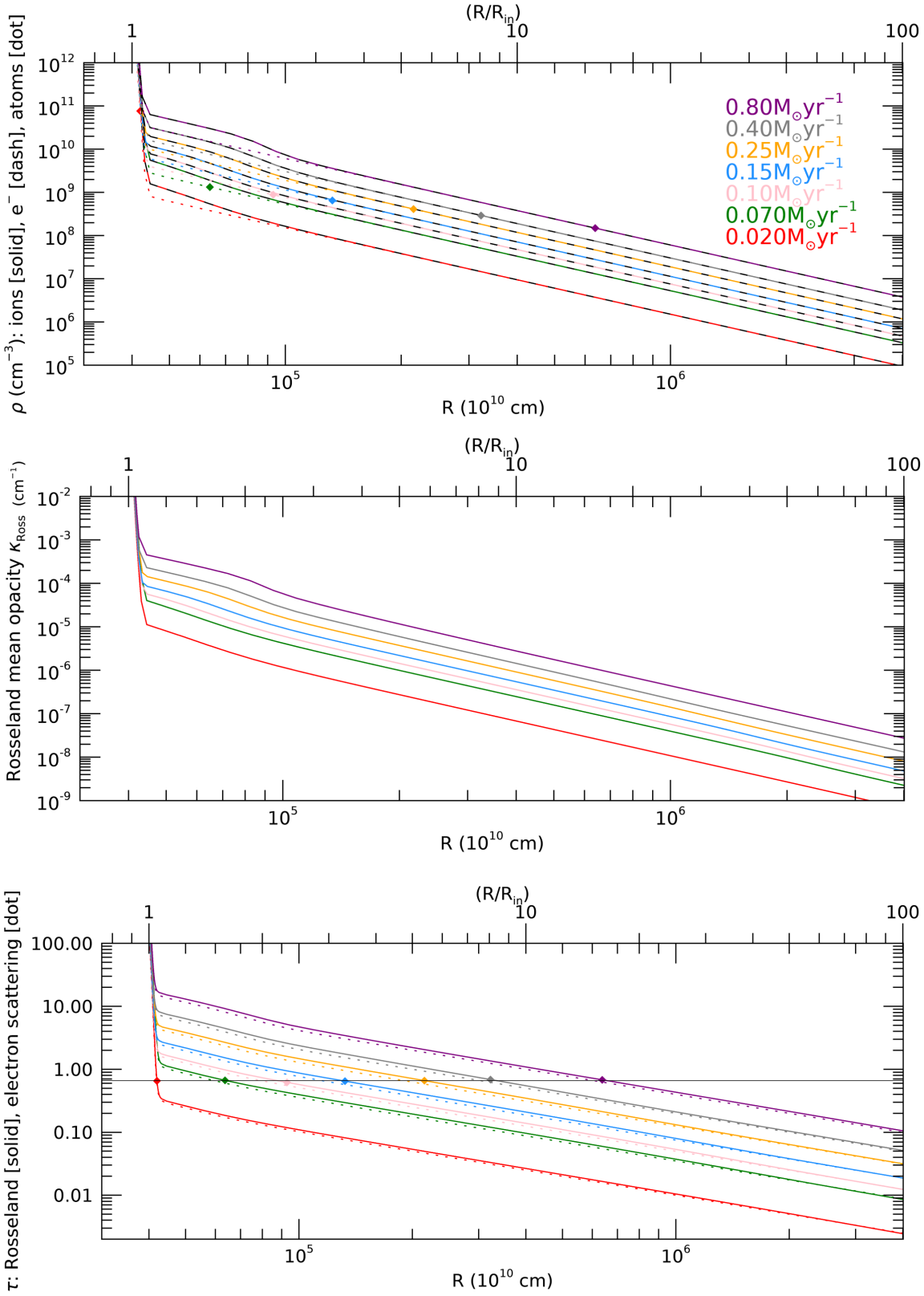

Figure 4.17: CSM profiles of density (upper), opacity (central) and optical depth (lower). The colour corresponds to the $\dot{M}$ of the model which is the only difference in the input of the models. The line-style corresponds to the text on the relevant y-axis. The diamond symbols indicate the depth at which the CSM is no longer optically thick.

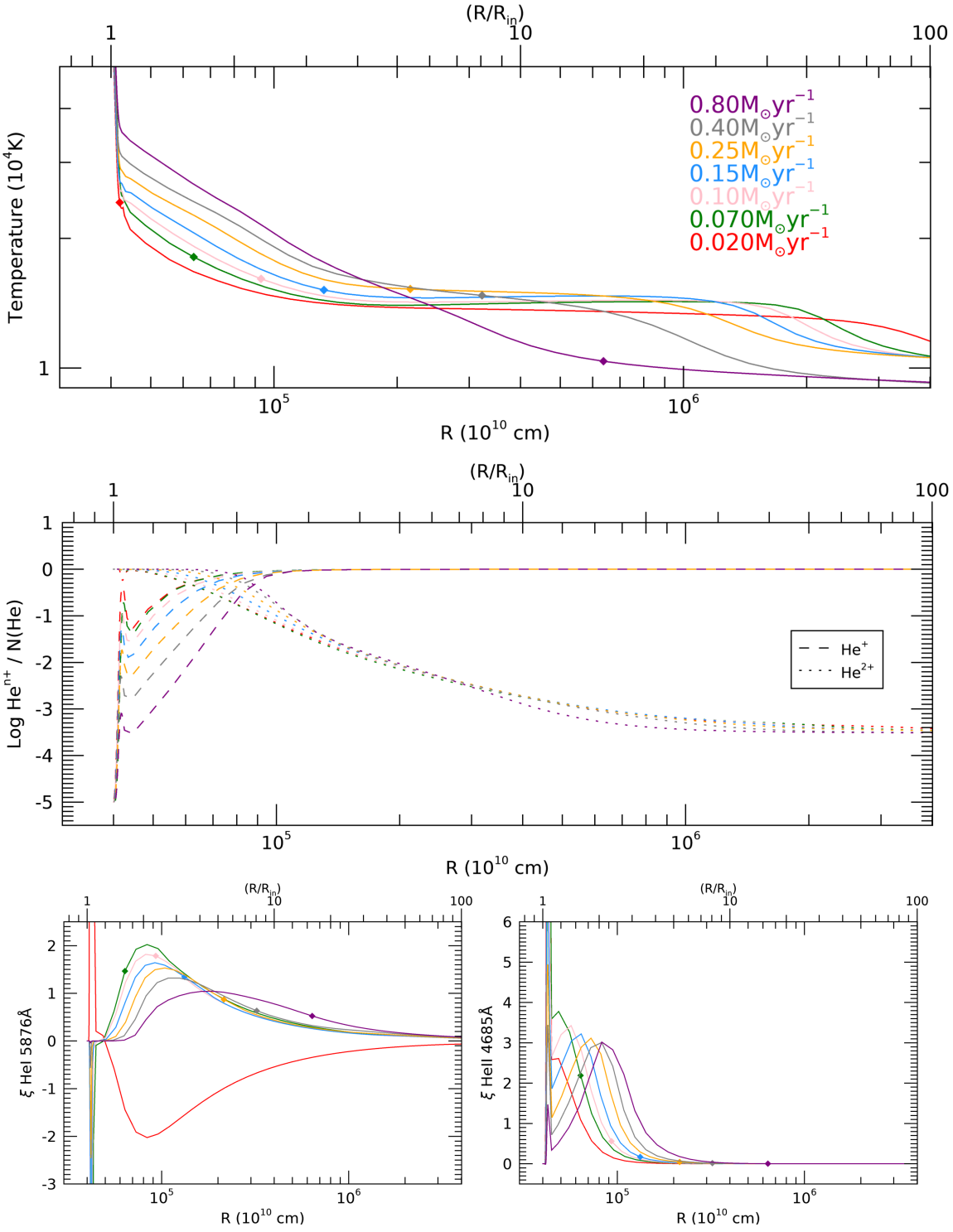

Figure 4.18: CSM profiles of temperature (upper), ionisation fraction of He (central), line formation regions (lower) of He I 5876 Å (left) and He II 4685 Å (right). The colour corresponds to the $\dot{M}$ of the model which is the only difference in the input of the models. $\xi(R)$ relates to the equivalent width of the line as: EW=$\int_{\infty}^{R_{in}} \xi(R)\, d(log(R))$ and highlights the formation region of the line.

The central and lower panels of Figure 4.18 display the ionisation fraction of He and formation regions of He I 5876 Å and He II 4685 Å respectively. A larger $\dot{M}$ is seen to extend the He^{2+} region further into the CSM due to the larger temperatures in the optically thick region. However, as the variation in this temperature is mild in comparison to that from L_{SN}- and R_{in}-variations, there is less variation in the ionisation fractions of elements and the resulting formation region of their lines. Accordingly, a change in the spectrum's He I/He II ratio is less drastic for a variation in $\dot{M}$, compared to the ratio change resulting from variations in L_{SN} or R_{in}.

4.3 Properties of SN 2010al from CMFGEN modelling

In Section 4.2, we showed how properties of the progenitor and SN affect the resulting spectra. We now focus on fitting an early-time spectrum of a particular SN Ibn event, SN 2010al. SN 2010al remains one of the earliest spectroscopically observed Type-Ibn SNe, with the spectrum we fit our models to being obtained just 5.7 days post-explosion with the FAST spectrograph of the Tillinghast Telescope (Fabricant et al., 1998). We obtained this publicly available spectrum through the Open Supernovae catalogue (Guillochon et al., 2017). Fabricant et al. (1998) report a spectral resolution of $\Delta\lambda = 3$Å, corresponding to a resolving power between 1133-2433 over the ∼3400-7300 Å spectral coverage for this observation. After normalising this spectrum with respect to the continuum, our automated spectral fitting routine outlined in Section 4.1.2 returned best-fit models. Here, we describe how we improve upon these preliminary models.

We begin by ensuring our models provide adequate fits to the observed spectrum in absolute flux units as opposed to the continuum-normalised spectrum alone. Section 2.2.4 describes this process in detail. For SN 2010al, the preliminary best-fit models from our automated fit to the normalised spectrum underestimates the absolute flux of the observation, suggesting accurate temperature and opacity structures, while L_{SN} is being underestimated. Therefore, we scale L_{SN} to the value required to match the observed continuum flux, applying the mentioned scaling relations for retaining the temperature and opacity profiles. These scalings result in a predicted $R_{\rm in}$ of 1.2 $\times 10^{15}$ cm for SN 2010al. We also find that $E(B-V) = -0.4$ is required to reproduce the slope of the spectral continuum of SN 2010al, hence we artificially redden each of our SN 2010al models by this colour excess.

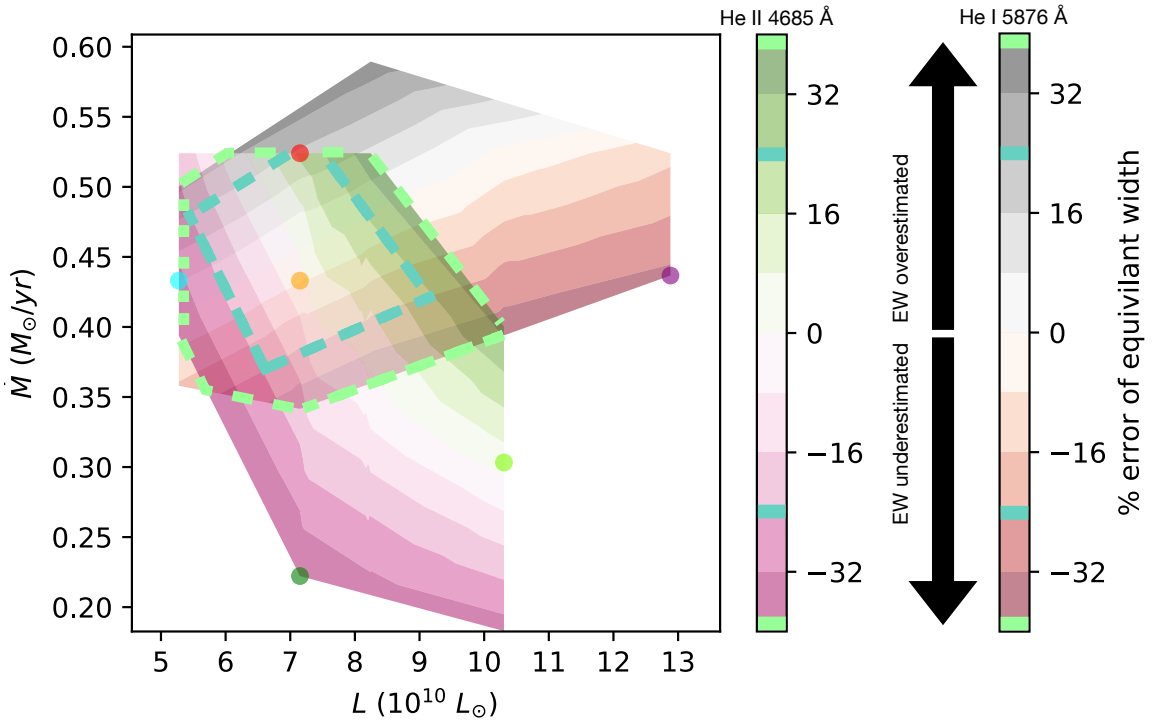

Figure 4.19: Parameter space explored by best-fitting models to the SN 2010al early spectrum. The overlapping colour gradients highlight where the modelled parameter space best reproduces the equivalent widths of He I 5876 Å and He II 4685 Å emission as indicated by the colour bars. Overestimating the line equivalent width results in a positive error, while an underestimation leads to a negative value as indicated by the arrows. The L_{SN} and $\dot{M}$ of the six models displayed in Figures 4.20-4.23 are indicated by the circles matching the colour of their spectra. The grid space corresponding to the upper error thresholds of <24% and <40% adopted in Figure 4.24 are also displayed by the blue and green dashed lines, respectively.

Having scaled our preliminary best-fit models to reproduce the absolute flux spectrum, we are able to constrain the range of L_{SN} and $\dot{M}$ which best reproduce the observation. To achieve this, we slightly vary either the L_{SN} or $\dot{M}$ of the models which best fit the absolute flux spectrum, creating a sub-library of models. To quantify the suitability of each of these models, we utilise the prominent He I 5876 Å and He II 4685 Å emission lines, calculating their equivalent widths in both the modelled spectra and observed spectrum. This allows us to calculate a percentage error for each model's ability to fit these strong lines in the observation. The sub-library of SN 2010al models and their respective fit-errors are displayed in Figure 4.19.

Our CMFGEN models show that variations in both $\dot{M}$ and L_{SN} strongly affect the He I 5876 Å and He II 4685 Å lines. The combination of spectral effects that $\dot{M}$ and L_{SN} have result in an optimal region within Figure 4.19 for simultaneously reproducing the observed lines. The model shown in Figure 4.20 and represented by the orange circle in Figure 4.19 resides within this region, having $\dot{M}$=0.43 $M_{\odot}$yr^{-1}and L_{SN}=7.1 $\times 10^{10} L_{\odot}$. We can see that this model simultaneously fits the EWs of both lines to a satisfactory degree, illustrating that it has the appropriate ionisation and density structure for the CSM. Large variations in either L_{SN} or $\dot{M}$ from these values clearly lower the fit quality as shown in Figures 4.21-4.23, as is now discussed.

Figure 4.21 shows that a variation in $\dot{M}$ affects both the He II 4685 Å (left) and He I 5876 Å (right) lines, with higher values of $\dot{M}$ increasing their EWs, and vice versa. As explained in Section 4.2.3, this is caused by the change in density of the CSM through the mass continuity equation ($\rho \propto \dot{M}$), and the fact that both lines are recombination lines and thus have emissivities approximately proportional to $\rho^2_{\rm CSM}$.

Our models have also indicated that an increase in L_{SN} raises He II 4685 Å and weakens the He I emission, as seen in the purple model in Figure 4.22. This is a result of the changing ionisation fraction of He. A higher temperature profile due to a larger L_{SN} also strengthens the N III emission seen blue-ward of He II 4685 Å. Raising L_{SN} to 1.3 $\times 10^{11} L_{\odot}$ is seen to produce broad emission blue-ward of He I 5876 Å. This broad emission is due to C IV 5801 and 5812 Å, and is absent from the observations.

Figure 4.23 shows an example of a model that fits the EW He II 4685 Å well, but does not reproduce He I 5876 Å. If only He II 4685 Å is observed, then the derived $\dot{M}$ and L_{SN} will be highly degenerate, with large errors up to a factor of 2. This illustrates that it is crucial to observe both lines for determining realistic properties of SN Ibn progenitors at early-times.

We find that setting an allowed upper error threshold of <24% in the equivalent

widths of He I 5876 Å and He II 4685 Å yields a satisfactory fit to the observed spectrum of SN 2010al. Figure 4.24 displays our final best-fit models (within the shaded blue region) which satisfy this, with the absolute and normalised spectra given in the upper and lower panels, respectively. Also shown are models which satisfy a more forgiven threshold of <40% (green shaded region). This figure shows that our best-fit models simultaneously provide satisfactory fits to the observed continuum in addition to the strong emission lines. The displayed line identifications of prominent lines in our models are mostly in agreement with the predicted identifications offered in Pastorello et al. (2015).

We mention above that we predict the colour excess due to the reddening effect to be E(B-V)=0.4 mag for SN 2010al. The best-fit models which satisfy the upper error threshold of <24% (<40%) in the equivalent widths of He I 5876 Å and He II 4685 Å shown in Figure 4.24 predict the following progenitor and SNe properties for SN 2010al: a SN luminosity between 6.2-8.2 (5.3-10) $\times 10^{10}$ $L_{\odot}$, a progenitor mass-loss rate between 0.39-0.52 (0.34-0.52) $M_{\odot}\mathrm{yr}^{-1}$, a wind velocity of 1000 km s^{-1} and an inner boundary radius to the CSM R_{in} of 1.2 $\times 10^{15}$ cm. This R_{in} corresponds to an explosion time of 14 days assuming a typical ejecta velocity for normal SNe of 10^4km s^{-1}. To achieve a modelled time of 5.7 days post-explosion more consistent with the observed spectrum, an ejecta velocity of 2.5 $\times 10^4$ km s^{-1} is required. However, it may be the case that Type-Ibn SNe have higher ejecta velocities compared to non-interacting normal SNe.

In terms of the surface abundances, we obtain a composition of 99% He and $\sim$ 1% N by mass. The N abundance is determined from the N III and N IV lines in the optical spectrum. Our models also allow us to determine the nature of the double-peaked emission component seen at $\sim$ 4660 Å. Pastorello et al. (2015) suggest that the redder peak is He II 4686 Å while the bluer peak likely results from a blend of C III 4648 Å and N III 4640 Å. Our best fit models instead predict the blue peak to result predominantly from a blend of N III 4634, 4641 and 4642 Å. The respective equivalent widths our models predict for these N III lines are factors of 65, 111 and 15 larger than that predicted for C III 4648 Å. We do not see evidence of high C abundance.

The component which appears to be underestimated in the models further blue-ward of the previously discussed blue N III peak likely originates from a blend of He I 4472 Å and He II 4542 Å, both of which are present in the model, albeit insufficiently. Our best fit model also suggests that He II strongly contributes to the emission at 6560 Å offering an alternative to the H-α identification inferred by Pastorello et al. (2015). This would be consistent with the lack of H lines observed and the consequent Ibn classification of SN 2010al.

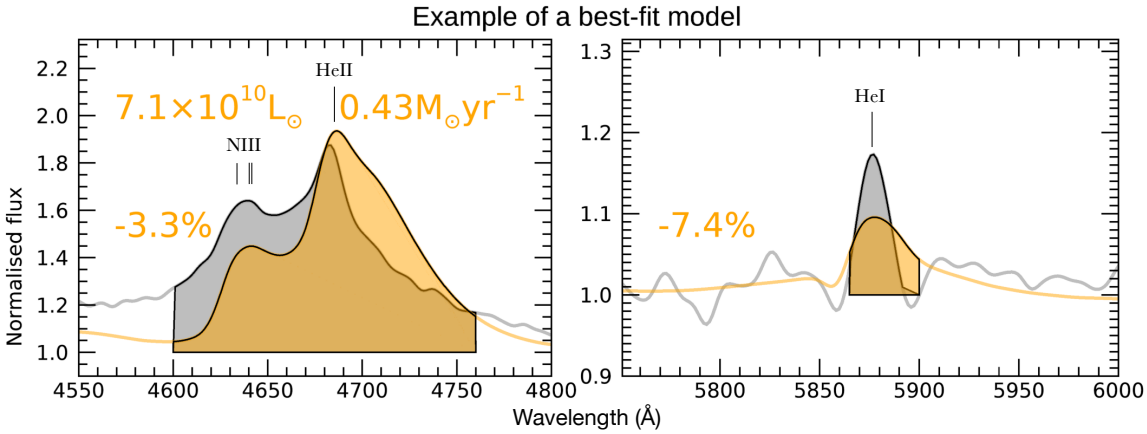

Figure 4.20: A model fit (orange) to the observed spectrum of SN 2010al at 5.7 days post-explosion (grey). The left and right panels display the He II 4685 Å and He I 5876 Å lines, respectively. The shaded areas display the regions from which the equivalent widths were calculated. The error of the model in matching the observation are stated, along with the L_{SN} and $\dot{M}$ of the model. The chosen values of L_{SN} and $\dot{M}$ result in a good fit to these lines. The remaining modelled parameters are as follows: $T_{\star}$=22.7 kK, $T_{\rm eff}$=13.7kK and $R_{\rm in}$=1.2 $\times$ 10^{15} cm.

From analysing the He I line formation region of the SN 2010al best-fit models (in a similar manner to that undertaken in the parameter study of Section 4.2), we find that the formation occurs predominantly at depths between ∼2-3 R_{in} into the CSM. Similar to that done by Gräfener and Vink (2016) for SN 2013cu, we can assume this peak He I formation region to be representative of the outer region of the CSM, allowing us to predict both the time and mass required in forming the CSM. Our models predict a faster wind velocity of 1000 km s^{-1} for SN 2010al compared to the 130 km s^{-1} used for SN 2013cu. This faster wind drastically reduces the time required to expel CSM material out to the ∼2.5 R_{in} radius adopted for the outer region of the CSM, requiring only 0.95 years. Multiplying this time duration by our models' mass-loss rates of 0.39-0.52 $M_{\odot}yr^{-1}$suggests a total mass of 0.37-0.49 $M_{\odot}$ for the CSM. As mentioned by Gräfener and Vink (2016), it is important to note that such predictions offer lower limits for the true mass of the CSM, as it may extend beyond the formation region of He I. Additionally, our models include He I emission, albeit weaker, at distances well beyond the peak region.

Gräfener and Vink (2016) discuss two main effects of LTT for the case of Type-IIb SN 2013cu. Firstly, LTT results in an overall dimmer spectrum, as light received by an observer consists of light which left the nearest point of the CSM to the observer at a given time, combined with light which left more distant regions of the system at earlier (and dimmer) times. This is true so long as the spectrum was taken at a time in which the

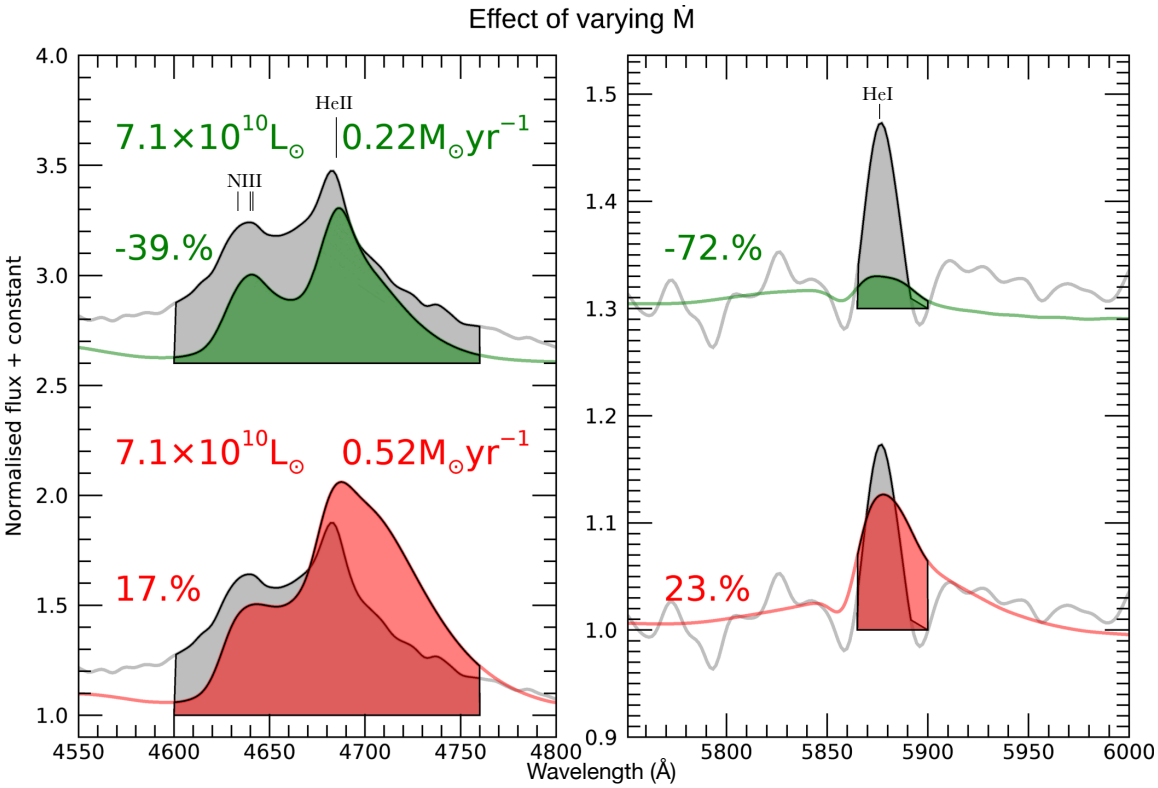

Figure 4.21: Similar to Figure 4.20, only now the models were chosen to demonstrate the effect a variation in $\dot{M}$ has on the line fits. Remaining modelled parameters are as follows for the upper green (lower red) model: $T_{\rm eff}$=17.6 (12.5) kK, matching $T_\star$ and $R_{\rm in}$ of 22.7 kK and 1.2×10^{15} cm, respectively.

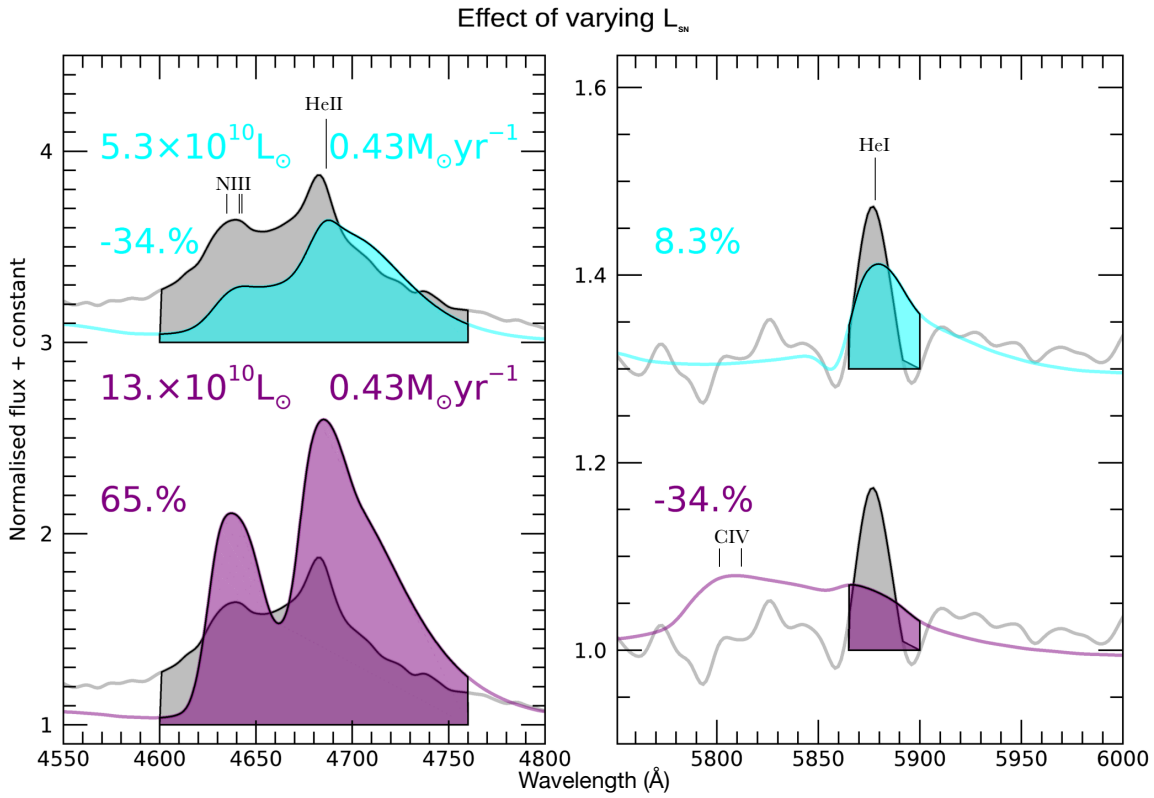

Figure 4.22: Similar to Figure 4.20, only now the models were chosen to demonstrate the effect a variation in L_{SN} has on the line fits. Remaining modelled parameters are as follows for the upper cyan (lower purple) model: $T_\star$=21.0 (26.3) kK, $T_{\rm eff}$=12.6 (13.3) kK and matching $R_{\rm in}$ of 1.2×10^{15} cm.

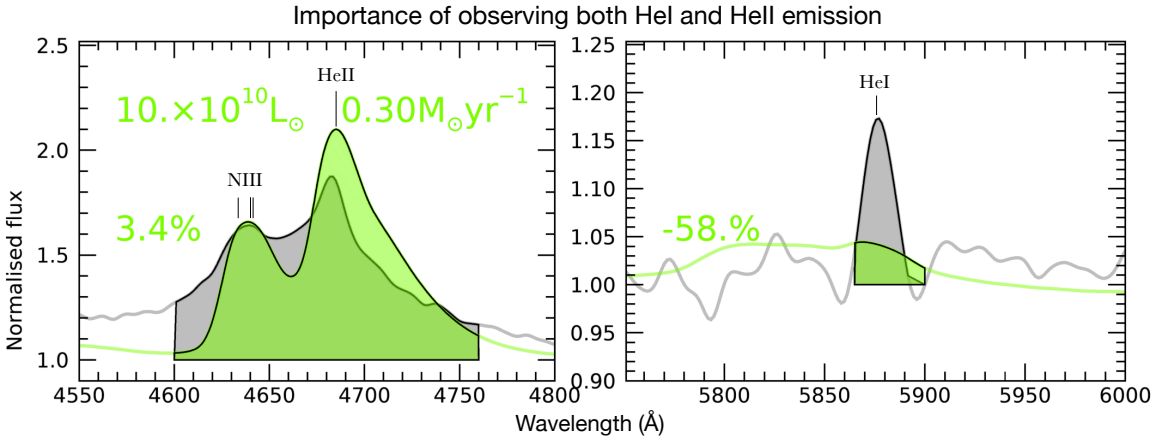

Figure 4.23: Similar to Figure 4.20, only now the model was chosen to demonstrate the importance of simultaneously observing both He I and He II emission in order to constrain L_{SN} and $\dot{M}$. Remaining modelled parameters are as follows: $T_\star$=24.8 kK, $T_{\rm eff}$=15.1 kK and $R_{\rm in}$=1.2×10^{15} cm.

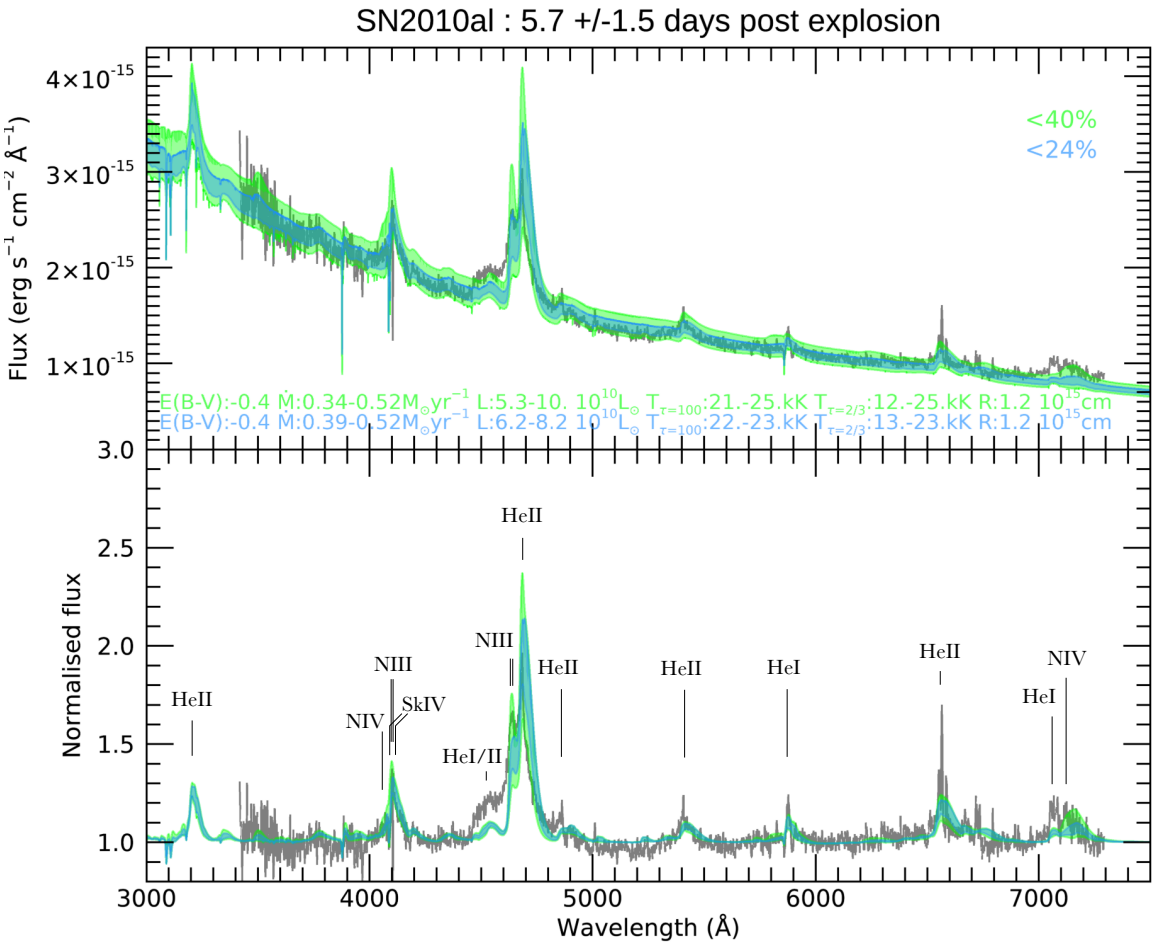

Figure 4.24: Best-fitting models to a spectrum of SN 2010al observed 5.7 days post-explosion (grey). The green (blue) shaded region contains the spectra of all models which achieved an error of <40% (<24%) in the equivalent width of both He I 5876 Å and He II 4685 Å compared to the observation. Upper and lower panels show the spectra in absolute and normalised flux units, respectively. Prominent emission lines in the model are identified by vertical lines in the normalised flux spectrum. Predicted properties of the progenitor and the colour excess are also stated.

light curve was rising, as was the case for the SN 2010al spectrum fitted here. Hence, had our modelling accounted for LTT, it likely would have required slightly greater luminosities in order to reproduce the observed absolute spectrum.

Secondly, the depth at which the formation of a particular spectral line occurs decides the extent at which LTT affects the resulting line profile. LTT weakens the red wing of a spectral line, as this wing is produced by material travelling away from the observer. This light has a greater distance to travel to reach the observer, and accordingly, light reaching the observer and forming the red wing must have left at an earlier (and dimmer) time than that which forms the blue wing. Figure 4.20 reveals that a slight weakening of the red wing of both He I 5876Å and He II 4685Å would indeed aid the fit of our best fit models. Spectral lines which form further into the CSM at cooler temperatures, typically lower ionisation He lines such as He I 5786Å, are more affected by LTT than those which form at shorter depths into the CSM. Utilising Equation 6 of Gräfener and Vink (2016), we demonstrate this by calculating the time delay relative to the closest point to the observer, for light to travel from various points along the formation regions of the He I 5876Å and He II 4685Å lines. The resulting time delays are displayed in Figure 4.25. It was mentioned previously that He I 5786Å formation peaks at $\sim$2.5 R_{in} into the CSM of our SN 2010al models. As would be expected, He II 4685Å peaks at a shorter depth of $\sim 1.6 R_{in}$. As highlighted by Figure 4.25, the greater formation depth of He I renders such lines more susceptible to LTT effects. A relative time delay exceeding 2 days for the more distant He I formation regions emphasises the importance of including LTT effects in future modelling.

Figure 4.26 compares synthetic photometry computed using our $<$40% spectral fit-error models to a wealth of photometric observations. The photometric observing instruments include the space-based Swift satellite and its UltraViolet and Optical Telescope (hereby UVOT, Roming et al., 2005). Impressively, the early 5.7 day spectral observation was obtained before photometric observations began in most of the displayed pass-bands. The earlier light-curves of the I, R, V and non-UVOT B bands suggest that our synthetic photometry is up to a half magnitude lower (brighter) than the observed photometry. As the models provide a good fit to the observed optical spectrum, the slight disagreement between observed and synthetic *optical* photometry likely originates from the observations rather than the models. A slight over-prediction of the flux in the observed spectrum, perhaps originating from instrumental or data reduction errors, could cause this. These errors could alternatively result in the photometric flux appearing lower than its true value. Of course, for wavelengths beyond the narrow

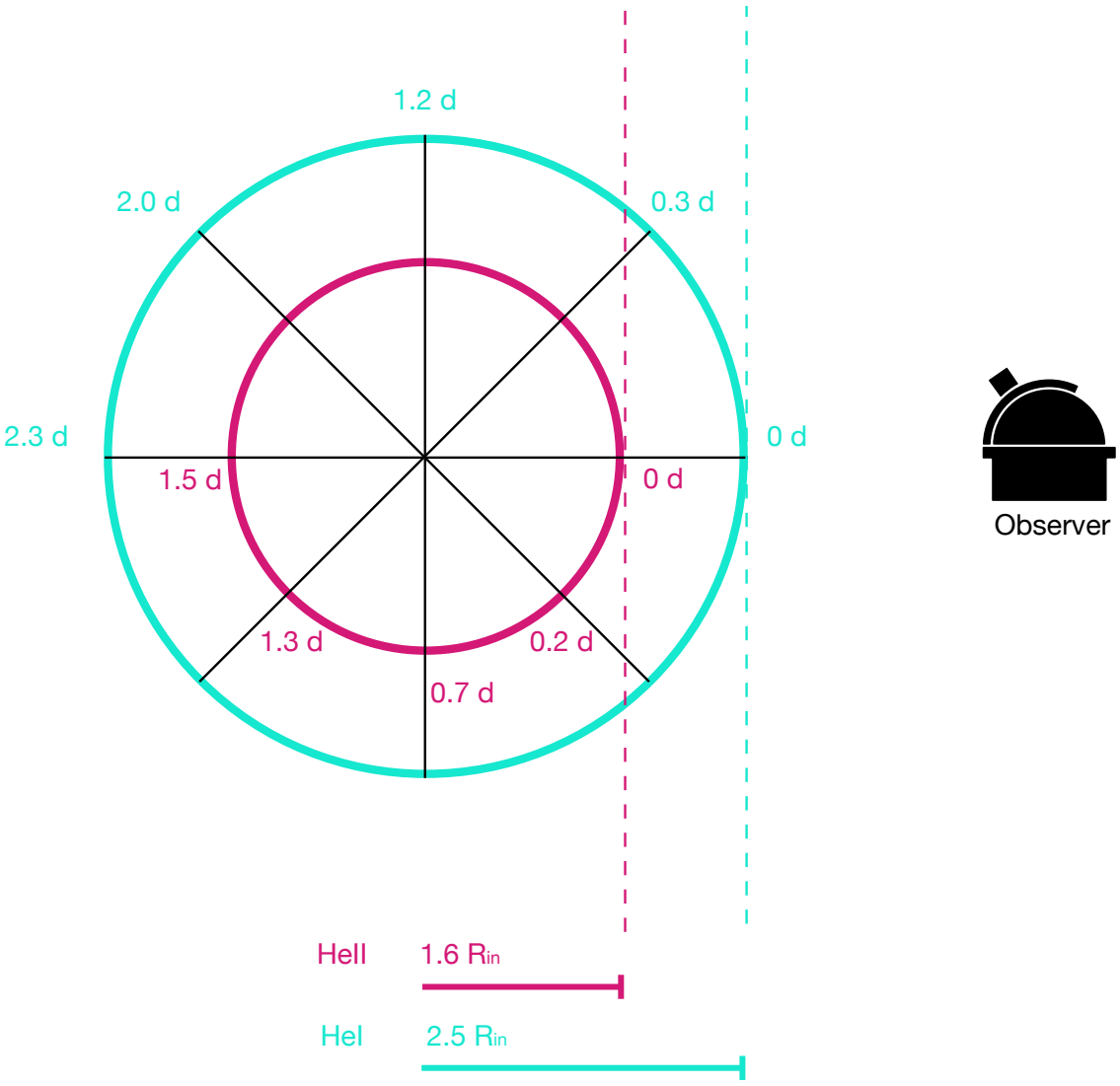

Figure 4.25: The time delay in days relating to where in the CSM of SN 2010al light travels from, relative to the region nearest to the observer. The delays were calculated using Equation 6 of Gräfener and Vink (2016). Distances of 2.5 R_{in} and 1.6 R_{in} were chosen to be representative of the radii at which He I and He II line formation peak, respectively. These radii are based on an analysis of He I 5876Å and He II 4685Å formation in the SN 2010al best-fit models (not shown, but similar to that presented in the parametric study of Section 4.2).

region covered spectroscopically, the modelled spectrum may be a poor representation of the true spectrum, resulting in very large discrepancies between synthetic and observed photometry. Fortunately, this does not seem to be the case in both UV and IR bands, although the earlier observing time of the spectrum and the large magnitude ranges of the synthetic photometry complicate this.

It is particularly clear from the R-band light curve that the spectral observation our models fit was obtained while the light-curve of SN 2010al was still rising. Hence our modelling of SN 2010al may be of particular use to those aiming to observe SN Ibn at early-times, observations which are currently lacking.

Our predicted properties, in particular the H-free and N-rich nature of our models are consistent with the progenitor being H-stripped (probably of WN type), exploding as a Type-I SN surrounded by a dense H-free, He-rich CSM as previously suggested by Pastorello et al. (2015). The mass-loss rates our models need to produce the required CSM density are considerably higher than that of a radiative driven wind which suggests that this CSM was ejected in a major eruption, or perhaps a binary interaction. We can also not rule out the explosion of a small-mass, stripped-envelope star surrounded by a He-rich CSM which could have been ejected by a binary interaction. SN 2010al's location of 9.5" West and 8.1" South from the centre of its host spiral galaxy UGC 4286 (Rich, 2010; Pastorello et al., 2015) favours the higher mass WR scenario, however, such an analysis is complicated by the edge-on orientation of UGC 4286.

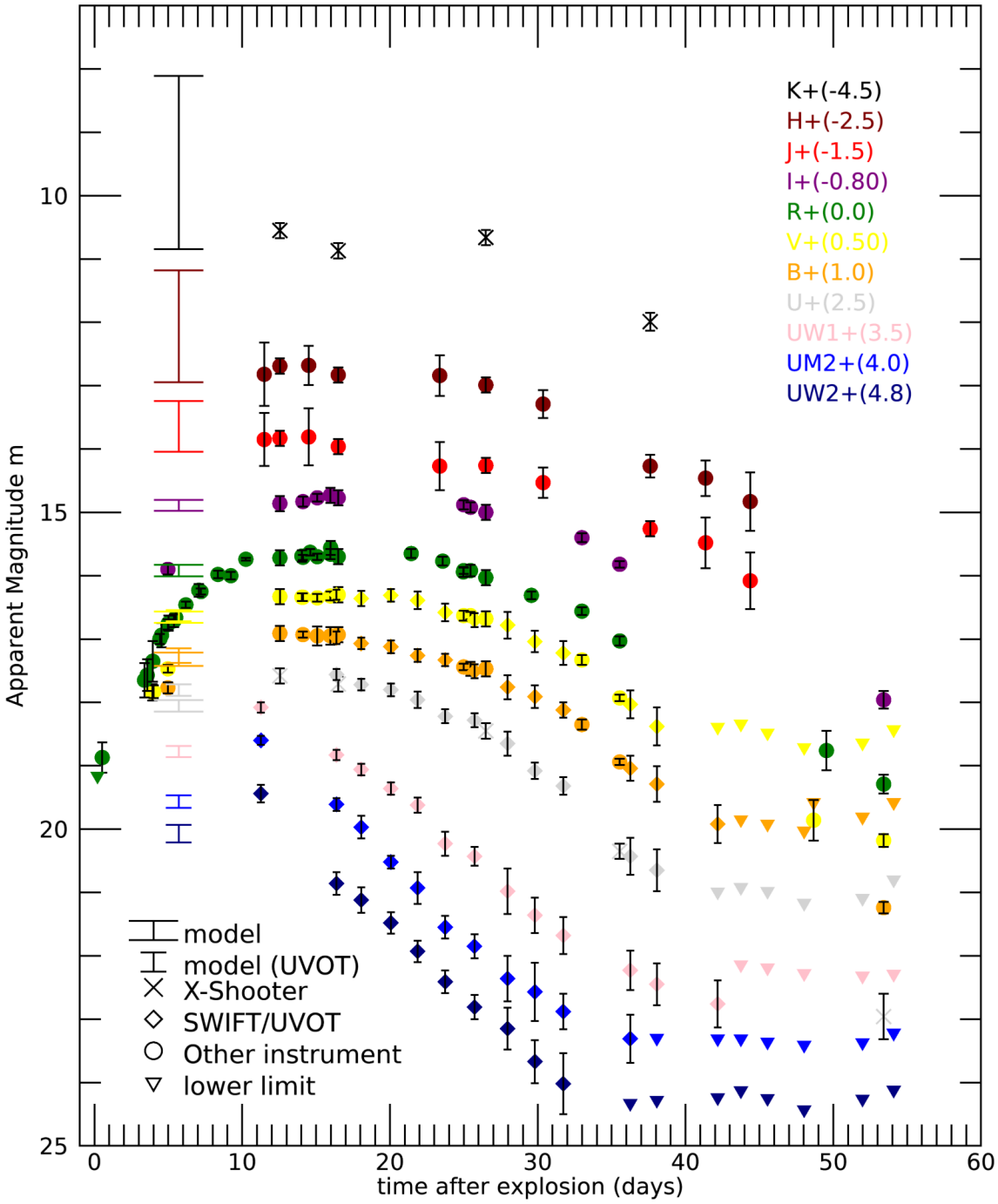

Figure 4.26: Synthetic photometry of SN 2010al compared to observational data obtained from Pastorello et al. (2015). Coloured bars at 5.7 days span the range of magnitudes predicted by our <40% fit-error models to the optical spectrum of SN 2010al. Their capsize distinguishes between modelled fits to standard and Swift UVOT bands. Colour corresponds to the pass-bands displayed previously in Figure 2.3. Remaining symbols indicate the instrument used to obtain the observation or whether it is a lower limit of apparent magnitude due to a non-detection. An arbitrarily offset quoted in the legend has been applied to the apparent magnitude of each pass-band to separate overlapping light-curves and ease visualisation. The full list of instruments which obtained the observational data is given in Tables A3 and A5 of Pastorello et al. (2015).

Chapter 5

A brief outlook into future works

This final chapter offers a brief outlook into the future work of the two studies presented in this thesis. Sections 5.1 and 5.2 cover our studies of PHL 293B and Type-Ibn SNe, respectively.

5.1 Outlook for PHL 293B

The case of PHL 293B is unique in the sense that several spectra were obtained shortly before its disappearance, which show spectral features that are consistent with stellar properties of an LBV in eruption. The low metallicity ($\sim$ 0.1 solar) of PHL 293B further amplifies its importance. It will be highly beneficial to search for similar events in large scale surveys such as the Zwicky Transient Factory (ZTF; Bellm et al., 2019) and the Large Synoptic Survey Telescope (LSST; Ivezic et al., 2008). Given that the majority of such events in deep surveys will be much fainter than PHL 293B and located much farther, a detailed analysis of this object in the local Universe provides an important benchmark for understanding the late-time evolution of massive stars in low metallicity environments and their remnants. Deep high spatial resolution imaging is needed to further discriminate between the different scenarios that have been proposed. Fortunately, our team will get the chance to do so with the Hubble Space Telescope as will be presented in a future paper led by Nathan Smith.

5.2 Outlook for early-time spectra of SNe Ibn

A lack of detailed spectral modelling for Type-Ibns prevents a comparison of the predicted properties with that for other Type-Ibn events. However, numerous studies have predicted progenitor properties for the more common H-rich interacting Type-IIn SNe, with Boian

and Groh (2020) also employing CMFGEN to model their early-time spectroscopy. The L_{SN} and $\dot{M}$ we predict for SN 2010al are within the range of 10^8-10^{12} $L_\odot$ and a few 10^{-4} up to 1.0 $M_\odot \mathrm{yr}^{-1}$ that Boian and Groh (2020) predict for the 17 Type-IIn events that they study. In the future however, early-time detailed spectroscopic modelling of more interacting events, particularly Ibns, will greatly benefit such a comparison.

A similar procedure to that followed in Section 4.3 for SN2010 al could also be applied to early-time observations of more Type-Ibn SNe. With SNe classification techniques constantly improving, more and more spectra of Type-Ibn SNe should be obtained at sufficient time post-explosion and resolution for performing such an analysis. As it stands, SN 2010al remains the best-suited event to our modelling.

Bibliography

Adams, S. M. et al. (July 2017a). "The search for failed supernovae with the Large Binocular Telescope: confirmation of a disappearing star". In: MNRAS 468.4, pp. 4968–4981. DOI: 10.1093/mnras/stx816. arXiv: 1609.01283 [astro-ph.SR].

Adams, S. M. et al. (Aug. 2017b). "The search for failed supernovae with the Large Binocular Telescope: constraints from 7 yr of data". In: MNRAS 469.2, pp. 1445–1455. DOI: 10.1093/mnras/stx898. arXiv: 1610.02402 [astro-ph.SR].

Allan, Andrew P. and Jose H. Groh (2021). "Type Ibn Supernovae - A detailed spectroscopic study using radiative transfer modelling with CMFGEN ". In: *[Manuscript in preparation]*.

Allan, Andrew P. et al. (June 2020). "The possible disappearance of a massive star in the low-metallicity galaxy PHL 293B". In: MNRAS 496.2, pp. 1902–1908. DOI: 10.1093/mnras/staa1629. arXiv: 2003.02242 [astro-ph.SR].

Anderson, Lawrence S. (Apr. 1989). "Line Blanketing without Local Thermodynamic Equilibrium. II. A Solar-Type Model in Radiative Equilibrium". In: ApJ 339, p. 558. DOI: 10.1086/167317.

Basinger, C. M. et al. (July 2020). "The Search for Failed Supernovae with the Large Binocular Telescope: N6946-BH1, Still No Star". In: *arXiv e-prints*, arXiv:2007.15658, arXiv:2007.15658. arXiv: 2007.15658 [astro-ph.SR].

Bellm, Eric C. et al. (Jan. 2019). "The Zwicky Transient Facility: System Overview, Performance, and First Results". In: PASP 131.995, p. 018002. DOI: 10.1088/1538-3873/aaecbe. arXiv: 1902.01932 [astro-ph.IM].

Bilinski, Christopher et al. (Mar. 2018). "SN2012ab: a peculiar Type IIn supernova with aspherical circumstellar material". In: MNRAS 475.1, pp. 1104–1120. DOI: 10.1093/mnras/stx3214. arXiv: 1712.03370 [astro-ph.SR].

Björklund, R. et al. (Apr. 2021). "New predictions for radiation-driven, steady-state mass-loss and wind-momentum from hot, massive stars. II. A grid of O-type stars in the Galaxy and the Magellanic Clouds". In: A&A 648, A36, A36. DOI: 10.1051/0004-6361/202038384. arXiv: 2008.06066 [astro-ph.SR].

Boian, I. and J. H. Groh (2018). "Catching a star before explosion: the luminous blue variable progenitor of SN 2015bh". In: A&A 617, A115, A115. DOI: 10.1051/0004-6361/201731794. arXiv: 1708.05380 [astro-ph.SR].

— (Jan. 2019). "Diversity of supernovae and impostors shortly after explosion". In: A&A 621, A109, A109. DOI: 10.1051/0004-6361/201833779. arXiv: 1811.06505 [astro-ph.SR].

Boian, Ioana and Jose H. Groh (June 2020). "Progenitors of early-time interacting supernovae". In: MNRAS 496.2, pp. 1325–1342. DOI: 10.1093/mnras/staa1540. arXiv: 2001.07651 [astro-ph.SR].

Brown, Thomas M. et al. (Nov. 2002). "Isolating Clusters with Wolf-Rayet Stars in I Zw 18". In: ApJ 579.2, pp. L75–L78. DOI: 10.1086/345336. arXiv: astro-ph/0210089 [astro-ph].

Burke, Colin J. et al. (Feb. 2020). "The Curious Case of PHL 293B: A Long-Lived Transient in a Metal-Poor Blue Compact Dwarf Galaxy". In: *arXiv e-prints*, arXiv:2002.12369, arXiv:2002.12369. arXiv: 2002.12369 [astro-ph.GA].

Busche, Joseph R. and D. John Hillier (2005). "Spectroscopic Effects of Rotation in Extended Stellar Atmospheres". In: AJ 129.1, pp. 454–465. DOI: 10.1086/426362.

Castor, J. I., D. C. Abbott, and R. I. Klein (Jan. 1975). "Radiation-driven winds in Of stars." In: ApJ 195, pp. 157–174. DOI: 10.1086/153315.

Chevalier, Roger A. and Claes Fransson (2017). "Thermal and Non-thermal Emission from Circumstellar Interaction". In: *Handbook of Supernovae*. Ed. by Athem W. Alsabti and Paul Murdin, p. 875. DOI: 10.1007/978-3-319-21846-5_34.

Conti, P. S. (Jan. 1984). "Basic Observational Constraints on the Evolution of Massive Stars". In: *Observational Tests of the Stellar Evolution Theory*. Ed. by A. Maeder and A. Renzini. Vol. 105, p. 233.

Crivellari, Lucio, Sergio Simón-Díaz, and María Jesús Arévalo (2019). *Radiative Transfer in Stellar and Planetary Atmospheres*. DOI: 10.1017/9781108583572.

Crowther, P. A. and L. J. Hadfield (Apr. 2006). "Reduced Wolf-Rayet line luminosities at low metallicity". In: A&A 449.2, pp. 711–722. DOI: 10.1051/0004-6361:20054298. arXiv: astro-ph/0512183 [astro-ph].

Crowther, Paul A. (Sept. 2007). "Physical Properties of Wolf-Rayet Stars". In: ARA&A 45.1, pp. 177–219. DOI: 10.1146/annurev.astro.45.051806.110615. arXiv: astro-ph/0610356 [astro-ph].

Davidson, Kris (Feb. 2020). "Radiation-Driven Stellar Eruptions". In: *Galaxies* 8.1, p. 10. DOI: 10.3390/galaxies8010010. arXiv: 2009.02340 [astro-ph.SR].

de Groot, Mart (Mar. 1988). "The most luminous stars in the universe". In: *Irish Astronomical Journal* 18, pp. 163–170.

de Jager, C., H. Nieuwenhuijzen, and K. A. van der Hucht (Feb. 1988). "Mass loss rates in the Hertzsprung-Russell diagram." In: A&AS 72, pp. 259–289.

Dekker, Hans et al. (Aug. 2000). "Design, construction, and performance of UVES, the echelle spectrograph for the UT2 Kueyen Telescope at the ESO Paranal Observatory". In: *Optical and IR Telescope Instrumentation and Detectors*. Ed. by Masanori Iye and Alan F. Moorwood. Vol. 4008. Society of Photo-Optical Instrumentation Engineers (SPIE) Conference Series, pp. 534–545. DOI: 10.1117/12.395512.

Dessart, Luc, Edouard Audit, and D. John Hillier (June 2015). "Numerical simulations of superluminous supernovae of type IIn". In: MNRAS 449.4, pp. 4304–4325. DOI: 10.1093/mnras/stv609. arXiv: 1503.05463 [astro-ph.SR].

Dolphin, Andrew (Aug. 2016). *DOLPHOT: Stellar photometry*. ascl: 1608.013.

Dolphin, Andrew E. (Oct. 2000). "WFPC2 Stellar Photometry with HSTPHOT". In: PASP 112.776, pp. 1383–1396. DOI: 10.1086/316630. arXiv: astro-ph/0006217 [astro-ph].

Ekström, S. et al. (Jan. 2012). "Grids of stellar models with rotation. I. Models from 0.8 to 120 $M_{M_\odot}$ at solar metallicity (Z = 0.014)". In: A&A 537, A146, A146. DOI: 10.1051/0004-6361/201117751. arXiv: 1110.5049 [astro-ph.SR].

Fabricant, Daniel et al. (Jan. 1998). "The FAST Spectrograph for the Tillinghast Telescope". In: PASP 110.743, pp. 79–85. DOI: 10.1086/316111.

Fitzpatrick, Edward L. (Jan. 1999). "Correcting for the Effects of Interstellar Extinction". In: PASP 111.755, pp. 63–75. DOI: 10.1086/316293. arXiv: astro-ph/9809387 [astro-ph].

Foley, R. J. et al. (May 2011). "The Diversity of Massive Star Outbursts. I. Observations of SN2009ip, UGC 2773 OT2009-1, and Their Progenitors". In: ApJ 732, 32, p. 32. DOI: 10.1088/0004-637X/732/1/32. arXiv: 1002.0635 [astro-ph.SR].

Foley, Ryan J. et al. (Mar. 2007). "SN 2006jc: A Wolf-Rayet Star Exploding in a Dense He-rich Circumstellar Medium". In: ApJ 657.2, pp. L105–L108. DOI: 10.1086/513145. arXiv: astro-ph/0612711 [astro-ph].

Gal-Yam, A. and D. C. Leonard (Apr. 2009). "A massive hypergiant star as the progenitor of the supernova SN 2005gl". In: Nature 458.7240, pp. 865–867. DOI: 10.1038/nature07934.

Georgy, C. et al. (2013). "Grids of stellar models with rotation. III. Models from 0.8 to 120 $M_{\odot}$at a metallicity Z = 0.002". In: A&A 558, A103, A103. DOI: 10.1051/0004-6361/201322178. arXiv: 1308.2914 [astro-ph.SR].

Gormaz-Matamala, Alex C. et al. (Mar. 2019). "Self-consistent Solutions for Line-driven Winds of Hot Massive Stars: The m-CAK Procedure". In: ApJ 873.2, 131, p. 131. DOI: 10.3847/1538-4357/ab05c4. arXiv: 1903.00417 [astro-ph.SR].

Gräfener, G. and J. S. Vink (Jan. 2016). "Light-travel-time diagnostics in early supernova spectra: substantial mass-loss of the IIb progenitor of SN 2013cu through a superwind". In: MNRAS 455.1, pp. 112–126. DOI: 10.1093/mnras/stv2283. arXiv: 1510.00013 [astro-ph.SR].

Grassitelli, L. et al. (Mar. 2021). "Wind-envelope interaction as the origin of the slow cyclic brightness variations of luminous blue variables". In: A&A 647, A99, A99. DOI: 10.1051/0004-6361/202038298. arXiv: 2012.00023 [astro-ph.SR].

Groh, J. H., G. Meynet, and S. Ekström (Feb. 2013). "Massive star evolution: luminous blue variables as unexpected supernova progenitors". In: A&A 550, L7, p. L7. DOI: 10.1051/0004-6361/201220741. arXiv: 1301.1519 [astro-ph.SR].

Groh, J. H. et al. (June 2009). "On the Nature of the Prototype Luminous Blue Variable Ag Carinae. I. Fundamental Parameters During Visual Minimum Phases and Changes in the Bolometric Luminosity During the S-Dor Cycle". In: ApJ 698.2, pp. 1698–1720. DOI: 10.1088/0004-637X/698/2/1698. arXiv: 0904.2363 [astro-ph.SR].

Groh, J. H. et al. (2019). "Grids of stellar models with rotation. IV. Models from 1.7 to 120 M at a metallicity Z = 0.0004". In: A&A 627, A24, A24. DOI: 10.1051/0004-6361/201833720. arXiv: 1904.04009 [astro-ph.SR].

Groh, Jose H. (Dec. 2014). "Early-time spectra of supernovae and their precursor winds. The luminous blue variable/yellow hypergiant progenitor of SN 2013cu". In: A&A 572, L11, p. L11. DOI: 10.1051/0004-6361/201424852. arXiv: 1408.5397 [astro-ph.HE].

Groh, Jose H. et al. (June 2012a). "On the influence of the companion star in Eta Carinae: 2D radiative transfer modelling of the ultraviolet and optical spectra". In: MNRAS 423.2, pp. 1623–1640. DOI: 10.1111/j.1365-2966.2012.20984.x. arXiv: 1204.1963 [astro-ph.SR].

— (June 2012b). "On the influence of the companion star in Eta Carinae: 2D radiative transfer modelling of the ultraviolet and optical spectra". In: MNRAS 423.2, pp. 1623–1640. DOI: 10.1111/j.1365-2966.2012.20984.x. arXiv: 1204.1963 [astro-ph.SR].

Groh, Jose H. et al. (Apr. 2014). "The evolution of massive stars and their spectra. I. A non-rotating 60 $M_{\odot}$star from the zero-age main sequence to the pre-supernova stage". In: A&A 564, A30, A30. DOI: 10.1051/0004-6361/201322573. arXiv: 1401.7322 [astro-ph.SR].

Guillochon, James et al. (Jan. 2017). "An Open Catalog for Supernova Data". In: ApJ 835.1, 64, p. 64. DOI: 10.3847/1538-4357/835/1/64. arXiv: 1605.01054 [astro-ph.SR].

Heger, A. et al. (July 2003). "How Massive Single Stars End Their Life". In: ApJ 591.1, pp. 288–300. DOI: 10.1086/375341. arXiv: astro-ph/0212469 [astro-ph].

Higgins, Erin R. et al. (May 2021). "Evolution of Wolf-Rayet stars as black hole progenitors". In: *arXiv e-prints*, arXiv:2105.12139, arXiv:2105.12139. arXiv: 2105.12139 [astro-ph.SR].

Hillier, D. J. (July 1991). "The effects of electron scattering and wind clumping for early emission line stars." In: A&A 247, p. 455.

Hillier, D. John and D. L. Miller (1998). "The Treatment of Non-LTE Line Blanketing in Spherically Expanding Outflows". In: ApJ 496.1, pp. 407–427. DOI: 10.1086/305350.

Hillier, D. John et al. (June 2001). "On the Nature of the Central Source in η Carinae". In: ApJ 553.2, pp. 837–860. DOI: 10.1086/320948.

Hillier, D. John et al. (May 2006). "The UV Scattering Halo of the Central Source Associated with η Carinae". In: ApJ 642.2, pp. 1098–1116. DOI: 10.1086/501225. arXiv: astro-ph/0601686 [astro-ph].

Hosseinzadeh, Griffin et al. (Feb. 2017). "Type Ibn Supernovae Show Photometric Homogeneity and Spectral Diversity at Maximum Light". In: ApJ 836.2, 158, p. 158. DOI: 10.3847/1538-4357/836/2/158. arXiv: 1608.01998 [astro-ph.HE].

Hosseinzadeh, Griffin et al. (Jan. 2019). "Type Ibn Supernovae May not all Come from Massive Stars". In: ApJ 871.1, L9, p. L9. DOI: 10.3847/2041-8213/aafc61. arXiv: 1901.03332 [astro-ph.HE].

Humphreys, Roberta M. and Kris Davidson (1994). "The luminous blue variables: Astrophysical geysers". In: *Publications of the Astronomical Society of the Pacific* 106, p. 1025. DOI: 10.1086/133478. URL: https://doi.org/10.1086/133478.

Humphreys, Roberta M. and Kris Davidson (Oct. 1994). "The Luminous Blue Variables: Astrophysical Geysers". In: PASP 106, p. 1025. DOI: 10.1086/133478.

Humphreys, Roberta M., Kris Davidson, and Nathan Smith (1999). "Eta Carinae's Second Eruption and the Light Curves of the Eta Carinae Variables". In: *Publications of the*

Astronomical Society of the Pacific 111.763, pp. 1124–1131. DOI: 10.1086/316420. URL: https://doi.org/10.1086/316420.

Iglesias, Carlos A. and Forrest J. Rogers (June 1996). "Updated Opal Opacities". In: ApJ 464, p. 943. DOI: 10.1086/177381.

Ivezic, Z. et al. (June 2008). "Large Synoptic Survey Telescope: From Science Drivers To Reference Design". In: *Serbian Astronomical Journal* 176, pp. 1–13. DOI: 10.2298/SAJ0876001I.

Izotov, Y. I. et al. (2011). "VLT/X-shooter observations of the low-metallicity blue compact dwarf galaxy PHL 293B including a luminous blue variable star". In: A&A 533, A25, A25. DOI: 10.1051/0004-6361/201016296. arXiv: 1108.4309 [astro-ph.CO].

Izotov, Yuri I. and Trinh X. Thuan (2009). "Luminous Blue Variable Stars in the two Extremely Metal-Deficient Blue Compact Dwarf Galaxies DDO 68 and PHL 293B". In: ApJ 690.2, pp. 1797–1806. DOI: 10.1088/0004-637X/690/2/1797. arXiv: 0809.3077 [astro-ph].

Izotov, Yuri I., Trinh X. Thuan, and Grażyna Stasińska (2007). "The Primordial Abundance of ^{4}He: A Self-consistent Empirical Analysis of Systematic Effects in a Large Sample of Low-Metallicity H II Regions". In: ApJ 662.1, pp. 15–38. DOI: 10.1086/513601. arXiv: astro-ph/0702072 [astro-ph].

Izotov, Yuri I. et al. (Sept. 1997). "I Zw 18: A New Wolf-Rayet Galaxy". In: ApJ 487.1, pp. L37–L40. DOI: 10.1086/310872. arXiv: astro-ph/9707272 [astro-ph].

Kilpatrick, Charles D. et al. (Feb. 2018). "Connecting the progenitors, pre-explosion variability and giant outbursts of luminous blue variables with Gaia16cfr". In: MNRAS 473.4, pp. 4805–4823. DOI: 10.1093/mnras/stx2675. arXiv: 1706.09962 [astro-ph.SR].

Kotak, R. and J. S. Vink (Dec. 2006). "Luminous blue variables as the progenitors of supernovae with quasi-periodic radio modulations". In: A&A 460.2, pp. L5–L8. DOI: 10.1051/0004-6361:20065800. arXiv: astro-ph/0610095 [astro-ph].

Lamers, Henny J. G. L. M. and Joseph P. Cassinelli (1999). *Introduction to Stellar Winds*.

Lamers, Henny J. G. L. M., Theodore P. Snow, and Douglas M. Lindholm (Dec. 1995). "Terminal Velocities and the Bistability of Stellar Winds". In: ApJ 455, p. 269. DOI: 10.1086/176575.

Legrand, F. et al. (Oct. 1997). "Detection of WR stars in the metal-poor starburst galaxy IZw 18." In: A&A 326, pp. L17–L20. arXiv: astro-ph/9707279 [astro-ph].

Leonard, Douglas C. et al. (June 2000). "Evidence for Asphericity in the Type IIN Supernova SN 1998S". In: ApJ 536.1, pp. 239–254. DOI: 10.1086/308910. arXiv: astro-ph/9908040 [astro-ph].

Lovegrove, Elizabeth and S. E. Woosley (June 2013). "Very Low Energy Supernovae from Neutrino Mass Loss". In: ApJ 769.2, 109, p. 109. DOI: 10.1088/0004-637X/769/2/109. arXiv: 1303.5055 [astro-ph.HE].

Maeder, André and Georges Meynet (Jan. 2000). "The Evolution of Rotating Stars". In: ARA&A 38, pp. 143–190. DOI: 10.1146/annurev.astro.38.1.143. arXiv: astro-ph/0004204 [astro-ph].

Mapelli, Michela (June 2021). "Formation channels of single and binary stellar-mass black holes". In: *arXiv e-prints*, arXiv:2106.00699, arXiv:2106.00699. arXiv: 2106.00699 [astro-ph.HE].

Massey, Philip, K. A. G. Olsen, and J. Wm. Parker (Nov. 2003). "The Discovery of a 12th Wolf-Rayet Star in the Small Magellanic Cloud". In: PASP 115.813, pp. 1265–1268. DOI: 10.1086/379024. arXiv: astro-ph/0308237 [astro-ph].

Massey, Philip et al. (June 2014). "A Modern Search for Wolf-Rayet Stars in the Magellanic Clouds: First Results". In: ApJ 788.1, 83, p. 83. DOI: 10.1088/0004-637X/788/1/83. arXiv: 1404.7441 [astro-ph.SR].

Matheson, Thomas et al. (Mar. 2001). "Optical Spectroscopy of Type IB/C Supernovae". In: AJ 121.3, pp. 1648–1675. DOI: 10.1086/319390. arXiv: astro-ph/0101119 [astro-ph].

Meynet, G. and A. Maeder (Jan. 2005). "Stellar evolution with rotation. XI. Wolf-Rayet star populations at different metallicities". In: A&A 429, pp. 581–598. DOI: 10.1051/0004-6361:20047106. arXiv: astro-ph/0408319 [astro-ph].

Moriya, Takashi J., Elena I. Sorokina, and Roger A. Chevalier (Mar. 2018). "Superluminous Supernovae". In: Space Sci. Rev. 214.2, 59, p. 59. DOI: 10.1007/s11214-018-0493-6. arXiv: 1803.01875 [astro-ph.HE].

Mould, Jeremy R. et al. (2000). "The Hubble Space Telescope Key Project on the Extragalactic Distance Scale. XXVIII. Combining the Constraints on the Hubble Constant". In: ApJ 529.2, pp. 786–794. DOI: 10.1086/308304. arXiv: astro-ph/9909260 [astro-ph].

Neugent, Kathryn F., Philip Massey, and Nidia Morrell (Aug. 2018). "A Modern Search for Wolf-Rayet Stars in the Magellanic Clouds. IV. A Final Census". In: ApJ 863.2, 181, p. 181. DOI: 10.3847/1538-4357/aad17d. arXiv: 1807.01209 [astro-ph.SR].

Neustadt, J. M. M. et al. (Apr. 2021). "The search for failed supernovae with the Large Binocular Telescope: a new candidate and the failed SN fraction with 11 yr of data". In: *arXiv e-prints*, arXiv:2104.03318, arXiv:2104.03318. arXiv: 2104.03318 [astro-ph.SR].

Nugis, T. and H. J. G. L. M. Lamers (Aug. 2000). "Mass-loss rates of Wolf-Rayet stars as a function of stellar parameters". In: A&A 360, pp. 227–244.

O'Connor, Evan and Christian D. Ott (Apr. 2011). "Black Hole Formation in Failing Core-Collapse Supernovae". In: ApJ 730.2, 70, p. 70. DOI: 10.1088/0004-637X/730/2/70. arXiv: 1010.5550 [astro-ph.HE].

Ofek, E. O. et al. (Apr. 2007). "SN 2006gy: An Extremely Luminous Supernova in the Galaxy NGC 1260". In: ApJ 659.1, pp. L13–L16. DOI: 10.1086/516749. arXiv: astro-ph/0612408 [astro-ph].

Ofek, Eran O. et al. (July 2014). "Precursors Prior to Type IIn Supernova Explosions are Common: Precursor Rates, Properties, and Correlations". In: ApJ 789.2, 104, p. 104. DOI: 10.1088/0004-637X/789/2/104. arXiv: 1401.5468 [astro-ph.HE].

Owocki, Stanley P., Kenneth G. Gayley, and Nir J. Shaviv (Nov. 2004). "A Porosity-Length Formalism for Photon-Tiring-limited Mass Loss from Stars above the Eddington Limit". In: ApJ 616.1, pp. 525–541. DOI: 10.1086/424910. arXiv: astro-ph/0409573 [astro-ph].

Pastorello, A. et al. (June 2007). "A giant outburst two years before the core-collapse of a massive star". In: Nature 447.7146, pp. 829–832. DOI: 10.1038/nature05825. arXiv: astro-ph/0703663 [astro-ph].

Pastorello, A. et al. (Sept. 2008). "Massive stars exploding in a He-rich circumstellar medium - II. The transitional case of SN 2005la". In: MNRAS 389.1, pp. 131–140. DOI: 10.1111/j.1365-2966.2008.13603.x. arXiv: 0801.2278 [astro-ph].

Pastorello, A. et al. (May 2015). "Massive stars exploding in a He-rich circumstellar medium - IV. Transitional Type Ibn supernovae". In: MNRAS 449.2, pp. 1921–1940. DOI: 10.1093/mnras/stu2745. arXiv: 1502.04946 [astro-ph.SR].

Pepe, F. et al. (Jan. 2021). "ESPRESSO at VLT. On-sky performance and first results". In: A&A 645, A96, A96. DOI: 10.1051/0004-6361/202038306. arXiv: 2010.00316 [astro-ph.IM].

Petrov, Blagovest, Jorick S. Vink, and Götz Gräfener (May 2016). "Two bi-stability jumps in theoretical wind models for massive stars and the implications for luminous blue variable supernovae". In: MNRAS 458.2, pp. 1999–2011. DOI: 10.1093/mnras/stw382. arXiv: 1602.05868 [astro-ph.SR].

Puls, Joachim, Jorick S. Vink, and Francisco Najarro (Dec. 2008). "Mass loss from hot massive stars". In: A&A Rev. 16.3-4, pp. 209–325. DOI: 10.1007/s00159-008-0015-8. arXiv: 0811.0487 [astro-ph].

Reynolds, Thomas M., Morgan Fraser, and Gerard Gilmore (Nov. 2015). "Gone without a bang: an archival HST survey for disappearing massive stars". In: MNRAS 453.3, pp. 2885–2900. DOI: 10.1093/mnras/stv1809. arXiv: 1507.05823 [astro-ph.SR].

Rich, D. (Mar. 2010). "Supernova 2010al in UGC 4286". In: *Central Bureau Electronic Telegrams* 2207, p. 1.

Roming, Peter W. A. et al. (Oct. 2005). "The Swift Ultra-Violet/Optical Telescope". In: Space Sci. Rev. 120.3-4, pp. 95–142. DOI: 10.1007/s11214-005-5095-4. arXiv: astro-ph/0507413 [astro-ph].

Rutten, Robert J. (2003). *Radiative Transfer in Stellar Atmospheres*.

Rybicki, George B. and Alan P. Lightman (1986). *Radiative Processes in Astrophysics*.

Salpeter, Edwin E. (Jan. 1955). "The Luminosity Function and Stellar Evolution." In: ApJ 121, p. 161. DOI: 10.1086/145971.

Sander, Andreas A. C. and Jorick S. Vink (Nov. 2020). "On the nature of massive helium star winds and Wolf-Rayet-type mass-loss". In: MNRAS 499.1, pp. 873–892. DOI: 10.1093/mnras/staa2712. arXiv: 2009.01849 [astro-ph.SR].

Sanders, N. E. et al. (May 2013). "PS1-12sk is a Peculiar Supernova from a He-rich Progenitor System in a Brightest Cluster Galaxy Environment". In: ApJ 769.1, 39, p. 39. DOI: 10.1088/0004-637X/769/1/39. arXiv: 1303.1818 [astro-ph.CO].

Schlegel, Eric M. (May 1990). "A new subclass of type II supernovae ?" In: MNRAS 244, pp. 269–271.

Shenar, T. et al. (Feb. 2020). "Why binary interaction does not necessarily dominate the formation of Wolf-Rayet stars at low metallicity". In: A&A 634, A79, A79. DOI: 10.1051/0004-6361/201936948. arXiv: 2001.04476 [astro-ph.SR].

Smith, F. and J. Dudley (Jan. 1982). "The Isaac-Newton Telescope". In: *Journal for the History of Astronomy* 13, p. 1. DOI: 10.1177/002182868201300101.

Smith, Nathan (Sept. 2008). "A blast wave from the 1843 eruption of η Carinae". In: Nature 455.7210, pp. 201–203. DOI: 10.1038/nature07269. arXiv: 0809.1678 [astro-ph].

— (Mar. 2013). "A model for the 19th century eruption of Eta Carinae: CSM interaction like a scaled-down Type IIn Supernova". In: MNRAS 429.3, pp. 2366–2379. DOI: 10.1093/mnras/sts508. arXiv: 1209.6155 [astro-ph.SR].

Smith, Nathan (Aug. 2014). "Mass Loss: Its Effect on the Evolution and Fate of High-Mass Stars". In: ARA&A 52, pp. 487–528. DOI: 10.1146/annurev-astro-081913-040025. arXiv: 1402.1237 [astro-ph.SR].

— (2017a). "Interacting Supernovae: Types IIn and Ibn". In: *Handbook of Supernovae*. Ed. by Athem W. Alsabti and Paul Murdin, p. 403. DOI: 10.1007/978-3-319-21846-5_38.

— (Sept. 2017b). "Luminous blue variables and the fates of very massive stars". In: *Philosophical Transactions of the Royal Society of London Series A* 375.2105, 20160268, p. 20160268. DOI: 10.1098/rsta.2016.0268.

Smith, Nathan, Kenneth H. Hinkle, and Nils Ryde (2009). "Red Supergiants as Potential Type IIn Supernova Progenitors: Spatially Resolved 4.6 μm CO Emission Around VY CMa and Betelgeuse". In: AJ 137.3, pp. 3558–3573. DOI: 10.1088/0004-6256/137/3/3558. arXiv: 0811.3037 [astro-ph].

Smith, Nathan, Jon C. Mauerhan, and Jose L. Prieto (Feb. 2014). "SN 2009ip and SN 2010mc: core-collapse Type IIn supernovae arising from blue supergiants". In: MNRAS 438.2, pp. 1191–1207. DOI: 10.1093/mnras/stt2269. arXiv: 1308.0112 [astro-ph.SR].

Smith, Nathan and Stanley P. Owocki (July 2006). "On the Role of Continuum-driven Eruptions in the Evolution of Very Massive Stars and Population III Stars". In: ApJ 645.1, pp. L45–L48. DOI: 10.1086/506523. arXiv: astro-ph/0606174 [astro-ph].

Smith, Nathan and Ryan Tombleson (Feb. 2015). "Luminous blue variables are antisocial: their isolation implies that they are kicked mass gainers in binary evolution". In: MNRAS 447.1, pp. 598–617. DOI: 10.1093/mnras/stu2430. arXiv: 1406.7431 [astro-ph.SR].

Smith, Nathan, Jorick S. Vink, and Alex de Koter (2004). "The Missing Luminous Blue Variables and the Bistability Jump". In: *The Astrophysical Journal* 615.1, pp. 475–484. DOI: 10.1086/424030. URL: https://doi.org/10.1086/424030.

Smith, Nathan et al. (Apr. 2010). "Discovery of Precursor Luminous Blue Variable Outbursts in Two Recent Optical Transients: The Fitfully Variable Missing Links UGC 2773-OT and SN 2009ip". In: AJ 139.4, pp. 1451–1467. DOI: 10.1088/0004-6256/139/4/1451. arXiv: 0909.4792 [astro-ph.SR].

Smith, Nathan et al. (May 2011a). "A Massive Progenitor of the Luminous Type IIn Supernova 2010jl". In: ApJ 732.2, 63, p. 63. DOI: 10.1088/0004-637X/732/2/63. arXiv: 1011.4150 [astro-ph.SR].

Smith, Nathan et al. (2011b). "Luminous blue variable eruptions and related transients: diversity of progenitors and outburst properties". In: MNRAS 415.1, pp. 773–810. DOI: 10.1111/j.1365-2966.2011.18763.x. arXiv: 1010.3718 [astro-ph.SR].

Smith, Nathan et al. (Nov. 2012). "SN 2011hw: helium-rich circumstellar gas and the luminous blue variable to Wolf-Rayet transition in supernova progenitors". In: MNRAS 426.3, pp. 1905–1915. DOI: 10.1111/j.1365-2966.2012.21849.x. arXiv: 1204.0043 [astro-ph.SR].

Smith, Nathan et al. (May 2015). "PTF11iqb: cool supergiant mass-loss that bridges the gap between Type IIn and normal supernovae". In: MNRAS 449.2, pp. 1876–1896. DOI: 10.1093/mnras/stv354. arXiv: 1501.02820 [astro-ph.HE].

Smith, Nathan et al. (2019). "On the Gaia DR2 distances for Galactic luminous blue variables". In: MNRAS 488.2, pp. 1760–1778. DOI: 10.1093/mnras/stz1712. arXiv: 1805.03298 [astro-ph.SR].

Sobolev, V. V. (1960). *Moving envelopes of stars*.

Stoll, R. et al. (Mar. 2011). "SN 2010jl in UGC 5189: Yet Another Luminous Type IIn Supernova in a Metal-poor Galaxy". In: ApJ 730.1, 34, p. 34. DOI: 10.1088/0004-637X/730/1/34. arXiv: 1012.3461 [astro-ph.CO].

Sukhbold, Tuguldur et al. (Apr. 2016). "Core-collapse Supernovae from 9 to 120 Solar Masses Based on Neutrino-powered Explosions". In: ApJ 821.1, 38, p. 38. DOI: 10.3847/0004-637X/821/1/38. arXiv: 1510.04643 [astro-ph.HE].

Sundqvist, J. O. et al. (Dec. 2019). "New predictions for radiation-driven, steady-state mass-loss and wind-momentum from hot, massive stars. I. Method and first results". In: A&A 632, A126, A126. DOI: 10.1051/0004-6361/201936580. arXiv: 1910.06586 [astro-ph.SR].

Terlevich, Roberto et al. (2014). "High-velocity blueshifted Fe II absorption in the dwarf star-forming galaxy PHL 293B: evidence for a wind driven supershell?" In: MNRAS 445.2, pp. 1449–1461. DOI: 10.1093/mnras/stu1806. arXiv: 1409.1189 [astro-ph.GA].

Thöne, C. C. et al. (Mar. 2017). "SN 2015bh: NGC 2770's 4th supernova or a luminous blue variable on its way to a Wolf-Rayet star?" In: A&A 599, A129, A129. DOI: 10.1051/0004-6361/201629968. arXiv: 1606.09025 [astro-ph.HE].

van Genderen, A. M. (Feb. 2001). "S Doradus variables in the Galaxy and the Magellanic Clouds". In: A&A 366, pp. 508–531. DOI: 10.1051/0004-6361:20000022.

van Genderen, A. M., M. de Groot, and C. Sterken (Sept. 1997). "New perceptions on the S Doradus phenomenon and the micro variations of five Luminous Blue Variables (LBVs)". In: A&AS 124, pp. 517–531. DOI: 10.1051/aas:1997204.

Vernet, J. et al. (Dec. 2011). "X-shooter, the new wide band intermediate resolution spectrograph at the ESO Very Large Telescope". In: A&A 536, A105, A105. DOI: 10.1051/0004-6361/201117752. arXiv: 1110.1944 [astro-ph.IM].

Vink, J. S., A. de Koter, and H. J. G. L. M. Lamers (Oct. 1999). "On the nature of the bi-stability jump in the winds of early-type supergiants". In: A&A 350, pp. 181–196. arXiv: astro-ph/9908196 [astro-ph].

Vink, Jorick S. (2012). "Eta Carinae and the Luminous Blue Variables". In: *Eta Carinae and the Supernova Impostors*. Ed. by Kris Davidson and Roberta M. Humphreys. Vol. 384, p. 221. DOI: 10.1007/978-1-4614-2275-4_10.

Vink, Jorick S. and A. de Koter (Oct. 2002). "Predictions of variable mass loss for Luminous Blue Variables". In: A&A 393, pp. 543–553. DOI: 10.1051/0004-6361:20021009. arXiv: astro-ph/0207170 [astro-ph].

Vink, Jorick S., A. de Koter, and H. J. G. L. M. Lamers (Apr. 2001). "Mass-loss predictions for O and B stars as a function of metallicity". In: A&A 369, pp. 574–588. DOI: 10.1051/0004-6361:20010127. arXiv: astro-ph/0101509 [astro-ph].

Walborn, N. R. et al. (July 1989). "The spectrograms of Sanduleak -69 202, precursor to supernova 1987A in the Large Magellanic Cloud." In: A&A 219, pp. 229–236.

Weis, Kerstin and Dominik J. Bomans (Sept. 2020). "Luminous Blue Variables". In: *arXiv e-prints*, arXiv:2009.03144, arXiv:2009.03144. arXiv: 2009.03144 [astro-ph.SR].

Wolf, C. J. E. and G. Rayet (Jan. 1867). "Spectroscopie stellaire". In: *Academie des Sciences Paris Comptes Rendus* 65, pp. 292–296.

Yoon, S. C., N. Langer, and C. Norman (Dec. 2006). "Single star progenitors of long gamma-ray bursts. I. Model grids and redshift dependent GRB rate". In: A&A 460.1, pp. 199–208. DOI: 10.1051/0004-6361:20065912. arXiv: astro-ph/0606637 [astro-ph].